DISSERTATION

RATIONAL DESIGN AND NOVEL BIOPROCESSES FOR LOW-CARBON BIOFUELS AND BIOPRODUCTS

Submitted by

Danielle Bartholet

Department of Chemical and Biological Engineering

In partial fulfillment of the requirements

For the Degree of Doctor of Philosophy

Colorado State University

Fort Collins, Colorado

Fall 2023

Doctoral Committee:

Advisor: Kenneth Reardon
Co-Advisor: Thomas Foust

Susan De Long
Christie Peebles
Bret Windom

ABSTRACT

RATIONAL DESIGN AND NOVEL BIOPROCESSES FOR LOW-CARBON BIOFUELS AND BIOPRODUCTS

The reduction of fossil fuel consumption and carbon emissions is one of the greatest challenges of our time, and innovative solutions are necessary to prevent climate catastrophe while maintaining economic development and modern ways of life. Biofuels and bioproducts can provide low-carbon alternatives to petroleum fuels and petroleum-based chemical processes. However, several limitations have impeded the wide-scale implementation of bio-based technologies. Biologically derived chemicals frequently do not possess ideal fuel properties due to high oxygen content and lower energy density. Furthermore, petroleum processes remain economically favorable to biological alternatives due to the high costs and low yields associated with bioprocesses. Rational design approaches to the development of new fuels and chemicals combined with improved bioconversion processes are strategies that address multiple aspects of sustainable development for a circular carbon economy.

The broad purpose of this work was to explore and develop low-carbon alternatives to petrochemical products and processes. We begin by proposing a group of novel fuel additive molecules, then explore alternative technologies for their production.

In Chapter 2 of this work, a rational design approach was used to identify “ideal” diesel fuel additive molecules. The desired characteristics of a liquid transportation fuel include high efficiency and engine performance, low particulate emissions, compatibility with current engines and infrastructure, and low risk of environmental contamination. In this work, we use

computational tools to propose structures for diesel fuel additives that meet these criteria. Starting with the chemical structure of dimethoxymethane (DMM), a class of oxygenated molecules, called polyoxymethylene ethers (POMEs) is proposed by varying oxygen content in the backbone length and carbon content in the end group length. Additional structural variations, including iso-alkyl end groups and tertiary branches, are considered here for the first time.

The ten candidate molecules identified consist largely of butyl-terminated POMEs. Synthesis chemistry for butyl-terminated POMEs was developed, utilizing an acid-catalyzed transacetalization reaction of butanol with methyl-terminated POMEs. To improve the sustainability of POME production, it is desirable to produce precursors from biomass using bioconversion processes. Therefore, the focus of this work pivoted to bioprocess technologies for improved production of butanol and other fuel precursor molecules.

Butanol and other molecules of interest are highly reduced metabolic products, requiring the input of electrons through intracellular reducing equivalents. Frequently, the yields of these reduced products are limited due to redox constraints of metabolic pathways. Electro-enhancement, which refers to the direct supplementation of electrons from solid electrodes, may overcome redox constraints by enabling “unbalanced fermentations”. While electro-ehancement of processes like fermentation (electro-fermentation) and anaerobic digestion (electro-AD) has been reported to successfully induce metabolic shifts and alter product profiles, much remains unknown about the mechanisms leading to observed shifts. Chapter 3 provides a detailed review of the literature in this field, highlighting the challenges and shortcomings of electro-enhancement research. Methods developed to improve the study of bioelectrochemical systems are also presented here.

In Chapter 4, we apply these methods to pure culture electro-fermentations of *Clostridium pasteurianum* with the objective of increasing butanol production. Our results indicate that applied potentials may affect metabolite profiles through redox control but did not provide sufficient evidence for direct bacterial/electrode interaction. In Chapter 5, these methods are applied to electro-AD of food waste inoculated with wastewater sludge. Applied potentials are shown to have a wide range of effects on product profile and microbial communities. These results suggest that electro-enhancement may provide a method for fine-tuning product profiles in heterogeneous, mixed culture systems. However, further experiments are required in both pure and mixed culture systems to fully elucidate the effect of electro-enhancement on cellular proceses. Through this work, new methods were developed to facilitate future research in bioelectrochemical systems and enable the design of improved electro-enhanced bioprocesses.

ACKNOWLEDGEMENTS

I'd like to thank each of my committee members for their guidance and mentorship. Thank you, Dr. Bret Windom, for convincing me to come to CSU for graduate school in the first place, and to my co-advisor Dr. Tom Foust for giving me the opportunity to pursue this degree and to collaborate with NREL. Thank you, Dr. Christie Peebles for your pep talks whenever I expressed self-doubt and Dr. Susan De Long for your valuable contributions to my work. Most of all I'd like to thank my advisor Dr. Ken Reardon for being not just a great PhD advisor, but a true mentor. The last five and a half years have brought so many challenges and major life changes, and I am so grateful for your patience, understanding, and support through everything.

I have so many peers and friends to thank for their collaboration and commiseration. Thank you for crying with me, laughing with me, and sharing in this wild journey that is grad school: the C2B2 crew who were my first friends in Colorado and encouraged me to pursue a PhD; Abby Grieb, Maddy Florestano, Ben Platt, Alec Taylor, Hattie McKenzie, and Sean Engels; my first-year cohort, especially Jaron Thompson, who I spent countless late nights studying thermo and math modeling with; My lab mates; Mark Greenwood and Kees Baas; and my work besties Dr. Abby Orun and Claire Bailey. Also thank you to Vail Baumer's flash drive because I didn't get my own until the last month of my PhD.

Thank you to the incredible undergraduates who were instrumental in completing this work: Emily Weintraut, Emma Barrett, Mariana Sauceda, Amanda Mohrlang, Payton Belli, Amanda Schmidt, Polina Zaytseva, Ian Wettlaufer, Juni Zugush, and Michael Evans. Thank you especially to Emma for your contributions to the AD reactor design and Polina for getting me through this last year. I truly couldn't have done it without you.

Thank you to Timothy Gonzales for your assistance with so many things over the years, and to Adam Sherrer and Grace Blaskowski for building my super nifty incubator. Thank you to Dr. Jaclyn Adkins for letting me annoy you constantly about electrochemistry and vent to you about my doubts and frustrations.

Thank you to Roland Ulber's group at TU Kaiserslautern for hosting me, and especially to Jan- Niklas Hengsbach and Marienne Volkmar for your help with lab work and to Ludovica Varriale for helping me through a challenging time abroad.

And finally, thank you to my family and friends who have no idea what I do, but have enthusiastically supported me every step of the way on my academic journey. Thanks Mom and Dad for the many sacrifices you've made to give me every opportunity to succeed. Thank you to my dear Mamaw and my sissy for being my biggest cheerleaders and to Henry and my niece for reminding me why I do what I do. I hope I can help make the world a better place for you.

TABLE OF CONTENTS

CHAPTER 1: BACKGROUND

1.1 Circular Carbon Economy

Virtually every object you have come into contact with today exists because of fossil fuels. Maybe the textiles in your clothing contain polyester, a petroleum-derived synthetic material. If you're wearing organic cotton, the machinery used to plant, harvest, and process it likely consumed large quantities of fossil fuels. Many of the items we use every day were produced from petroleum-based chemical processes, and even those that are not required the transportation of raw materials, powering of factories, and distribution of finished products. When we consider just how many of our modern comforts would not exist without the use of petroleum, it is easier to see that the use of fossil fuels has helped mankind immensely. As an environmentalist, I had a hard time writing that sentence. If you find yourself struggling to come to terms with the benefits of fossil fuels, consider the way cheap, disposable petroleum-based plastics have revolutionized medicine and scientific research by improving infection control, sterility, and accessibility. It is no coincidence that the use of fossil fuels mirrors the rise of global GDP and improved quality of life[1].

Anyone reading this document is likely well-versed in the negatives of our petroleum-based economy. I don't need to tell you that global warming is bad, but I will: Global warming is bad. Burning fossil fuels releases greenhouse gasses into the atmosphere, and these anthropogenic emissions have undoubtedly led to the climate crisis that threatens the weather patterns, food production, biodiversity, and ecosystem services we depend on to survive. The excessive use of disposable plastics leads to the generation of massive quantities of trash and pollution of oceans and waterways. And of course, there's the small detail that fossil fuels are

nonrenewable resources. They are finite and will not be regenerated on a timescale worth considering.

All this to say, we **need** to reduce our use of petroleum, but we can't just stop using it. Innovative solutions are needed to enable sustainable global development. The circular carbon economy is a framework for achieving this sustainable development. To illustrate the concept of a circular carbon economy, let's briefly step back to 7th grade science class and consider the earth's carbon cycle. In the carbon cycle, plants take carbon dioxide from the atmosphere and convert it into biomass. Plants and animals respire and eventually die and decompose, releasing carbon back into the atmosphere and earth to be used again and again. Without the extraction of fossil fuels, the total amount of carbon within this cycle remains constant. Fossil fuels are called *fossil* fuels for a reason – they formed from the fossilized remains of biomass sequestered deep within the earth's crust for millions of years. When we extract them, we are introducing "new" carbon to the carbon cycle. In a circular carbon economy, the carbon that already exists in the earth's carbon cycle is used to meet our carbon demands.

One strategy for implementing a circular carbon economy is the use of bioprocess technologies, which take advantage of cellular machinery to produce organic molecules from bio-based precursors, in place of petroleum-based processes. Bioprocesses utilize renewable feedstocks such as crops and organic wastes. Since these renewable resources contain carbon that already exists in the carbon cycle, their use results in lower, or even negative, net emissions of greenhouse gases.

Furthermore, products made from biological processes are more likely to be biodegradable than those derived from petroleum[2,3]. Because bioprocesses rely on enzymatic reactions, the chemical structures of products derived from them are more compatible with

metabolic processes of microorganisms and enzymes, enabling more efficient biodegradation. In contrast, petroleum products are highly recalcitrant to biodegradation, as they contain carbon structures that are not naturally occurring in ecosystems[4]. Microorganisms may not possess the necessary enzymes to effectively break down these complex and unfamiliar molecules.

1.2 Biofuels

Biofuels are a category of bioproducts that are particularly important for reducing greenhouse gas emissions. The use of biofuels and bio-based blendstocks displaces a fraction of fossil fuels. While the combustion of biofuels results in the same release of carbon as the combustion of fossil fuels, carbon released in biofuel combustion was captured from the atmosphere through photosynthesis. This cycling of carbon allows biofuels to achieve low or zero net emissions.

One of the most ubiquitous biofuels used today is ethanol. Ethanol is typically added into gasoline at 10% (v/v) blending to displace fossil fuels and oxygenate the fuel for cleaner combustion, as mandated by the Clean Air Act in 1990[5]. Oxygenates such as ethanol increase the oxygen content during combustion, facilitating more complete combustion and the oxidation of carbon monoxide to carbon dioxide. While ethanol is currently the standard blendstock for gasoline oxygenation, many biologically derived molecules could be considered for this purpose, as biological processes excel at producing oxygenated functional groups.

In the US, more than 15 billion gallons of bioethanol is produced annually[6]. This ethanol is typically produced from corn, with about 90 million acres of agricultural land dedicated to corn ethanol production[7]. Corn and sugar cane ethanol from the United States and Brazil, respectively, account for 84% of global bioethanol production[6]. In Europe, a less monoculture-based

agricultural system and less cultivable land limits the production of bioethanol, and the majority of biofuels are biodiesels from plant oils and used cooking oil[6].

Corn and sugarcane ethanol are considered first generation biofuels[8]. These feedstocks contain large amounts of easily extractable sugars and carbohydrates, which can be readily fermented by yeast to produce large quantities of ethanol. The processes for ethanol production from these high-sugar and high-starch crops is simple and enables high-yield production at a large scale. However, there are major drawbacks to first generation biofuels.

In the US, more than 15 billion gallons of bioethanol is produced annually6. This ethanol is typically produced from corn, with about 90 million acres of agricultural land dedicated to corn ethanol production7. Corn and sugar cane ethanol from the United States and Brazil, respectively, account for 84% of global bioethanol production[6]. In Europe, a less monoculture-based agricultural system and less cultivable land limits the production of bioethanol, and the majority of biofuels are biodiesels from plant oils and used cooking oil[6].

Corn and sugarcane ethanol are considered first generation biofuels[8]. These feedstocks contain large amounts of easily extractable sugars and carbohydrates, which can be readily fermented by yeast to produce large quantities of ethanol. The processes for ethanol production from these high-sugar and high-starch crops is simple and enables high-yield production at a large scale. However, there are major drawbacks to first generation biofuels. These feedstocks are produced through intensive farming practices, which require massive inputs of water, pesticides, and energy. Furthermore, there are serious concerns about competition with food crops for agricultural land and resources.

Further generations of biofuels address some of these issues, but come with their own challenges. Second generation biofuels refer to those made from biomass derived from non-food

crops, such as agricultural residue, grasses, and forestry wastes[9]. While this lignocellulosic biomass is abundant, inexpensive, and can be derived from waste streams, the extraction of usable sugars from highly recalcitrant biopolymers requires significantly more pretreatment before enzymatic conversion, increasing the cost and energy demand of the production process[9,10]. Algal biofuels also present technical challenges that prevent economic competition with fossil fuels.

These limitations, and interest in newer technologies such as electrical energy storage and hydrogen fuel, have reduced interest in biofuels as alternative transportation fuels. However, we argue that biofuels remain the most promising strategy for reaching carbon neutrality for the following reasons: (1) Not all vehicles can be electrified. The aviation, heavy-duty trucking, rail, and marine sectors require alternative decarbonization strategies due to the high energy densities they require11. (2) The majority of the electricity consumed to charge electric vehicles and power manufacturing processes comes from fossil fuels[6,12]. Therefore, while electric vehicles can help reduce non-point source pollution, they may have little to no effect on net greenhouse gas emissions. (3) The lifecycle of an electric vehicle poses several other environmental concerns including the extraction and purification of rare earth metals and disposal of toxic batteries[12]. (4) Hydrogen powered and electric vehicles require large changes in infrastructure[12], whereas liquid biofuels could be amenable to current transpiration systems and even existing vehicles. Finally, regardless of the shiny new technologies we can propose for alternative energy sources, biofuels are the simplest answer. Biofuels take advantage of energy from the sun that is converted and stored in chemical bonds by a process that has evolved over billions of years.

To drive forward the widespread use of biofuels, their limitations need to be addressed to make them economically competitive with fossil fuels. Advancements in biofuel research can be

divided into three focus areas: (1) The development of novel molecules for improved fuel properties and reduced emissions, (2) engineering of feedstocks and alternative feedstock sourcing, and (3) improvements to conversion technologies[6]. The present work touches on all three of these areas of development. In Chapter 2, a **rational chemical design** approach is used to propose novel bio-based diesel fuel additives for reduced emissions of particulate matter. The remainder of this work focuses on improved bioconversion through **electro-enhanced bioprocesses**. We also explore the use of alterative feedstocks, applying electro-enhancement to the **valorization of wet wastes**.

1.3 Rational design of novel bio-based fuels and chemicals

Advances in predictive chemical modeling enable a rational design approach to biofuel development. Rational design is a strategy of creating new molecules with specific properties and functions based on computational methods and established principles of chemistry. Historically, chemical compounds have been discovered through trial and error and high-throughput screening approaches. In contrast, rational design approaches aim to streamline the discovery process by providing a framework for designing molecules based on target properties and functions. A rational design approach begins with identifying the desired chemical properties. Structure-activity relationships are then used to group properties with functional groups or other structural variations.

This approach can be applied to a wide range of commodity chemicals, pharmaceuticals, and fuel molecules. In the context of biofuels, it is increasingly being implemented to retrosynthetically design biochemical pathways for biological production of alcohols, fatty acids, and terpenes with specific functionalities[6]. Here, we use rational design not for retrosynthetic

pathway design of biomolecules, but to propose novel structures for diesel fuel additive molecules with desired properties.

When considering an "ideal" liquid transporation fuel, we can identify the following criteria: Efficient, clean burning, amenable to current infrastructure, and produced from biological precursors. While this "perfect" fuel is not attainable in the immediate future, fuel additives can be designed to improve the properties of existing fuels. The conventional ground transportation fuels are gasoline for spark ignition engines, and diesel for compression ignition. Diesel fuels offer the benefit of higher efficiency, but at the expense of clean combustion. In diesel fuel combustion, incomplete oxidation of carbon species resulting from non-homogenous fuel vaporization and ignition causes the formation of particulate matter (PM), which is a serious environmental and health concern[11–15] Oxygenated molecules can significantly reduce emissions of PM during diesel combustion, but high oxygen content can negatively impact the efficiency combustion properties of diesel fuels. In chapter two, we use a rational design approach to identify diesel fuel additive molecules that significantly reduce soot formation during combustion and can be produced from bio-based precursors while maintaining engine performance.

1.4 Electro-enhanced bioprocesses

The second crucial area for advancing biofuel technologies is the development of improved conversion processes – the processes by which raw biomass is converted into desired products. Corn ethanol production involves minimal steps for conversion, while more sustainable, woody biomass feedstocks require additional treatment to overcome recalcitrance of lignocellulosic material[16]. Generally, the first step for any bioconversion process is mechanical

pretreatment, where raw biomass is ground, milled or otherwise mechanically broken down to increase surface area, flow properties, and homogeneity for further processing[16]. Physiochemical pretreatment methods, such as steam explosion, can also be used. In steam explosion, steam expands within lignocellulosic materials, leading to disruption of individual fibers and cell wall structure[16]. Enzymatic processes and chemical pretreatment methods including including acids, bases, and organic solvents are commonly used.

Following pretreatment, extracted sugars can be used as substrates for microbial conversion to alcohols and other metabolic products. The most well-known bioconversion process is yeast fermentation, where sugars are converted anaerobically to alcohols and organic acids by yeasts such as *Saccharomyces cerevisiae*. In fermentative metabolic pathways, glucose or other carbon substrates are converted into pyruvate during glycolysis, where ATP is generated. NAD is then regenerated for glycolysis by transferring electrons to organic electron acceptors. The requirement of fermentative pathways to utilize organic molecules as terminal electron acceptors results in the production of reduced metabolites, making fermentation an industrially important process for production of valuable products such as organic acids and alcohols. Fermentative pathways are therefore driven by the intracellular balance of redox molecules, and yields of highly reduced molecules are limited by this redox constraint.

High cost and energy demand of biomass pretreatment is frequently regarded as the most significant constraint to the implementation of bioprocess technologies. An important area of research is the improvement of processes for digesting highly recalcitrant biopolymers like lignin. Approaches for improving lignocellulosic biomass conversion include genetic modification of feedstock crops to alter biopolymer structures and increase production of value-

added chemicals[17], development of novel chemistry for deconstruction of biopolymers and engineering approaches for improving efficiency of chemical and physiochemical processes.

Following extraction of sugars from biomass feedstocks, fermentation of these sugars to produce desired products is also an energy and resource demanding step of the conversion process. Therefore, improved bioconversion technologies are vital for improving product yields and lowering costs. Multiple approaches for improved bioconversion also exist including the exploration of non-model organisms with varied metabolic capabilities, metabolic engineering to improve product yields or increase production of value-added products, implementation of co-cultures, and engineering approaches investigating reactor design and operation conditions. In this work, we explore a novel approach to improving bioconversion: electro-enhancement.

Here, we use the term electro-enhancement to refer to the use of a solid electrode as an electron donor in bioprocesses. Electro-enhanced bioprocesses allow us to harness cheap, renewable electrons from solar and wind power to overcome redox constraints in fermentation and drive metabolic reactions for improved production of reduced metabolites. The technologies for performing electro-enhanced bioprocess are called bioelectrochemical systems (BES). The field of BES as well as methods for studying these systems is explored in depth in chapter three. In Chapter 4, electro-enhancement is applied to a pure culture fermentation (electro-fermentation) for improved biobutanol production. In Chapter 5, we explore electro-enhancement of a complex, mixed-culture process (electro-AD) that utilizes organic wastes to produce volatile fatty acids.

1.5 Organic Waste Valorization

An attractive alternative to fuel crops and lignocellulosic biomass is the use of organic waste as a feedstock for the production of biofuels and bioproducts. Abundant, energy-dense waste streams such as livestock manure and food waste provide a sustainable, cheap, and low carbon source of substrates that can be converted into a range of valuable products. These closed-loop processes couple waste management with sustainable production of fuels and chemicals.

One benefit of organic waste feedstocks is that they bring with them their own biocatalysts. In the example of corn ethanol production, enzymes are used to digest starches into simple sugars, then an inoculum of specific yeast strains is used to ferment sugars to alcohols. Processes for lignocellulosic biomass include even more complexity, with intense mechanical and chemical pretreatment required to extract fermentable sugars. In contrast, organic waste streams contain their own diverse community of microorganisms, all serving different roles in the breakdown of complex biomolecules into a range of products. We can therefore take advantage of these communities to perform multiple stages of the conversion process.

One example of organic waste valorization is anaerobic digestion (AD). AD occurs naturally in anaerobic environments that are rich in organic matter, such as marine sediments. Industrially, AD is used to convert organic wastes, such as manure and food waste, into biogas and solid digestate, which are used as renewable fuel and fertilizer. AD involves multiple metabolic processes performed by a diverse community of archaea and bacteria. Complex biomolecules are broken down into simple sugars by hydrolytic microorganisms. These simple sugars can then be fermented to produce organic acids and alcohols. The primary intermediate products are 2-6 carbon volatile fatty acids (VFAs). Following this acidogenic step, acetogens will convert longer chain VFAs into acetate, which is then consumed by methanogens to produce

methane. While biogas has traditionally been the target product of AD processes, VFAs and other soluble products have higher economic value and can be used to produce liquid biofuels.

The balance of these processes and the distribution of soluble and gaseous products is highly dependent on digestion conditions, feedstock, and the microbial community. In Chapter 5 of this work, we explore how applied potentials affect electrode microbial communities and alter microbial processes in AD with the goal of increasing the production of longer chain acids and inhibiting methanogenesis.

CHAPTER 2: DESIGNER FUELS: IDENTIFYING AND SYNTHESIZING NOVEL BIO-DERIVED FUEL ADDITIVES FOR CLEAN AND EFFICIENT COMBUSTION

2.1 Introduction

Compression ignition (CI) engines provide the benefit of improved efficiency when compared to spark ignition engines. However, the combustion of diesel fuels in CI engines produces more particulate matter (PM) than the combustion of gasoline in spark ignition engines [18]. Adverse effects on climate change and human health have been linked to PM from fossil fuel combustion[11–13,19]. Jacobson reported that PM is the second-most significant contributor to global warming following carbon dioxide [19,20]. Also concerning are the well-documented short and long-term effects of PM on pulmonary and cardiovascular health, as well as millions of premature mortality rates [11–15]. While novel, alternative fuels and propulsion system designs are important technologies to investigate as long-term solutions to the problems created by fossil fuel dependence, massive changes in energy infrastructure are not likely to occur for many years. Therefore, solutions must be found to minimize the ecological and health impacts of diesel fuel combustion within the current infrastructure. A promising solution is the rational design of environmentally benign diesel fuel blendstocks that will reduce PM emissions while maintaining or improving engine efficiency. Many studies have investigated the effects of oxygenated fuel blendstocks on the formation of PM during diesel combustion[21–27]. The presence of carbon-oxygen bonds leads to lower concentrations of the soot precursors that are formed in the locally fuel-rich premixed ignition that is characteristic of diesel engines[22]. However, the presence of oxygen has a negative impact on the lower heating value (LHV) of a fuel component. While soot reduction depends on oxygen content to the first order [28], it also depends on the specific oxygenated functionality [29], so the molecular structures and

physicochemical properties of the oxygenated species are important when considering blending effects and engine performance. For example, ethanol is commonly added to gasoline, but its use as a diesel fuel additive is limited by low cetane number; low flashpoint temperature, which creates headspace flammability concerns in fuel tanks; and poor miscibility, which results in the need for engine and distribution infrastructure modifications [23,24,30].

It is also important to consider the environmental fate of a potential fuel additive molecule. Methyl tert-butyl ether (MTBE) was used widely as an oxygenated additive in gasoline to reduce emissions. However, due to its water solubility and environmental persistence, MTBE became a problematic groundwater and soil contaminant [31] and is no longer used as a fuel additive in the United States [32].

A molecule that has recently gained attention as a potential diesel additive is dimethoxymethane (DMM), also known as methylal (Fig. 1). DMM has been shown to significantly reduce soot[33]; however, it has a much lower LHV than petroleum fuels, is highly soluble in water, and fails to meet the diesel criteria for flash point (T_{flash}). Recently, polyoxymethylene dimethyl ethers (POMDMEs), molecules similar to DMM but with longer oxymethylene backbones, have been investigated [33–37] (Fig. 2). The increased oxygen content of POMDMEs suggests they would provide effective suppression of soot formation, and POMDMEs of backbone length n=2–3 (Fig. 2) may be more miscible in diesel fuel [34] and have higher cetane numbers than DMM. However, due to the high oxygen content and short alkyl end groups of POMDMEs, they have low LHV and are likely to be highly water soluble and non-biodegradable, making them potential environmental contaminants. Lautenschütz et al. also investigated the fuel properties of POMDMEs analogs that have ethyl end groups [38]. While these ethyl-terminated polyoxymethylene ethers (POMEs) demonstrated some favorable properties, such as high cetane numbers, they still fell short of optimal

LHVs for diesel fuel [38.] Furthermore, that study did not consider whether the investigated POMEs could be potential environmental contaminants.

Industrially, DMM, (MM-POME$_1$; see Section 2.1 for nomenclature) is synthesized by acetalization of formaldehyde[33]. Chain propagation can then be achieved through reacting paraformaldehyde and MM-POME$_1$ over an acid catalyst to produce POMDMEs (MM-POME$_2$ through MM-POME$_8$). These methyl-terminated POMEs have also been synthesized directly from dimethyl ether over a Ti$(SO_4)_2$/activated carbon catalyst with high selectivity[39]. Methanol (MeOH) and its derivative, formaldehyde, are the primary chemicals utilized for MM-POME synthesis,[8] and therefore, a low carbon-intensity POME-based fuel can be derived from ligno-cellulosic biomass via biomass gasification and methanol synthesis[40–43].

In this study, we used a rational design approach to identify POMEs with the potential to reap the benefits of POMDMEs, including effective soot reduction and high cetane number, while circumventing the limitations of engine and infrastructure incompatibility and environmental concerns. Sixty-seven candidate POMEs (Fig. 3) were evaluated, including linear structures of backbone length n = 1-7 and alkyl end groups of length C1-C5 as well as structures with isopropyl and isobutyl end groups, and structures with a tertiary alkyl branch of length C1-C4. Only a few variants of POMEs have been investigated previously, and most of their fuel properties remain unknown. Thus, several predictive tools were used to estimate the LHV, melting point (T_{melt}), T_{flash}, biodegradability, water solubility, ignition delay, derived cetane number (DCN), and hydrocarbon solubility of each molecule. There is no ASTM standard test for characterizing the sooting tendency of diesel fuels, so most fuel design studies are unable to consider soot (e.g., 29). In this study we include soot by using a relatively new parameter, yield

sooting index (YSI), which is defined as the amount of soot formed by a fuel when it is doped at low concentration into a base methane/air flame[49]. We have shown elsewhere that YSI correlates well with the ASTM D1322 smoke point test used for characterizing sooting tendencies of jet fuels but has the benefit of requiring less sample volume (100 μL vs 10 mL) and offering a wider dynamic range that encompasses low soot molecules such as POMEs 30,31. POMEs were evaluated against fuel criteria both as pure compounds and as blendstocks in diesel fuel at 10-50% blending.

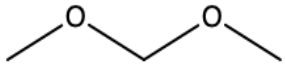

Figure 1: Chemical structure of dimethoxymethane (DMM).

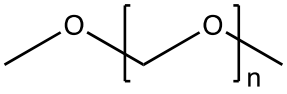

Figure 2: General chemical structure of polyoxymethylene dimethyl ethers (POMDMEs).

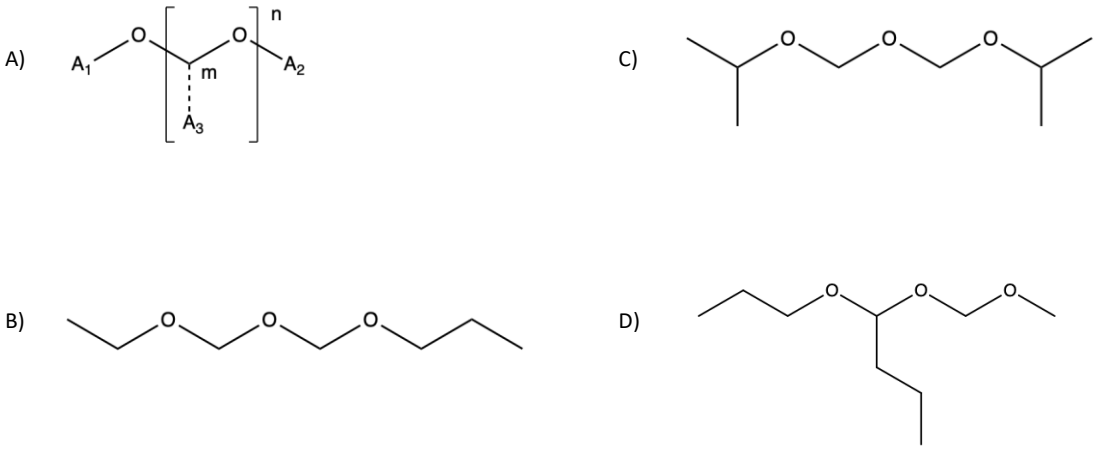

Figure 3: Polyoxymethylene ether (POME) structures. (A) General structure of POMEs. A_1, A_2, and A_3 are alkyl terminating groups, and *n* is the POME backbone length. The possible single branch point is indicated at *m*, and the dotted line indicates that some POME molecules are not branched. (B) Example linear POME with linear end groups: EP-$POME_2$. (C) Example linear POME with branched end groups: iPiP-$POME_2$. (D) Example branched POME with linear end groups: 1P-PM-$POME_2$. Only structures with a single A_3 group were considered in this study.

2.2 Materials and Methods

2.2.1 POME Nomenclature

A general nomenclature for POMEs is defined here as *mA_3- A1A2-POMEn*, where A_1 and A_2 represent the terminating alkyl groups and A_3 represents an optional tertiary branch. Alkyl groups are designated by M, E, P, B, and Pe for methyl, ethyl, propyl, butyl, and pentyl groups respectively. The branch point (if one) is indicated by *m*, and *n* is the POME backbone length (Fig. 3A). Linear POMEs (Fig. 3B) are named by ordering the terminating groups from shortest to longest. POMEs with iso-alkyl groups were also considered and are denoted as iP or iB for isopropyl and isobutyl groups respectively (Fig. 3C). The first term of the general nomenclature accounts for tertiary branching (Fig. 3D). When naming branched POMEs, the branch point m is numbered from the closer end and the terminating groups named beginning with that end.

2.2.2 POMEs Used in Property Measurements

MM-$POME_1$ (DMM; 99.0% from Sigma-Aldrich and 99.5% from Acros), EE-$POME_1$ (ethylal; 99.0% from Acros and 99.0% from Merck), and BB-$POME_1$ (butylal; 98.5% from Sigma-Aldrich) were used as received. A mixture of $POME_{3-6}$ was procured from ASG Analytik-Service GmbH (Germany). The mixture was fractionated and purified via distillation (spinning band) to obtain MM-$POME_3$, MM-$POME_4$, MM-$POME_5$, and MM-$POME_6$.

2.2.3 Estimation of POME Properties

2.3.3.1 Boiling Point, Melting Point, and Flash Point

Basic physical properties such as melting point and boiling point were considered to ensure that the blendstock can be handled within the existing liquid fuel infrastructure and can be

blended and combusted easily with diesel fuels. Melting point is an important property when considering the engine compatibility and cold- flow properties of a potential fuel additive. At temperatures below the melting point, crystallization can occur, leading to improper fuel delivery and injection resulting in poor combustion 32. Criteria for low temperature properties are typically specified regionally based on local ambient conditions (ASTM D975-20a)33.

Since diesel fuel is a highly complex multicomponent mixture, the boiling point (T_{boil}) is specified as the 90% distillation temperature, or T90. To ensure that blending with POMEs will not affect the T90 of diesel fuels, the boiling points of pure POMEs must be considered. The flash point is an indicator of flammability and is important for safe transportation, storage, and use of a fuel 34. It was therefore considered to ensure safe handling and transportation of both the pure POME and the finished fuel blend, as well as behavior within existing diesel engines.

The Estimation Programs Interface Suite (EPI Suite) software35 was used to predict T_{boil} from the Adapted Stein and Brown Method, and T_{melt} (Mean or Weighted T_{melt}). Flash point values were then calculated from the predicted boiling points using three models: Butler36 (Eqn. 1), Prugh37 (Eqn. 2), and Prugh alcohol37 (Eqn. 3). The Prugh and Prugh alcohol models also depend on elemental mass percentages through the parameter X_{st} (Eqn. 4). Measured flash points were used to select the most appropriate T_{flash} model, and results from all three models are reported in Supplementary Materials.

$$T_{flash}(°\mathrm{F}) = 0.683 \cdot T_{boil}(°\mathrm{F}) - 119 \quad (1)$$

$$T_{flash}(K) = \frac{T_{boil}(K)}{1.442 - 0.08512 \cdot \ln(X_{st})} \quad (2)$$

$$T_{flash}(K) = \frac{T_{boil}(K)}{1.3611 - 0.0687 \cdot \ln(X_{st})} \quad (3)$$

$$X_{st} = \frac{83.8}{4.0 \cdot C + 4.0 \cdot \mathrm{S} + \mathrm{H} - \mathrm{X} - 2.0 \cdot \mathrm{O} + 0.84} \quad (4)$$

In Equation 4, C, O, H, and S represent the elemental mass percentages of carbon, oxygen, hydrogen, and sulfur in the candidate molecule, and X represents the elemental mass percentage of halogens.

2.3.3.2 Lower Heating Value

LHV is an important property for efficiency and fuel economy, so POMEs with higher LHVs are desirable. Three models were used to predict higher heating values (HHV) for each candidate molecule: The Dulong equation 38 (Eqn. 5), the Boie model 39 (Eqn. 6), and the Lloyd and Davenport model 40 (Eqn. 7). Each uses the elemental mass percentages of carbon, oxygen, hydrogen, nitrogen, and sulfur 38–41. Lower heating values (LHV) were then calculated according to ASTM D240 42 (Eqn. 8). Measured LHV values for several POMEs were used to select the most appropriate model, and results from all three models are reported in Supplementary Materials.

$$HHV\ \left(\frac{MJ}{kg}\right) = 0.336 \cdot C + 1.418 \cdot H + 0.094 \cdot S - 0.145 \cdot O \quad (5)$$

$$HHV\ \left(\frac{MJ}{kg}\right) = 0.3515 \cdot C + 1.1617 \cdot H + 0.06276 \cdot N + 0.1046 \cdot S - 0.1109 \cdot O \quad (6)$$

$$HHV\ \left(\frac{MJ}{kg}\right) = 0.3578 \cdot C + 1.1357 \cdot H + 0.059 \cdot N + 0.1119 \cdot S - 0.0845 \cdot O \quad (7)$$

$$LHV\ \left(\frac{MJ}{kg}\right) = HHV - 0.2122 \cdot H \quad (8)$$

2.3.3.3 Yield Sooting Index

The YSI, an index of sooting tendency, was evaluated to identify clean-burning molecules predicted to have low propensity for soot formation. YSI was predicted using a group contribution model for sooting tendency43. For the predictions reported here, the model used a training set consisting of about 500 measured YSIs for regular hydrocarbons and oxygenates.

2.3.3.4 Derived Cetane Number and Ignition Dela

Ignition delay (τ) and DCN are important metrics to evaluate combustion speed and fuel quality. These properties were evaluated to ensure that POMEs will not compromise the engine performance of blended fuels. Here, the ignition delay is defined as time following injection before primary heat release from autoignition of the fuel, thus accounting for both the mixture formation and ignition chemical kinetics. Values of τ were calculated from a group contribution model44 using predicted vapor pressures and molecular structures. The EPI Suite software35 was used to predict vapor pressures as the mean of the Antoine and Grain methods. The ignition delay is then typically used to calculate DCN from ASTM D6890 45 (Eqn. 9-10).

$$DCN = 4.460 + \frac{186.6}{\tau} \qquad 3.1\ ms \leq \tau \leq 6.5\ ms \qquad (9)$$

$$DCN = 83.99(\tau - 1.512)^{-0.658} + 3.547 \qquad \text{Otherwise} \qquad (10)$$

For many of the candidate POME molecules, the calculated ignition delays were less than 1.512 ms and thus the DCN could not be calculated from Equations 9 and 10.

A machine learning model was also used to predict DCN. The model was trained using a previously developed database of nearly 500 cetane measurements from both IQT-based DCN and CFR engine CN tests46.The model takes the form of a graph neural network, where a molecule's structure is encoded in a graph consisting of atoms (nodes) and bonds (edges), each with distinct features47. In this model, atom features included the element type, total number of

attached hydrogens, aromaticity, and presence in a ring. Bond features included the element type of the bridged atoms, bond type, and presence in a ring. After training, the model reached a mean absolute error on held-out validation data of 8.02 CN units. Predictions reported here were taken from the September 29th, 2020 version of the model.

2.3.3.5 Biodegradability and Water Solubility

Biodegradability and water solubility were evaluated to determine the potential for detrimental persistence in the environment. In the handling and distribution of liquid fuels, the release of small amounts of these fuels into the environment is inevitable, and molecules that are highly soluble will easily enter ground and surface water. Therefore, it is important that all fuel components will biodegrade into non-toxic, environmentally benign products.

The Ready Biodegradability Prediction from the EPI Suite35 BIOWIN model, which accounts for both aerobic and anaerobic biodegradation, was used for biodegradability assessment. Water solubility was predicted from the EPI Suite model based on the octanol/water partition coefficient. The solubility of MTBE, used to determine the criterion for POME solubility, was also predicted using EPI Suite due to the variability of published data and to provide a consistent comparison to predicted POME solubilities.

2.3.3.6 Solubility in Hydrocarbons

Solubility in hydrocarbons is a critical parameter for miscibility with hydrocarbon-based fuels48. The first level of a group contribution method49 was used to estimate Hansen Solubility Parameters for dispersion (δ_d), polarity (δ_p), and hydrogen bonding (δ_{hb})**.** Solubility

parameters for conventional diesel fuel were found in the literature 50. The sphere of solubility was determined by using the solubility of n-butanol in diesel as a limit, where the radius, R, is equivalent to the distance between diesel fuel and n-butanol on the Hansen solubility diagram. The solubility parameters for butanol and ethanol were also found in the literature50. The sphere of solubility is given by:

$$\left(\delta_d - \delta_{d,diesel}\right)^2 + \left(\delta_p - \delta_{p,diesel}\right)^2 + \left(\delta_{hb} - \delta_{hb,diesel}\right)^2 = R^2 \quad (11)$$

where

$\delta_{d,diesel} = 14.51$

$\delta_{d,butanol} = 16.0$

$\delta_{p,diesel} = 3.18$

$\delta_{p,butanol} = 7.5$

$\delta_{hb,diesel} = 5.79$

$\delta_{hb,butanol} = 15.8$

and

$$R = \sqrt{(\delta_{d,butanol} - \delta_{d,diesel})^2 + (\delta_{p,butanol} - \delta_{p,diesel})^2 + (\delta_{hb,butanol} - \delta_{hb,diesel})^2}$$

2.2.4 Estimation of POME/Diesel Blend Properties

2.2.4.1 Flash Point Estimation

Wickey and Chittenden51 proposed a simple method for calculating flash points of mixtures ($T_{flash,mix}$) that depends only on the flash point ($T_{flash,i}$) and volume fractions (φ_i) of the components (i) (Eqn. 12-14).

$$log_{10}(I_i) = -6.1188 + \frac{2414}{T_{flash,i}(^\circ C)+230.56} \quad (12)$$

$$I_{mix} = \sum \varphi_i I_i \quad (13)$$

$$T_{flash,mix}(°C) = \frac{2414}{6.1188 + log_{10}(I_{mix})} - 230.56 \quad (14)$$

2.2.4.2 LHV Estimation

Several studies have demonstrated that the LHV of a mixture is linearly dependent on the blendstock fraction52,53. Tesfa et al.52 proposed Equation 15 for estimating the LHV of biodiesel blended diesel fuels as a function of the blendstock volume fraction X:

$$LHV_{blend} = -0.041X + 42.32 \quad (15)$$

Here, we use a simple linear mixing rule based on the LHV of each of the components (LHV_i):

$$LHV_{blend} = \sum X_i LHV_i \quad (16)$$

2.2.4.3 YSI Estimation

McEnally et al.[69] showed that a linear mixing rule (Eqn. 17) is accurate for predicting YSI based on the YSI of each component (YSI_i).

$$YSI_{blend} = \sum X_i YSI_i \quad (17)$$

Here, X_i is the blendstock mole fraction and YSI_i is the YSI of each component. The YSI of certification diesel fuel was measured as 256 in this study. The molecular weight of the V2 diesel surrogate was used as an estimate for the molecular weight of diesel fuel55.

2.2.5 Screening POMEs as Potential Diesel Blendstocks

The process of screening POME molecules involved two phases, the first of which addresses basic requirements for a diesel fuel (Table 1). The POMEs passing the first screening

phase were then evaluated for properties desirable to produce a clean-burning fuel (Table 2).

The criteria for boiling point and flash point were determined based on ASTM standards for conventional (No. 2-D) diesel fuel. Thus, the ASTM T90 limit for diesel fuel, as 338 °C, was established as the boiling point criterion for POMEs. Also stated in ASTM D975-20a33, No.2-D diesel fuels are required to have a flash point above 52 °C. ASTM D975 does not specify a cloud point criterion, which depends on the ambient temperature where the finished blend will be used. While cloud point is a widely used metric to evaluate cold weather operability, no models for cloud point estimation are available. Therefore, melting point was used to evaluate the cold flow properties of POMEs. The criterion of 0 °C for the blendstock melting point was selected to ensure acceptable operability in most conditions and handling in liquid fuel infrastructures. Blendstocks with lower melting points would likely be required seasonally in some regions.

There is no ASTM specification for the LHV of diesel fuels. Therefore, to develop an LHV criterion, a comparison was made to ethanol-blended gasoline. Ethanol is commonly blended into gasoline with a blendstock fraction of 10% and has a low LHV of 28.89 ± 0.3 MJ/kg56 . The LHV of 10% ethanol blended gasoline (E10 gasoline) is 3.9% lower (43.95 ± 0.60)[71] than that of gasoline without ethanol (45.72 ± 0.20). Since this small reduction of LHV is widely accepted for gasoline, the criterion for LHV of pure POMEs has been specified so that the LHV of 10% POME/diesel blends is no more than 3.9% lower than that of conventional diesel (43 MJ/kg)53.

DCN was predicted as an indicator of combustion speed. The No.2-D diesel cetane number required by ASTM D975 33 was used as the criterion for pure POMEs.

The solubility of n-butanol in diesel fuel50 was used to determine the acceptable radius

of solubility (R, Eqn. 11) for POMEs in diesel, meaning that molecules will need to be more soluble than butanol in diesel fuel to meet this criterion. This limit was chosen for R because butanol has been studied as a diesel blendstock and demonstrates acceptable diesel solubility57.

The ratio YSI/LHV was used to evaluate the sooting tendency as a function of energy output per kilogram of fuel. The limit for this criterion was calculated by using a maximum YSI of 64 and a minimum LHV of 26.5 MJ/kg as described above. The YSI limit of [64] is 75% lower than the value (YSI = 246) that was measured for a certification diesel fuel using the procedures in Section 2.6.2. This diesel fuel sample is described by Mueller et al.55 and it was assumed to have the same formula and molecular weight ($C_{13.2}H_{23.0}$; 181.4 g/mol) as the V2 surrogate defined in that work55 Water solubility and biodegradability were combined into one metric to evaluate the potential for environmental contamination. Molecules that are predicted not to be biodegradable must be at least one order of magnitude less soluble in water than MTBE, which has a predicted solubility of 19,800 mg/L35 in water. Highly soluble molecules that are predicted to be readily biodegradable pass this screen.

Table 1: Phase 1 screening criteria: fuel property focus

Property	**Requirement**	**Description/Significance**	**Reference/ Justification**
Boiling point	< 338 °C	Blendstock must boil below the T90 limit for conventional diesel	ASTM D975-20a
Melting point	< 0 °C	Cold weather operability	ASTM D975-20a
Flash point	> 52 °C	Safety of handling blendstock and finished fuel	ASTM D975-20a
LHV	> 26.5 MJ/kg	Fuel economy	Less LHV penalty than E_{10} gasoline
DCN	> 40	Indicator of combustion speed	ASTM D975-20a ASTM D6890
Solubility in diesel	R < 10.26 relative to conventional diesel	Blendstock must be soluble in conventional diesel fuel	More soluble than n-butanol

Table 2: Phase 2 screening criteria: environmental focus.

Property	Requirement	Description/ Significance	Reference/ Justification
YSI/LHV	< 2.415 kg/MJ	Prevent soot formation in combustion	YSI 75% below the YSI of diesel. LHV criterion as defined in Phase 1.
Environmental fate	If non-biodegradable, water solubility must be < 1980 mg/L	Prevent environmental contamination	Non-biodegradable molecules must be 10 times less soluble than MTBE

2.2.6 Measurement of POME Properties for Model Evaluation

2.2.6.1 LHV

The HHV of the purchased/purified POMEs with alkyl group of C1 or greater (MM-$POME_1$, EE-$POME_1$, and BB-$POME_1$) were determined using an IKA-C200 calorimeter. Approximately 1.0 g of sample was used in each measurement. Measurements were conducted with the bomb calorimeter under excess pure oxygen at 3.0 MPa. The LHV was then calculated using Equation 8.

2.2.6.2: YSI

The sooting tendencies of the POMEs were measured using the yield-based approach we developed earlier 58. The specific procedures and apparatus used in this study are described in McEnally et al.54. The procedure consisted of three steps: (1) we sequentially doped 1000 ppm of n-heptane, toluene, and each POME into the fuel of a nitrogen-diluted methane flame; (2) we measured the maximum soot concentration in each flame with line-of-sight spectral radiance (LSSR); and (3) we rescaled the measured signals into YSI values using:

$$\mathrm{YSI_{POME}} = (\mathrm{YSI_{TOL}} - \mathrm{YSI_{HEP}}) \times \frac{\mathrm{LSSR_{POME}} - \mathrm{LSSR_{HEP}}}{\mathrm{LSSR_{TOL}} - \mathrm{LSSR_{HEP}}} + \mathrm{YSI_{HEP}} \quad (18)$$

where the subscripts POME, TOL, and HEP refer to the test POME, toluene, and n-heptane. This rescaling method factors out many sources of systematic uncertainty such as errors in the gas-phase reactant flowrates. Furthermore, it allows the new results to be quantitatively compared with a database 59 that contains measured YSIs for hundreds of organic compounds. The parameters YSI_{TOL} and YSI_{HEP} are constants that define the YSI scale; their values—170.9 and 36.0—were taken from the database so that the newly measured YSIs would be on the same scale. The YSI for each POME was measured three times. Isooctane was used as an internal standard and its YSI was measured 10 times over the course of this study. The values were consistent over time, their average (63.2) agreed with earlier studies (61.7),43 and their standard deviation was 1.2%. For compounds with very low YSIs – including all of the POMEs in this study – the overall uncertainty is ±5 YSI units54. This estimate includes random uncertainty based on two standard deviations of the YSI measured for the internal standard and systematic uncertainty due to possible errors in the dopant mass densities that were used to calculate the syringe pump flowrate corresponding to 1000 ppm.

2.2.6.3 Flash Point

All tests were performed using the PMA4 automated closed-cup tester with 45mL of fuel. This is a deviation from the D93A standard (70 mL fuel) due to the limited availability of POMEs. Tests with 1-pentanol, which has a similar T_{flash} range, showed no difference between 30, 50, and 70 mL tests, indicating that the evaporating fuel reached equilibrium with the air sufficiently rapidly in this volume range as long as the temperature probe was submerged.

2.2.6.4 Cetane Number

Cetane number was measured using an Advanced Fuel Ignition Delay Analyzer (AFIDA) instrument according to ASTM D8183-18.

2.3 Results

2.3.1 Predicted Properties of Linear and Branched POMEs

Sixty-seven POMEs were evaluated including linear structures of backbone length n = 1-7 and alkyl end groups of length C1-C5 as well as structures with isopropyl and isobutyl end groups, and structures with a tertiary alkyl branch of length C1-C4. To illustrate trends in the properties, predicted values of the parameters used in the two screening phases are presented in Table 3 for a subset of structures, the linear POME molecules. Predicted values of Hansen solubility parameters are presented in Figure 4.

2.3.2 Predicted Properties of POME/Diesel Blends

To evaluate the performance of POMEs as diesel fuel blendstocks, blending effects must also be considered. The T_{flash}, LHV, and YSI of selected POMEs blended at 10 – 50% in diesel were estimated to evaluate the potential of these formulations (Table 4). Complete results are available in Supplementary Materials.

2.3.3 Measured Properties of POMEs

Measured values for LHV, YSI, T_{flash}, water solubility, and DCN measured in this study are reported in Table 5.

Table 3: Predicted fuel properties of some pure linear POMEs. Values highlighted in darker orange are more favorable.

Species		LHV (MJ/kg)	YSI	YSI/LHV	T_{boil} (°C)	T_{melt} (°C)	T_{flash} (°C)	DCN	Water Solubility (mg/L)	Bio-degradable?
POME1	MM	23.2	4.5	0.2	48.0	-95.4	-38.9	53.2	1.3E+05	YES
	EE	28.8	14.4	0.5	98.0	-69.5	-4.8	81.5	2.2E+04	YES
	PP	32.0	27.3	0.9	144.4	-44.7	26.9	87.2	2.8E+03	YES
	BB	34.1	40.2	1.2	187.2	-20.9	56.1	99.0	3.0E+02	YES
	PePe	35.5	53.1	1.5	226.4	1.8	82.9	103.3	7.1E+01	YES
POME2	MM	21.2	5.7	0.3	99.0	-63.8	-4.2	79.0	2.8E+05	YES
	EE	25.9	15.6	0.6	145.3	-39.0	27.5	98.9	3.1E+04	YES
	PP	29.0	28.5	1.0	188.0	-15.2	56.7	100.4	3.4E+03	YES
	BB	31.2	41.4	1.3	227.1	7.5	83.3	108.3	3.7E+02	YES
	PePe	32.9	54.3	1.7	262.6	29.1	107.6	110.8	3.8E+01	YES
POME3	MM	20.0	6.9	0.3	146.2	-33.2	34.1	96.9	3.6E+05	NO
	EE	24.1	16.8	0.7	188.8	-9.5	48.7	109.9	3.9E+04	NO
	PP	27.0	29.7	1.1	227.8	13.2	62.7	109.5	4.1E+03	NO
	BB	29.1	42.6	1.5	263.2	34.8	76.1	115.2	4.3E+02	YES
	PePe	30.8	55.5	1.8	295.0	55.3	129.7	116.6	4.4E+01	YES
POME4	MM	19.3	8.1	0.4	189.6	-3.8	57.7	108.3	4.4E+05	NO
	EE	22.9	18.0	0.8	228.5	18.8	84.3	117.6	4.7E+04	NO
	PP	25.5	30.9	1.2	263.9	40.4	108.5	116.2	4.8E+03	NO
	BB	27.6	43.8	1.6	295.6	61.0	130.1	120.4	4.9E+02	NO
	PePe	29.2	56.6	1.9	323.7	80.4	149.3	121.1	5.0E+01	NO
POME5	MM	18.8	9.3	0.5	229.3	24.5	84.8	116.2	5.3E+05	NO
	MB	23.2	27.2	1.2	280.8	56.5	120.0	121.2	1.7E+04	NO
	BB	26.3	38.5	1.5	324.2	86.1	149.7	124.6	5.6E+02	NO
POME6	MM	18.4	10.5	0.6	265.2	51.8	109.4	122.0	6.1E+05	NO
	MB	22.4	28.3	1.3	311.2	82.1	140.8	125.5	2.0E+04	NO
	BB	25.3	46.2	1.8	349.2	110.1	166.7	127.9	6.3E+02	NO
POME7	MM	18.1	42.3	2.3	297.3	77.9	131.3	126.5	7.0E+05	NO

Greatly Exceeds Criteria — Does not meet Criteria

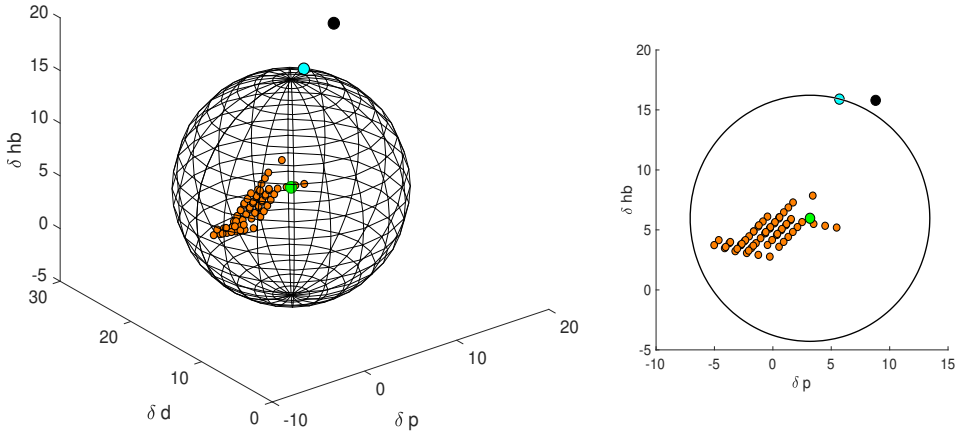

Figure 4: Hansen solubility diagram showing the Hansen solubility parameters for all 67 POMEs (orange) relative to conventional diesel fuel 50 (green). The radius of the sphere of solubility was determined from the Hansen solubility parameters of n-butanol 50 (blue). Ethanol[65] (black), which is known to have very poor solubility in diesel fuel, is outside of the identified sphere of solubility.

Table 4: Blend properties for 10% and 50% POME/diesel blends of POMEs passing both screening phases. Results for intermediate blends are in Supplementary Materials.

Species		**LHV**		**$T_{flash, mix}$**		**YSI**	
		10 vol%	**50 vol%**	**10 vol%**	**50 vol%**	**10 mol%**	**50 mol%**
$POME_1$	BB	41.9	38.4	88.9	66.1	223.0	136.8
	1P–PP	42.0	38.8	93.7	71.7	224.8	141.8
$POME_2$	PP	41.4	35.9	89.5	66.7	222.0	131.2
	EB	41.4	35.9	89.5	66.7	222.0	131.2
	PB	41.5	36.5	100.0	80.4	224.3	138.9
	iBiB	41.6	37.0	98.2	77.7	227.5	151.7
	1P–PM	41.5	36.5	94.1	72.2	224.0	137.2
	1E–PP	41.6	37.0	103.0	85.4	225.9	143.7
	1M – BP	41.6	37.0	103.0	85.4	225.9	143.7

Table 5: Measured POME properties.

Species		LHV (MJ/kg)	YSI	T_{flash} (°C)	DCN	Water Solubility (mg/L)
$POME_1$	MM	20.62	8.1 ± 5			387000 ± 18
$POME_1$	EE	27.80	15.5 ± 5	< 0		68500 ± 5
$POME_1$	PP		30.8 ± 5	33.4 ± 0.5	53.6 ± 0.4	3870 ± 0.6
$POME_1$	BB	33.82	44.8 ± 5	59.9 ± 1.1	74.7 ± 0.6	130 ± 05
$POME_3$	MM	19.78	2.8 ± 5	48.2 ± 0.3		421000 ± 29
$POME_4$	MM	19.6		85.6 ± 0.4		543000 ± 74
$POME_5$	MM	18.8		114.8 ± 1.2		442000 ± 40

2.4 Discussion

2.4.1. POMEs Predicted to Pass Phase 1 and 2 Criteria for Diesel Blendstocks

Using the predicted property values, the 67 POME candidates were evaluated using Phase 1 and Phase 2 screening criteria (Tables 1 and 2). Ten molecules passed through Phase 1 of the screening process, where the LHV, T_{melt}, and T_{flash} criteria eliminated most candidates. Generally, molecules either satisfied the criterion for T_{flash} or for T_{melt}, but not both. Phase 2 of the screening eliminated one additional molecule. All but three POMEs met the criterion for YSI/LHV, while many branched POME structures failed to meet the criterion for environmental impact. All POMEs satisfying the screening criteria (Fig. 5) have backbone length n = 1-2, but a variety of alkyl groups and branched structures are present.

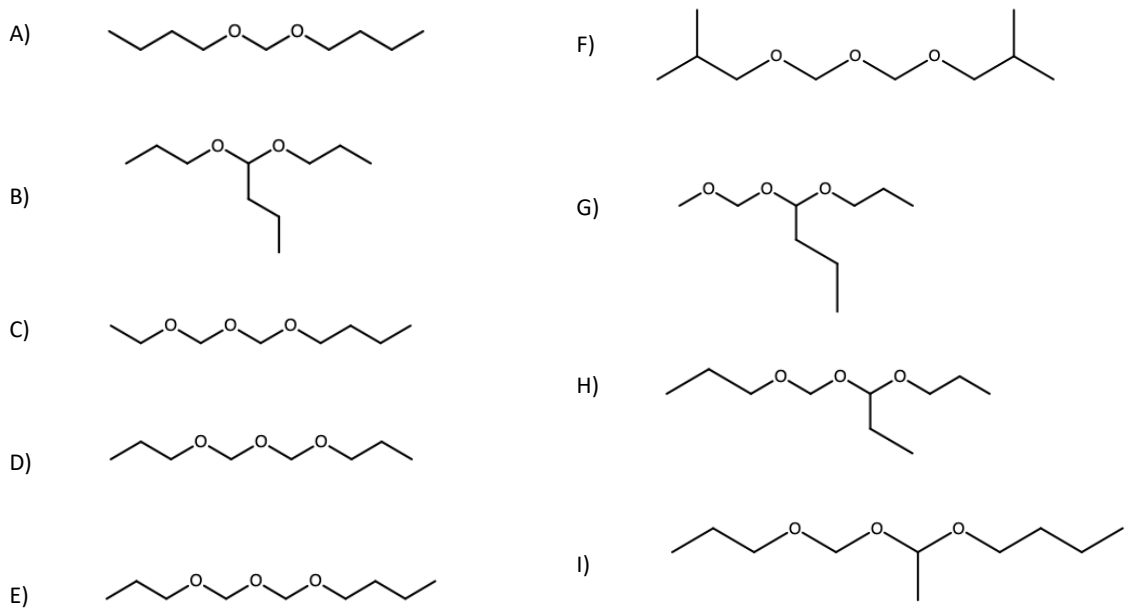

Figure 5: POMEs that passed Phases 1 and 2 of screening. A) BB-POME$_1$, B) 1P-PP POME$_1$, C) EB-POME$_2$, D) PP-POME$_2$, E) PB-POME$_2$, F) iBiB-POME$_2$, G) 1P-PM-POME$_2$, H) 1E-PP-POME$_2$, I) 1M-BP-POME$_2$

2.4.2. Effect of molecular structure on predicted POME properties

For a subset of the POMEs, the predicted fuel property results are presented in Tables S1 and S2, grouped to show trends in backbone length (n= 1-4) and linear or branched end-groups of different sizes (C1–C4). Figure 6 displays these results in a manner that enables visualization of trends in the properties. For cetane number and YSI, almost all of the structures meet the criteria. The YSI and YSI/LHV increase as end group size and POME backbone length increase. While increased oxygen content generally leads to decreased YSI, higher molecular weight results in increased sooting tendency. Thus, in the Kees of the POME structures, the higher molecular weight has a more significant impact than the higher oxygen content. LHV, which is generally low for all POME molecules, decreases as backbone length (and oxygen content) increases, resulting in an inversely proportional increase in the YSI/LHV ratio. There is an

31

incremental increase in the predicted LHV for each $POME_n$ chain length when the end group size increases, attributed to increasing the hydrocarbon-like attribute of the molecule. A similar trend with end group size was observed for T_{flash}, which increased significantly with increasing backbone length. The extremely low flash points of shorter POMEs could present a safety hazard. The property that most notably suffers from increasing backbone length is T_{melt}, with longer POMEs being solids at room temperature.

A marked reduction in water solubility was observed with increased end-group size for each backbone length, consistent with a hypothesis that larger end-groups would increase the hydrophobicity of the molecule and lead to a lower water solubility (Fig. 6). Increased molecular weight, whether from increased backbone length or increased end group size, led to higher T_{boil}.

POMEs with branched end-groups showed comparable predicted fuel property trends to those shown in Figures 6 and 7 for their linear counterparts with similar oxymethylene backbone lengths. Branched POMEs had similar predicted LHV as their linear analogs (same oxymethylene backbone and end groups) at the cost of higher YSI that resulted in increased predicted YSI/LHV ratios at longer backbones. Branched POMEs also had slightly lower boiling points and higher water solubility than their linear equivalents despite having similar molecular weight.

The importance of the end-group structure on small chain length POMEs, where the end-group makes up a larger portion of the overall structure, is exemplified by comparing the values for $POME_1$ and $POME_2$ molecules. For $POME_1$ molecules, the cetane number, LHV, T_{flash}, and water solubility values all improve upon exchange from MM to larger groups; in the case of LHV, T_{flash}, and water solubility, larger end groups result in the POME having property values that meet the criteria. Importantly, the calculated YSI values of all BB-$POME_n$ remain markedly

32

below the 246 value for conventional diesel fuel. Similar improvements were observed for $POME_2$, where PP and BB structures, along with their branched counterparts, meet the criteria for nearly all the properties.

It is helpful to identify indices for describing the molecules in terms of their oxymethylene backbones and alkyl end groups so that linear and branched structures can be compared directly and so that the contributions of these structures to POME properties can be described. Here, the Alkyl Index (AI) is defined as the total number of carbon atoms making up the alkyl end groups and tertiary alkyl branch of a POME. The Oxymethylene Index (OI) gives the number of oxygen atoms contained in oxymethylene backbone. The ratio of these indices can also be a helpful descriptor, as it indicates the extent to which the oxymethylene or alkyl structures dominate the overall molecular structure of a POME. This ratio, given by the oxymethylene index divided by the alkyl index, is called the O/A ratio.

To understand the effect of branching, branched and linear POMEs across a range of O/A ratios (0.25 – 4) were compared (Fig. 7). While there is not a defined trend between O/A ratio and values of YSI, CN, T_{flash}, T_{boil} and T_{melt}, lower O/A ratios (<1) favor higher LHV and lower water solubility across different POME lengths and linear or branched structures. This relationship is of great value since LHV and water solubility are the two fuel properties in which most POMEs are deficient. In a comparison of POMEs with the same OI and AI values but different branching (Table S3), the effect of branching on YSI is unclear, as some pairs show increased YSI with branching, while other pairs demonstrate lower YSI with branching. Values of T_{boil} and T_{melt} are affected favorably by branching, while T_{flash} is reduced. Most notably, branched structures are predicted to be recalcitrant to biodegradation. However, due to the lack of measurements for these modified POME structures, the predictive tools used in this study may

33

not fully capture the effects of branching on these properties.

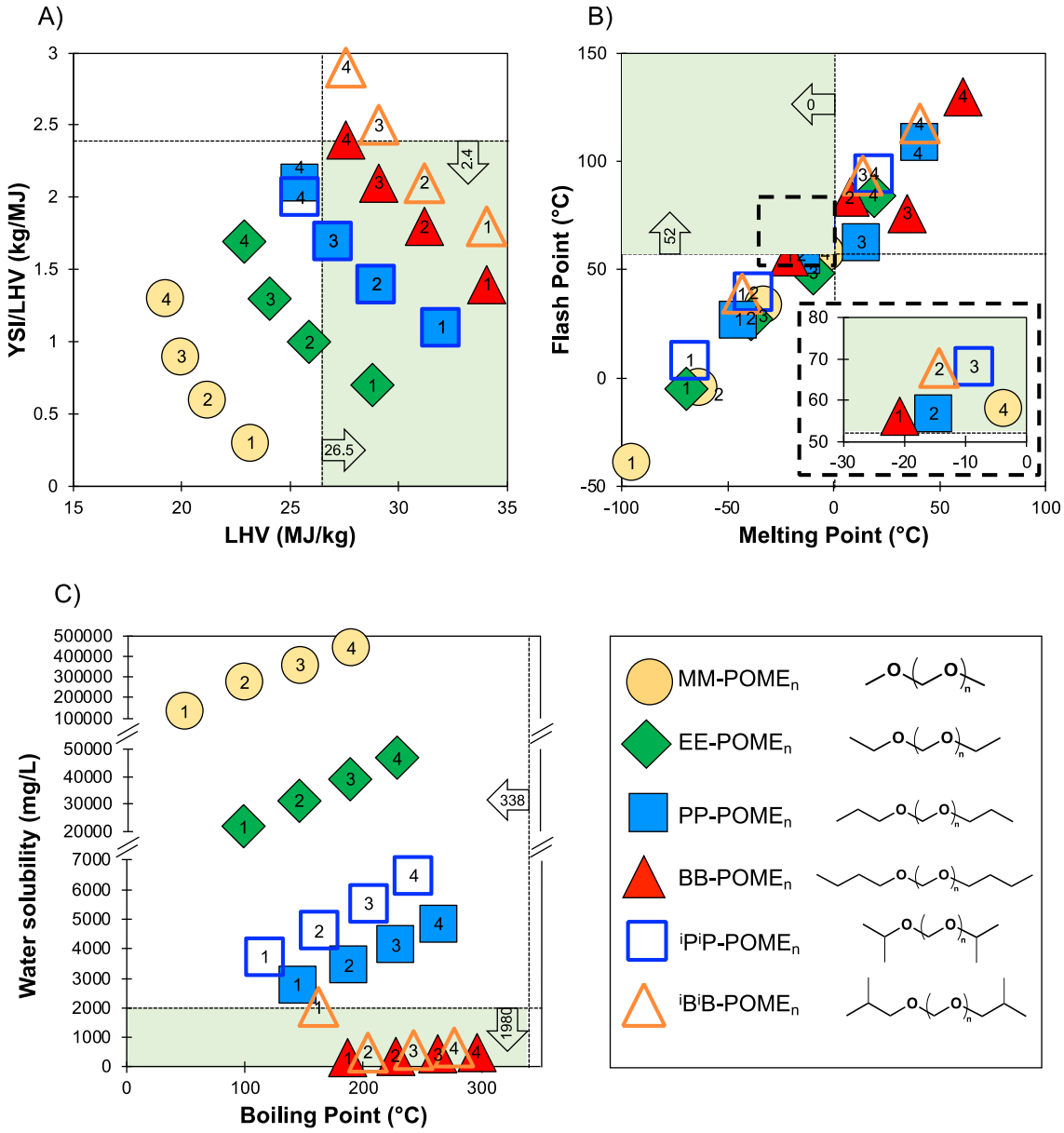

Figure 6. Relationships among predicted fuel properties and structures of linear POME$_n$ (n = 1–4) with linear and branched end groups (C1–C4). The screening criteria from Tables 1 and 2 are represented by dotted lines and targets are highlighted in light green. A) YSI/LHV and LHV, B) T_{flash} and T_{melt}, C) water solubility and T_{boil}. Numeration within the same marker type indicate the POME$_n$ chain length.

34

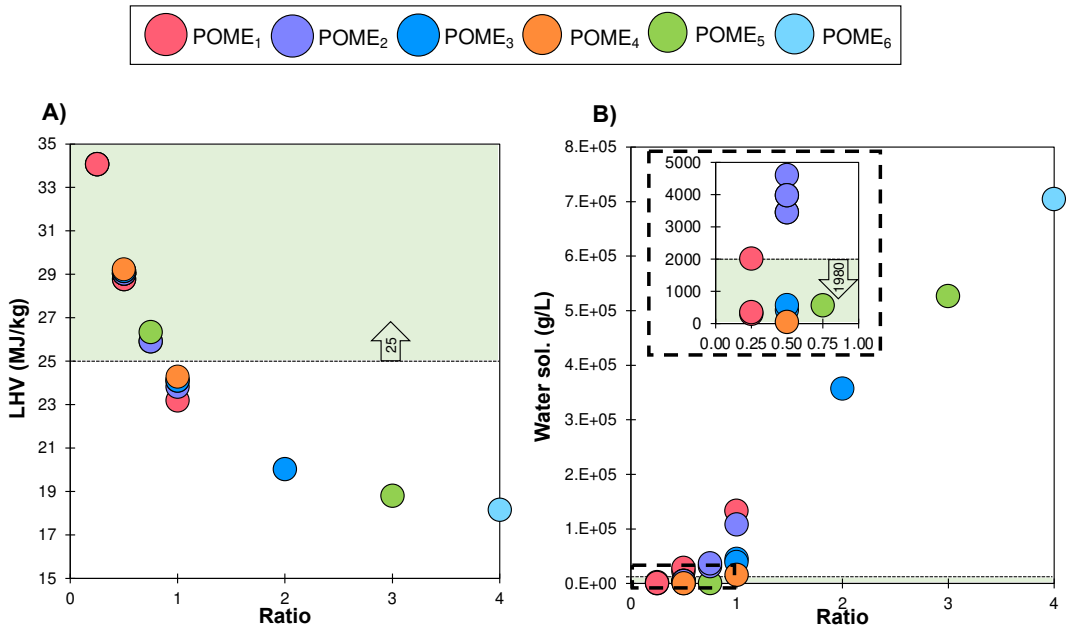

Figure 7. Relationships between A) LHV and B) water solubility with O/A ratio for linear POME structures. Dotted lines in B) show the region enlarged in the inset plot. The requirements of the screening criteria from Tables 1 and 2 are indicated by arrows that point to the fuel property improvement direction and targeted areas highlighted in light green.

2.4.3. Blending effects

The LHV, YSI, and T_{flash} of 10, 20, 30, 40, and 50% blends of POMEs in diesel fuel were also predicted (Table 4, Supplementary Materials). Blend properties are important to consider since POMEs will ultimately be used as diesel blendstocks. POMEs that passed through the screening are all predicted to have the potential to be blended at fractions as high as 50% and still meet LHV and T_{flash} criteria (Table 4). We note that the blending models implemented in this study are all based on ideal, linear blending behavior, which may not apply to POME/diesel blends.

2.4.4 Evaluation of predictive models

Measured data were used to evaluate the accuracy of the employed predictive tools for

35

evaluating POMEs (Tables 6 and 7). There are expected sources of error for each predictive model used. Models that only account for elemental mass fractions, such as those used to predict LHV, do not account for chemical groups or structural variations. These models are typically developed for a specific class of molecules and are not as accurate when applied to new structures. For example, the Dulong and Boie models used (Eqn. 5 and 6) in this study were developed for the analysis of coal 38.

Slightly more robust are group contribution methods. These models are designed to be applicable to multiple classes of molecules and account for chemical groups and differing structures. However, since POMEs, and the modified POMEs explored here, are novel molecules, group contribution methods are less able to properly account for these POME structures. The model used in this study for the calculation of ignition delay and DCN was developed for oxygenated hydrocarbons; however, because POMEs were not present in the training data, some amount of error is expected. A numerical issue arose in use of Equation 10, since DCN cannot be calculated for molecules with predicted ignition delays shorter than 1.512 ms. While POMEs are expected to have extremely short ignition delays, a new method for the prediction of DCN of POMEs would be beneficial. A group contribution method was also used for the estimation of POME solubility in diesel fuels. This method, while seemingly versatile, accounted poorly for POME structures. Although DMM is included in the training data for this method, and even appears as a secondary structure in the second-order groups, there is no way to consistently account for the structures of POMEs with longer backbones. The database for the group contribution model used to predict YSI contained three POME structures (MM-$POME_1$, EE-$POME_1$, BB-$POME_1$) on the date of accession 60. Only POMEs with backbone length n = 1 were included in this set, so the model may fail to extrapolate accurately to longer POME

36

structures.

Machine learning models, such as that used for the prediction of DCN, can be powerful tools when the training data includes sufficient information to capture the behavior of a given class of molecules. Machine learning model fitness depends heavily on the size of the training data set, and while several similar structures, such as triethylene glycol monomethyl ether, were included in the training data, no POMEs were used.

Average error and root mean square error (RMSE) were used to evaluate each model (Table 7). The R^2 values for the linear regression of predicted vs. measured values are also presented in Table 7. While a high R^2 value does not necessarily reflect the accuracy of a model, it provides insight to the relationship between a model's predictors and resulting property estimations. For example, the linear regression of predicted vs. measured values for the Prugh model (Eqn. 2) has the highest R^2 value of the T_{flash} models, yet it has the highest average error (Fig. 8). This implies that the Prugh model is a strong predictor of T_{flash} for POMEs but has a highly consistent error. In this case, the Prugh model consistently predicts the T_{flash} at an average of 32.4 °C lower than measured. In the event that were true for all of the POME T_{flash} predictions, only five candidates would pass both screening phases. Similar analyses of predicted vs. measured values for the other properties were also developed (Figs. S1–S5).

Table 6: Measured POME properties used to evaluate models. Values not marked with a citation were determined in this study (Table 5).

Species	**T_{boil} (°C)**	**T_{melt} (°C)**	**T_{flash} (°C)**	**LHV (MJ/kg)**	**DCN**	**YSI**	**Water Solubility (mg/L)**

37

$POME_1$	MM	42.361	-10561	-3261	20.62	5061	8.1	387000
$POME_1$	EE	8861	-6661		27.8	47 26	15.5	68500
$POME_1$	PP			33.4		53.6	30.8	3870
$POME_1$	BB			59.9	33.8	74.7	44.8	130
$POME_2$	MM	105[77]	-70[77]			68[38]		
$POME_2$	EE	140[78]	-45[38]	36[38]	25.7[38]	63[38]		
$POME_3$	MM	155.9[77]	-43[77]	48.2	19.78	72[38]	2.8	421000
$POME_3$	EE	185[78]	-24[38]	68[38]3.7[38]	67[38]			
$POME_4$	MM	201.8[77]	-10[77]	85.6	19.6	84[38]		543000
$POME_4$	EE			95[38]	19.6	70[38]		
$POME_5$	MM	242.4[77]	18[77]	115	18.8	93[38]		442000

Table 7: Statistical evaluation of models used in this work by comparing predicted (Table 3) vs. measured (Table 6) values.

Property	**Model**	**Average Error**	**RMSE**	**R^2**
T_{boil}	Adapted Stein and Brown	6.8%	8.84	0.986
T_{melt}	Mean or Weighted T_{melt}	9.1%	8.41	0.983
T_{flash}	Butler (Eqn. 1)	22%	16.8	0.963
T_{flash}	Prugh (Eqn. 2)	59%	32.8	0.991
T_{flash}	Prugh Alcohols (Eqn. 3)	24%	13.5	0.992
LHV	Dulong (Eqn. 5)	4.9%	1.19	0.967
LHV	Boie (Eqn. 6)	4.3%	0.99	0.971
LHV	Lloyd and Davenport (Eqn. 7)	2.7%	0.97	0.969
DCN	Machine learning model	43%	30.4	0.45
DCN	Group contribution model	240%	387	0.46
YSI	Machine learning model	44%	3.59	0.973
Water Solubility	Octanol/water partition coefficient	50%	112000	0.80

38

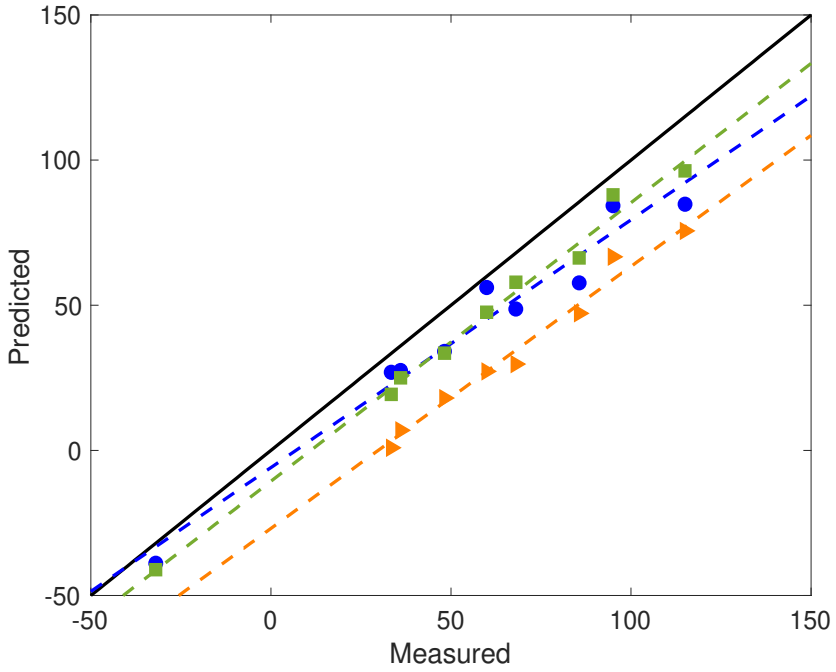

Figure 8: Predicted vs. measured values for T_{flash}. Solid black line: predicted = measured. Blue circles: Butler model (Eqn. 1) predictions vs. measured data. Orange triangles: Prugh model (Eqn. 2) predictions vs. measured data. Green squares: Prugh Alcohol model (Eqn. 3) vs. measured data. Dotted blue line: linear regression of predicted vs. measured values for the Butler model. Dotted orange line: linear regression of predicted vs. measured values for the Prugh model. Dotted green line: linear regression of predicted vs. measured values for the Prugh Alcohol model.

2.5 Conclusions

In this study, the fuel properties of 67 POMEs were predicted and used to identify promising diesel blendstock candidates. Nine POMEs are predicted to have structures that provide for substantial reduction in soot emissions compared to conventional diesel fuel while retaining or improving fuel properties appropriate for blending in diesel. Short chain length POMEs (OI = 1–2) and AI 6–8 appear to be most promising, with all nine identified POMEs belonging to this subset of POME structures. Further studies are necessary to assess the validity of structure–activity models for branched POME structures, as branching would likely have effects not captured by these models.

39

The models used in these predictions were shown to have a wide range of accuracy and those predictive tools should be revised by incorporation of POME measurements. In some cases, such as for LHV and T_{boil}, existing models provided highly accurate predictions despite having no POME structures in the training data. The finding that some models have high R^2 values and high error, such that they consistently overestimate or underestimate property values, could be used to propose a more accurate versions of those models for use with POMEs.

We note that the screening of POME structures was based on pure component values rather than on the properties of their blends with diesel. Considering that POMEs will be used in blends, it may also be reasonable to relax certain screening criteria. This would allow consideration of additional molecules that did not pass the original screening criteria but might have other advantages, such as ease of synthesis. As examples, PePe-$POME_1$, PB-$POME_1$, MP-$POME_2$, and EP-$POME_2$ all pass environmental screening and would pass through a slightly relaxed fuel property screen. Generally, POMEs with an O/A ratio of 0.2–0.6 may be viable diesel blendstocks.

Many of the POMEs identified in this work have yet to be synthesized, and most have not been produced on an industrial scale. Future research should focus on improving the synthesis of promising POMEs identified in this study and experimentally determining the performance of those molecules in diesel blends.

40

CHAPTER 3: BIOELECTROCHEMICAL METHODS AND REACTOR DESIGN FOR ELECTRO-ENHANCED BIOPROCESS TECHNOLOGIES

3.1 Introduction

3.1.1 Bioelectrochemical Systems

Bioelectrochemical systems are technologies that integrate living cells or enzymes with electrical circuits. These technologies can catalyze the conversion of energy between chemical bonds and electrical current, while taking advantage of the unique properties of cellular machinery. BES encompass a diverse range of biotechnologies, and by this broad definition, even some types of biosensors could be considered BES. Typically, though, we distinguish BES from other biotechnologies like biosensors in that BES are typically biochemical process technologies where the end goal is the production of energy or a substance, rather than detection or quantification of an analyte. The scope of BES considered here is limited to live cultures of bacteria interacting with a solid electrode. Even within this narrowed scope, BES can take many forms.

One way to further divide BES is based on the direction of electron flow. In anodic BES, chemical energy is converted to electrical energy, as electrons move from cells to an electrode (anode). As these cells metabolize soluble chemical substrates, they pass electrons to a solid electrode as a terminal electron acceptor in respiration, generating an electrical current.

In cathodic BES, electrons flow in the opposite direction, using living cells to transform electrical energy into chemical bonds. Here, cells can utilize electrodes as insoluble electron donors, accepting electrons and integrating them into cellular metabolism. The distinctions between subsets of cathodic BES are less clear: electro-fermentation (e-ferm) is sometimes considered a subset of microbial electrosynthesis (MES). We will define e-ferm and MES as

41

distinct categories of BES, where MES involves the bacterial reduction of CO_2 to acetate or other soluble metabolites, and e-ferm involves the fermentative metabolism of soluble carbon sources such as glucose to produce alcohols and organic acids.

We can also classify BES by the intended product. For example, in electro-fermentation, the intended products are soluble cellular metabolites, whereas in MFCs, the intended product is an electrical current. Figure 9 shows these branches of BES.

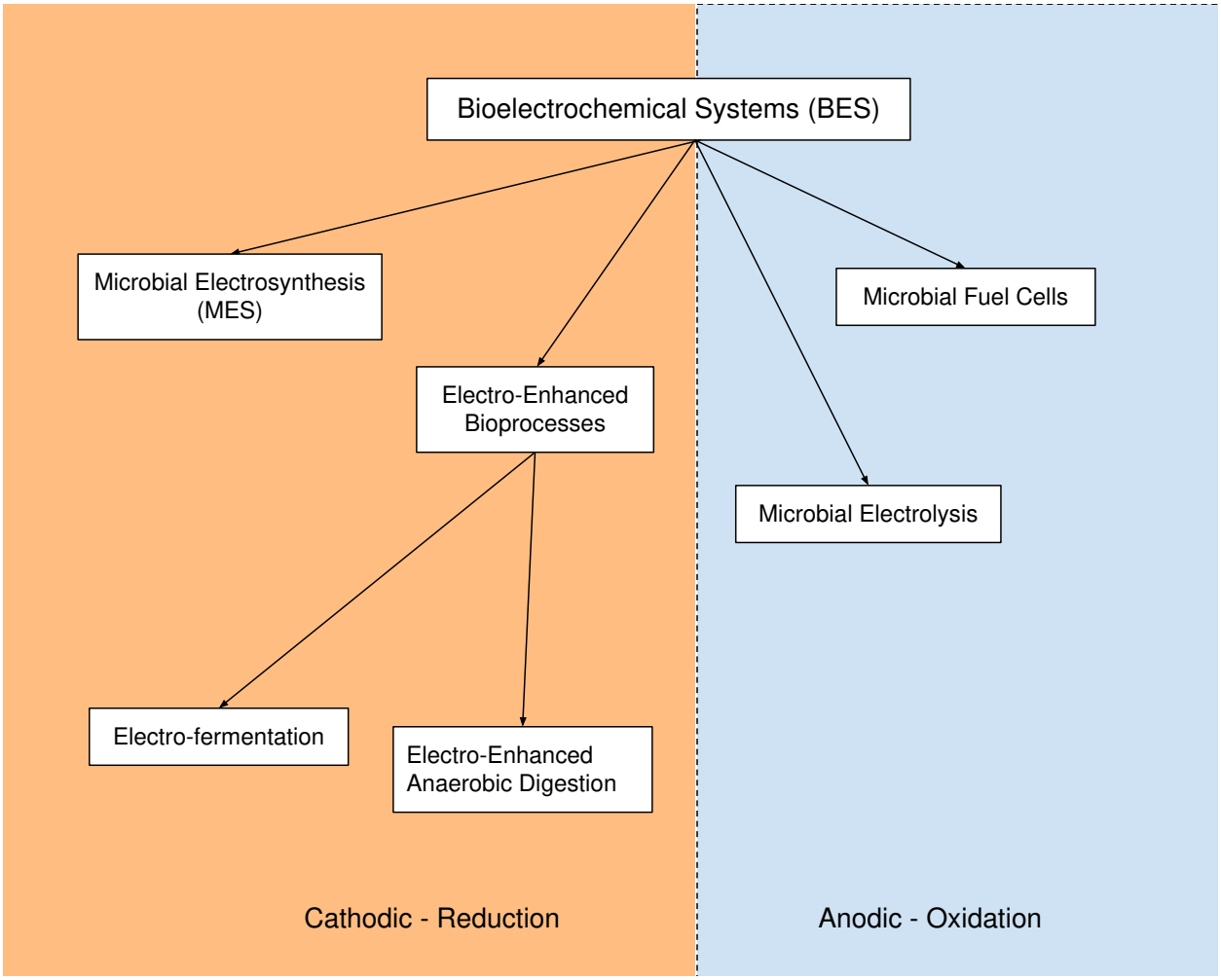

Figure 9: Bioelectrochemical systems can be categorized by the direction of electron flow (anodic and cathodic) as well as the intended product (electrical current or metabolic products).

42

BES can also be applied to technologies for waste valorization. In these mixed culture systems, applied potentials can affect processes occurring at both the community and cellular levels to influence conversion pathways from heterogeneous substrates to products of interest. While these branches of BES involve distinct processes and applications, they are united by the phenomenon of microbial extracellular electron transfer (EET): the transfer of electrons between microbe and electrode. Microorganisms that are capable of this transfer have been called *electroactive* species. Bacteria of the genera *Shewanella* and *Geobacter* are considered model electroactive organisms, and the mechanisms by which EET occurs in these species has been studied extensively in the context of anodic BES.

Several putative electron transfer mechanisms have been investigated for these organisms including direct transfer by membrane-bound cytochromes, conduction via bacterial nanowires, and indirect transfer by bacterial shuttle secretion[79–81]

. In both genera, it is hypothesized that outer membrane-bound cytochromes (OMCs) are integral to the EET mechanisms[79]. Some species of bacteria may be capable of secreting redox mediators and matrix-associated cytochromes or growing networks of nanowires within extracellular polymeric substances (EPS) to produce a current-generating biofilm[79,82]

While these mechanisms have been identified in a few model species, much remains unknown about microbial EET, especially cathodic transfer. There still exists discordance on how and why cells utilize EET mechanisms, how widespread this capability is, and how to study it. Several factors contribute to these inconsistencies in BES literature. First, the sensitivity of these mechanisms to environmental stimuli demands extremely well-controlled conditions. For example, even in low levels of oxygen, *Shewanella* species will favor aerobic respiration, using oxygen as a terminal electron acceptor rather than a solid electrode. Electrode materials and roughness, substrate availability, and electrode potential also play a significant role in the

43

electroactive behavior of bacteria. Many studies have failed to properly control for all variables or have not investigated multiple conditions. Others fail to consider the effect of background electrochemistry and the effects of unwanted electrochemical and redox phenomena on experimental results. Second, there are no standard methods for evaluating or quantifying EET. The majority of the electro-fermentation literature relies on purely observational studies that fail to probe microbial electroactivity and result in oversimplified conclusions. Third, the application of electroanalytical techniques to living cells, biofilms, and their components is difficult and requires rigorous evaluation of the electrochemical system being employed.

3.1.2 Anodic Bioelectrochemical Systems

The vast majority of BES research has focused on anodic systems. Extensively studied electroactive species of *Shewanella* and *Geobacter* have been known as dissimilatory metal-reducing bacteria (DMRB) for decades [80,81,83–91]. Lovley et al. first isolated *Geobacter metallireducens* from marine sediments in 1987 and observed that this species could utilize ferric iron as a terminal electron acceptor[92,93]. This was the first report of dissimilatory metal reduction, which differs from the assimilatory, intercellular use of iron by fermentative bacteria[92,94]. Other species of DMRB, such as *Geobacter sulfurreducens* and *Shewanella putrefaciens* were subsequently identified as major constituents in the biogeochemistry of sedimentary environments[94–96]. Further investigations of DMRB revealed that some species could use diverse inorganic terminal electron acceptors, both soluble and insoluble[93]. This finding had significant implications in biogeochemistry and remediation of marine environments, as these organisms showed potential for in situ remediation of metal-contaminated ground and surface water[93,94].

44

Beyond the ecological implications, these findings held evolutionary significance, as metal reduction may have predated other respiratory processes[94,97].

In 1998, Kim et al employed electroanalytical techniques to characterize the redox proteins known to be involved in dissimilatory metal reduction by *Shewanella putrefaciens*. In doing so, they demonstrated for the first time that live, intact bacterial cells could interact directly with an electrode, giving rise to the field of BES [90]. The study of DMRB in marine environments then resulted in the conceptualization of the microbial fuel cell when it was demonstrated that electrodes embedded in marine sediment could generate an electrical current[98]. Natural biogeochemical processes at the sediment-water interface result in a potential drop within the top few centimeters of marine sediment, which was shown to act as a fuel cell when embedded with an electrode[98]. Microbial community analysis of anodes from a variety of sediments showed significant augmentation of known metal-respiring *Geobacter* species, suggesting that the current may have resulted from direct electron transfer from sediment bacteria to the anode rather than from abiotic biogeochemical processes[88]. Bond and Lovley then demonstrated for the first time that electricity could be generated by direct microbial electrode respiration using *Geobacter sulfurreducens*[86]. These findings laid the foundation for the development of diverse microbial fuel cell technologies. In situ systems, like the marine sediment fuel cell[98], enable long-term power generation from continually renewed electron sources, while other MFC technologies could couple power generation with organic waste treatment.

3.1.3 Cathodic Bioelectrochemical Systems

45

While microbial fuel cells have shown potential for certain applications, the low current densities generated in these systems limit their utility as major renewable energy technologies. Our power and transportation systems rely on energy-dense carbon-based fuels, where energy can be stored infinitely in the form of chemical bonds to be extracted on-demand.

Fermentation is a bioprocess of industrial interest to produce valuable, reduced metabolites such as organic acids and alcohols. Fermentation is an anaerobic process in which organic molecules serve as terminal electron acceptors to regenerate NAD^+ for glycolysis. Because fermentation is controlled by this redox balance, yields of more reduced metabolites, which require more electrons in the form of reducing equivalents, are limited by redox constraints such as the reduction potential of the substrate.

Early efforts to alter fermentative pathways with redox control focused on the use of soluble redox mediators. In 1979, Hongo and Iwahara showed that L-glutamic acid production was increased in *Brevibacterium flavum* fermentations with cathodic applied potentials mediated by neutral red[99,100]. In 1988, Kim and Kim demonstrated that electrochemical energy could be used as a reducing equivalent in fermentation mediated by methyl viologen, leading to a 26% increase in butanol production[101]. While these results demonstrate that redox potential can be used to create "unbalanced fermentations", the use of redox mediators like neutral red and methyl viologen on a large scale is not ideal due to the cost and toxicity of these chemicals. To induce these metabolic shifts electrochemically without supplemented soluble mediators, direct interaction between electrode and microbe is required. This interaction may include any combination of microbial EET mechanisms, including secreted redox mediators. Here, we use the term electro-fermentation to discuss electro-enhanced fermentations without the use of

46

exogenous redox mediators. Figure 10 illustrates the concepts of mediated and unmediated electro-fermentation.

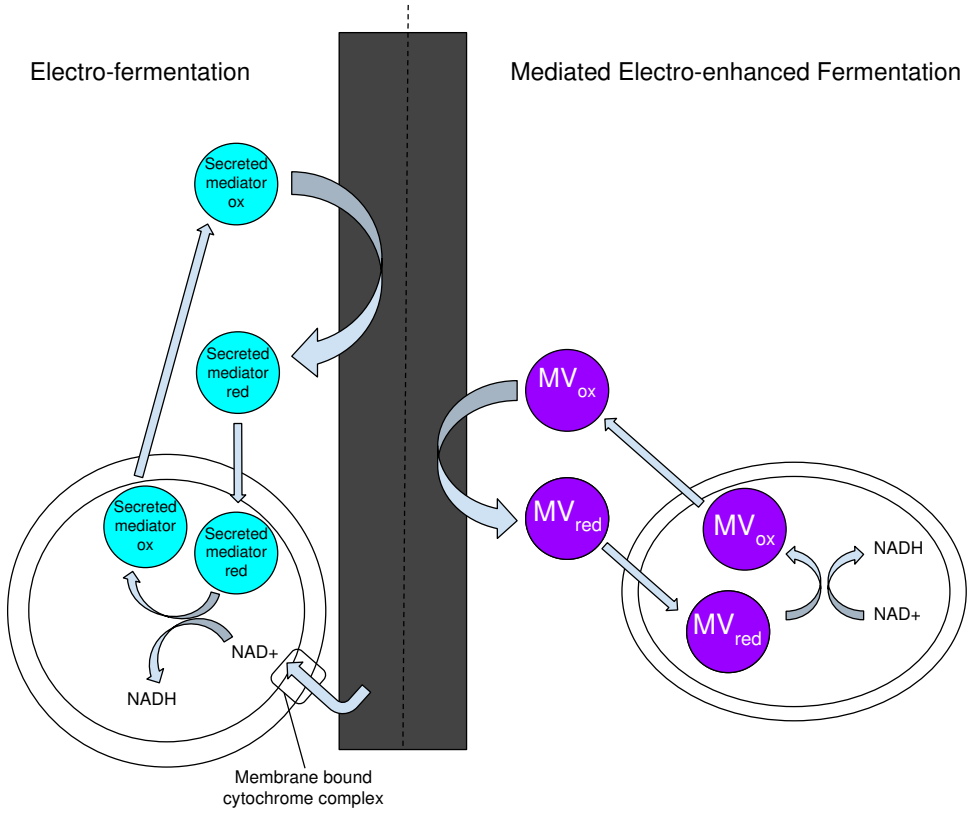

Figure 10: We define electro-fermentation as direct interaction between microbe and electrode without the use of supplemented redox mediators, whether it be the secretion of biological redox molecules or direct electron transfer via membrane bound cytochromes and cellular appendages.

Gregory et al first demonstrated that a cathode could act as direct electron donor in 2004, when they observed that *G. sufurreducens* could grow and reduce fumarate to succinate with a cathode serving as the sole electron donor[102]. It was later shown that this cathodic electron transfer mechanism shared almost no components with its anodic analog[103]. Ross et al. reported cathodic electron transfer in *Shewanella* as well, and further, using sequential gene knockouts, suggested that the electron transfer occurred using the same Mtr pathway in reverse[89,104]. In a

47

separate study that employed protein film voltammetry, it was shown that electron transfer among the outer membrane MtrABC complex proteins was not reversible[104]. These results suggest that, while some proteins involved in anodic electron transfer may also be required for cathodic transfer, the pathway is likely different.

Electro-fermentations of many species have been reported in the literature[105–111] Studies of *Clostridial* species, such *as C. thermocellum*, *C. acetobutylicum*, and *C. pasteurianum* demonstrated significant promise for electro-fermentation as a tool for improved productivity and yield of desired metabolites[106,107,110–112]. However, most of these studies are primarily observational and do not elucidate possible mechanisms of electron transfer in these species. Electro-fermentations of yeasts such as *Saccharomyces cerevisiae* have also been explored, although no direct evidence for electroactivity of yeast has been presented[105,106] Because the majority of literature in this field relies on observational studies with poorly controlled conditions, much remains unknown about cathodic direct electron transfer and extracellular electron utilization in fermentative pathways. The shortcomings of these studies will be explored further in sections 3.2 and 3.3.

Microbial electrosynthesis has also emerged as a cathodic BES. MES is defined as the microbially-catalyzed reduction of carbon dioxide into organic metabolites at a cathode. With abundant carbon in the form of atmospheric CO_2, technologies for the reduction of CO_2 into industrially valuable fuels and chemicals could provide low carbon alternatives to petroleum-based processes that may be amenable to current carbon-based infrastructure. While abiotic electrochemical and catalytic conversion technologies for CO_2 reduction exist, the ability to exploit cellular machinery through a biologically catalyzed process offers the advantages of improved long-term stability, catalyst regeneration, product specificity, and efficiency[113,114].

48

While microbial electrosynthesis offers the benefit of a virtually inexhaustible, inorganic carbon source, it is limited by the requirement of a lithoautotrophic or lithoheterotrophic metabolism.

3.1.4 Extracellular Electron Transfer Mechanisms

Several putative mechanisms for extracellular electron transfer have been identified, including membrane bound cytochromes, conductive cell appendages, and secreted redox mediators[79,84,115,116]. It has long been understood that C-type cytochromes were involved in electron transport chains for dissimilatory metal reduction[84,93,117–125]. *Shewanella* and *Geobacter* consist of gram-negative bacteria, which possess an inner and outer membrane enveloping a periplasmic space. In both genera, transmembrane and periplasmic proteins involved in electron transport across this cell envelope have been identified. In *G. sulfurreducens*, OmcE and OmcS are proteins located on the cell surface that are believed to play a role in EET[84,125]. In *S. oneidensis,* proteins MtrC and OmcA are believed to form transmembrane protein complexes for EET[84]. Conductive cell appendages have also been identified as putative EET mechanisms[82,111,126]. These appendages are believed to help with attachment and electron transfer to insoluble electron acceptors[82]. These appendages are believed to interact with membrane-bound cytochromes for electron transfer and aid in the formation of conductive biofilms[82,84]. Secreted redox mediators have also been identified as mechanisms for facilitating microbe-electrode interactions in known DMRB. Marsili et al. and Von Canstein et al. identified flavins secreted by electrode biofilms of *S. oneidensis* and demonstrated that these molecules increased rates of electron transfer to electrodes[80]. Multiple mechanisms likely play a role in microbial EET, resulting in the formation of conductive biofilms (Figure 11) .

49

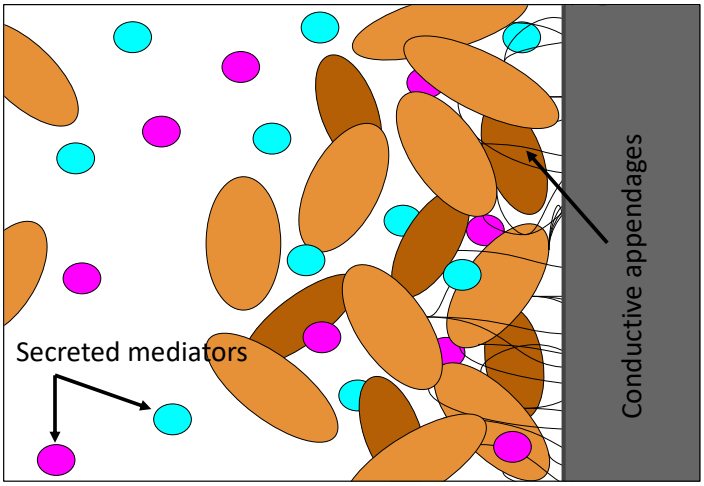

Figure 11: schematic of an electrode biofilm with conductive cell appendages as well as secreted mediators. Secreted redox molecules may remain in the biofilm matrix or diffuse into the supernatant.

While these mechanisms of EET have been studied extensively for gram-negative DMRB, less is known about EET in gram-positive bacteria or yeasts, which have also been proposed as electroactive organisms. Several species of clostridia have been implicated for BES applications, but due to the vastly different cell envelope structure that characterizes these gram-positive bacteria, it is unlikely that the mechanisms for EET resemble those identified in DMRB.

Light et al. used a genetic screen to identify genes responsible for EET in diverse gram-positive bacteria [127]. This mechanism was found to involve a dehydrogenase that may channel electrons to a membrane-localized quinone pool, where flavoproteins and secreted redox-mediating small molecule flavins facilitate electron transfer to electrodes and other extracellular acceptors[127]. Engel et al. identified both secreted flavins and conductive cell appendages in *Clostridium acetobutylicum* grown in BES.

3.1.5 Issues in the electro-fermentation literature

50

The literature in electro-fermentation and related technologies such as electro-enhanced anaerobic digestion contains shortcomings than can be divided into two distinct categories. The first is the failure to employ electroanalytical techniques to probe and measure extracellular electron transfer behavior, or the failure to properly adapt electrochemical techniques for biological systems. The second category is faulty BES reactor design. Here, we will discuss in detail the challenges and potential solutions to common pitfalls in these two categories.

3.2 Electroanalytical Techniques for Studying Microbial EET

3.2.1 Electroanalytical techniques

Electroanalytical methods are the standardized techniques for studying redox molecules in abiotic systems. These methods provide important information about the redox behavior of an analyte. An especially powerful and popular electroanalytical method is cyclic voltammetry (CV)[128]. CV involves applying linear sweeping voltage waveform to an electrochemical cell and measuring the resulting current response as a function of the applied potential. This cyclic process allows observation of the oxidation and reduction reactions of electroactive species and provides valuable information about their redox potentials, electron transfer kinetics, and diffusion coefficients.

3.2.2 Electrochemical analysis of live cells presents unique challenges

Just as no one would build a large-scale chemical plant without understanding the chemical process, we need to understand the behavior and conditions affecting microbial EET before designing bioelectrochemical systems. Electrochemical techniques can help elucidate mechanisms of EET by showing diffusion limitations, electrode adsorption, etc. Therefore, electroanalytical methods should be applied to cells, biofilms, and other fermentation

51

components as they would be applied to chemical analytes. However, many challenges arise in the application of electrochemical techniques to these complex biological systems.

Electrochemical techniques have been used to study redox active proteins, but even electrochemical analysis of purified proteins presents additional challenges beyond those encountered in traditional electrochemistry due to the fragility of enzymes and shielding of active sites[90,129]. Electrochemcial analysis of proteins often requires modification of electrode surfaces or proteins. Even greater complications arise in the study of living cells and biofilms, where proteins may be embedded in cell structures, hindering accessibility. Further, living cells and biofilms are constantly changing and responding to environmental stimuli, and different EET mechanisms may be present or absent under certain conditions. Finally, cells and biofilms may interact with and modify electrode surfaces. Despite these challenges, electroanalytical methods are an important tool for studying direct microbe-electrode interactions and are necessary for concluding whether a microorganism is electroactive.

Electrochemical techniques have been employed in the study of EET, but the literature is rife with inconsistencies that result from the complexities of microbe-electrode interactions. In 1998, Kim et al. first reported direct electrochemical interaction of intact bacterial cells with an electrode, performing fast scan rate (100mV/s) cyclic voltammetry on cell suspensions of *S. putrefaciens* using a glassy carbon electrode. They reported a quasi-reversible reaction centered at -0.145V vs SCE (+40mV vs. Ag/AgCl) for anaerobically grown cell suspensions[90]. While this work provided the first evidence that direct electrochemical interrogation of intact bacterial cells may be possible, we have observed that washed cell suspensions of *S. oneidensis* do not show any electroactive behavior at fast scan rates under any of the conditions we have investigated. Meitl et al. also performed fast scan rate cyclic voltammetry of washed S. *oneidensis* cell

52

suspensions, and, while they reported that their results corroborated those of earlier studies, such as those of Kim et al. they report a quasi-reversible reaction centered at -150mV vs. Ag/AgCl, rather than the +40mV vs. Ag/AgCl reported by Kim et al[130].

Marsili et al. and Baron et al. performed slow scan rate (1mV/s) cyclic voltammetry on *S. oneidensis* biofilms and demonstrated that, similarly to *G. sulfurreducens, S. oneidensis* exhibited catalytic turnover behavior in the presence of excess electron donor[80,131]. In lactate depleted biofilms, nonturnover behavior was observed, with two redox reactions centered at approximately -420 mV vs. Ag/AgCl and -150 mV vs. Ag/AgCl. The reaction centered at -420 mV was identified as a secreted riboflavin at the electrode-biofilm interface[80]. While the higher potential reaction observed corresponds to the quasi-reversible peaks observed by Meitl et al., it was hypothesized that the redox potential of this reaction was too high to be involved in the primary electron transfer process[80].

Srikanth et al. used pectin-entrapped *G. sulfurreducens* on graphite electrodes to electrochemically characterize electron transfer between bacteria and electrodes under several conditions. Cyclic voltammetry performed at 10mV/s revealed catalytic behavior indicative of electron turnover in oxidative metabolic pathways[116]. Marsili et al. reported the same catalytic wave response from *G. sulfurreducens* biofilms grown on glassy carbon electrodes[131].

The inconsistencies reported in the literature for electrochemical analysis of EET, especially for *S. oneidensis*, stem from the sensitivity of EET mechanisms in some species to growth and experimental conditions, as well as the lack of standardized methods for adaptation of electrochemical techniques to study microbial systems.

3.2.3 Techniques for Electrochemical Analysis of EET

53

Electrochemical analysis of biological systems involves additional considerations beyond traditional electrochemical methods. Here, we demonstrate some of the challenges associated with electrochemical analysis of bacterial suspensions and biofilms, as well as potential strategies for improved analysis of EET.

Shewanella oneidensis MR-1, *Lactococcus lactis*, *Escherichia coli* Nissle, *Saccharomyces cerevisiae*, and *Clostridium pasteurianum* were used to evaluate electrochemical techniques for studying EET under a variety of conditions. Known electrogen *S. oneidensis* served as a positive control.

3.2.2.1 Sensitivity to growth conditions

Shewanella are facultative anaerobes and have been shown to possess the most diverse respiration capabilities among all bacteria[79]. Electrochemical characterization of *S. oneidensis* cell suspensions, supernatant, and electrode biofilms demonstrate that EET mechanisms are expressed in response to environmental stimuli to facilitate growth and respiration under many conditions. Because of this metabolic diversity, *S. oneidensis* electroactivity, as observed in cyclic voltammetry, is extremely sensitive to growth and analytical conditions. Here, we use CV to demonstrate this sensitivity.

Figure 12 shows that *S. oneidensis* expresses EET mechanisms in response to depletion of a soluble electron acceptor. *S. oneidensis* biofilms were grown anaerobically on glassy carbon electrodes in tryptic soy broth (TSB) containing lactate as an electron donor and fumarate as an electron acceptor for 48 hours. After 48 hours of growth, one bioelectrode was transferred to anaerobic TSB lacking fumarate and incubated for an additional 4 hours. Both electrodes were then transferred to an anaerobic chamber, rinsed with phosphate buffered saline (PBS), and

54

submerged in PBS for CV analysis. IT should be noted that CV scans were performed sequentially, with the fumarate depleted biofilm scanned last to encourage further electron acceptor depletion.

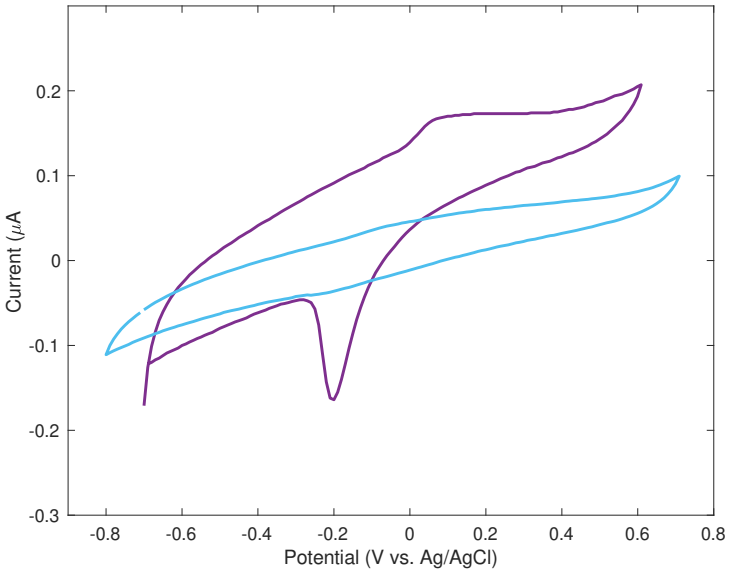

Figure 12: slow scan rate (1 mV/s) CV of anaerobic *S. oneidensis* biofilms in PBS on glassy carbon electrodes. The purple trace shows a biofilm grown with fumarte as an electron acceptor, then transferred to medium lacking fumarate for 4 hours. The blue trace shows a biofilm that was grown with excess fumarate, then immediately transferred to PBS for CV analysis.

S. oneidensis EET mechanisms also depend on oxygen availability. They are facultative species but will utilize oxygen as a terminal electron acceptor if it is present in levels as low as 10ppm. Following the same procedure described above, biofilms were grown on glassy carbon electrodes. Here, both biofilms were depleted of fumarate before analysis, but one biofilm was grown aerobically and the other anaerobically. CV was again performed in anaerobic PBS in an anaerobic chamber. The biofilm that was grown aerobically was scanned first to prevent metabolic changes. The aerobically grown biofilm does not exhibit the electron tranfer behavior seen in the anaerobic biofilm (Figure 13).

55

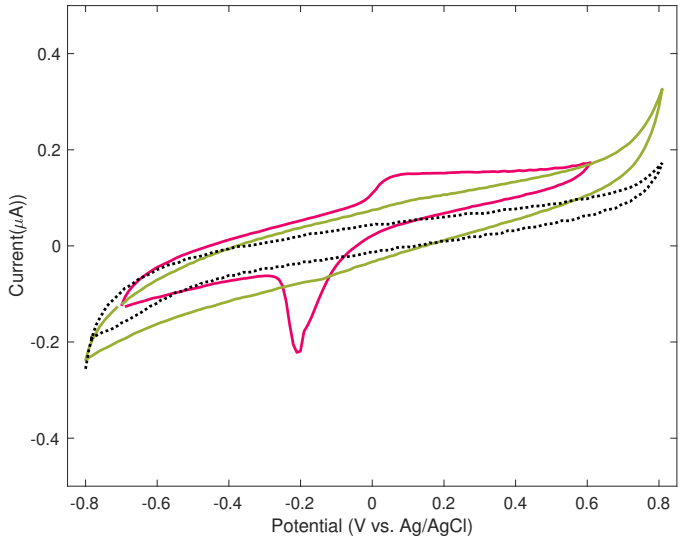

Figure 13: CV (1 mV/s) of an anerobically grown *S. oneidensis* biofilm (pink trace) and an aerobically grown *S. oneidensis* biofilm (green trace) shown with a background scan of anaerobic PBS.

3.2.2.2 Electrode cleaning

In abiotic electroanalytical research using glassy carbon electrodes, it is common to perform routine electrode polishing with 0.05 µm alumina slurry between experiments. In this procedure, 0.05 µm alumina is dispensed onto a microfiber polishing cloth with distilled water to form a slurry, the electrode surface is then held perpendicular to the cloth surface and gently moved in a rotating figure-eight pattern. The electrode is then thoroughly rinsed with DI to remove alumina particles from the surface[132]. Periodic cleaning may be performed with 0.3 µm and 0.05 µm slurries, sequentially, using the technique described. However, more aggressive cleaning with 5 µm slurry or a course grit paper is avoided, as this type of cleaning removes a substantial layer of the electrode surface, thus reducing its lifetime[132]. Aggressive cleanings are typically performed when a chemical species has non-specifically adsorbed to the electrode surface[132]. As researchers in BES do not typically disclose their electrode cleaning methods, it is unclear what techniques have been used to ensure complete biofilm removal in published studies.

56

However, many inconsistencies in the literature point to insufficient electrode cleaning. We have found that an aggressive cleaning is required between experiments to completely remove biofilms. Here, we demonstrate the importance of proper electrode cleaning and show how insufficient cleaning can lead to misleading results.

Improper electrode cleaning and failure to perform new background scans for each experiment can lead to false conclusions. Even when electrodes are stored without growth medium for long periods of time, residual biofilm materials can exhibit electroactive behavior. An electrode-respiring *S. oneidensis* biofilm was grown on a glassy carbon electrode, then transferred to sterile, anaerobic PBS in an anaerobic chamber for analysis. The electrode was left submerged in buffer containing no growth medium for 24 hours. After this period, cyclic voltammetry was performed (Figure 14 A). The electrode was then cleaned using a routine (0.05 µm) cleaning and stored with a rubber cover in open air for several weeks. Without obtaining a new background scan first, the same electrode was then incubated with *L. lactis,* and again CV was performed in sterile PBS in an anerobic chamber. The voltammogram obtained showed similar electrochemical behavior to that obtained from the *S. oneidensis* biofilm (Figure 14 B). The same procedure was repeated with *E. coli* Nissle, a biofilm forming strain of *E. coli*. Again, cyclic voltammetry showed similar electron transfer behavior to *S. oneidensis* (Figure 14 C). However, after aggressive electrode polishing was performed, this behavior was no longer observed in CV of *L. lactis* or *E. coli* biofilms under the same conditions (Figure 14 D). These results indicate that not only do biofilms require aggressive polishing for removal, but also that some components of EET mechanisms do not require active metabolism or even living cells. We

57

hypothesize that the single turnover reaction observed here was the result of electrode-adsorbed cytochromes or conductive cellular appendages.

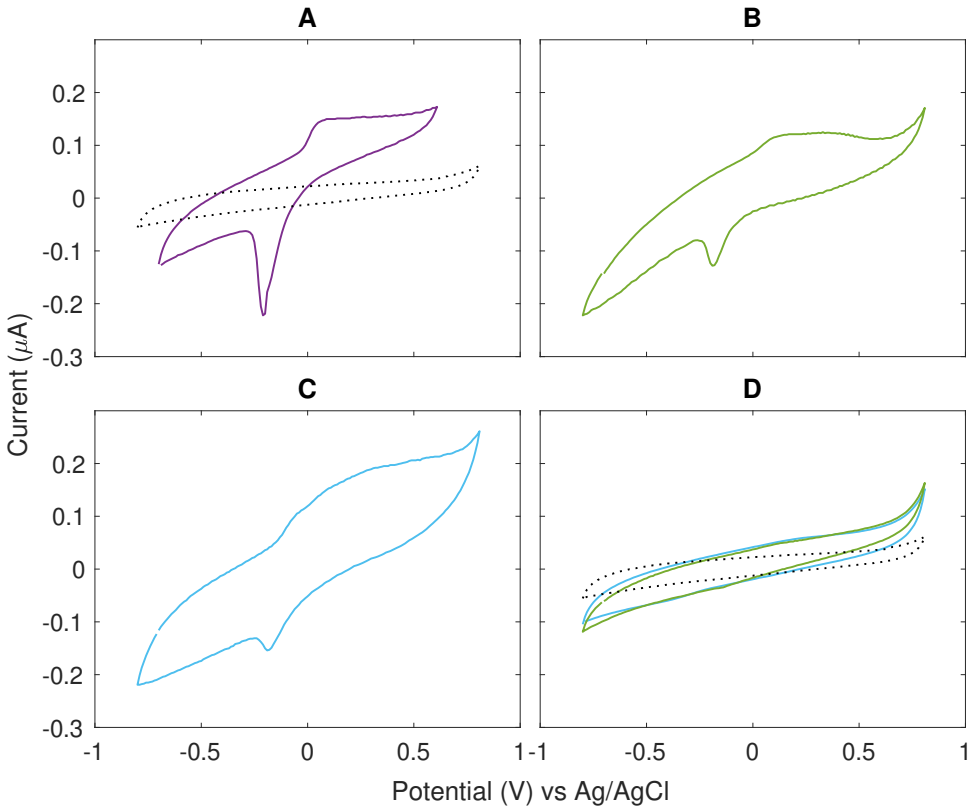

Figure 14: Cyclic voltammograms (1mV/s) demonstrating the importance of electrode cleaning and background scans. A: 48-hour anaerobic *S. oneidensis* biofilm in PBS (purple trace) with clean glassy carbon/PBS background (dotted black trace). B: 48-hour anaerobic *L. lactis biofilm* on an improperly cleaned electrode. C: 48-hour *E. coli* Nissle biofilm on an improperly cleaned electrode. D: *L. Lactis* (green trace) and *E. coli* Nissle (blue trace) after electrode was aggressively polished, with a new background scan demonstrating proper electrode cleaning between experiments (dotted black trace).

Confocal microscopy was used to verify that aggressive polishing is necessary for biofilm removal. A *C. pasteurianum* biofilm was grown anaerobically on a glassy carbon electrode by fitting the electrode to a butyl rubber stopper in a serum bottle, so that the electrode surface was suspended in bacterial culture. The serum bottle was filled with 100mL of reinforced clostridial medium (RCM) and purged with high purity nitrogen gas, then inoculated with 1mL glycerol stock and incubated at 37°C for 48 hours. After 48 hours, the electrode was washed gently with

58

sterile 0.85% NaCl and incubated in 0.85% NaCl with 10µM Syto-9 fluorescent DNA stain for 30 minutes at room temperature. After this incubation period, three sequential washing stages were performed using sterile NaCl. After washing, the electrode was immobilized to a glass slide using a laser-cut support with a rubber gasket. The slide was filled with 2mL of fresh 0.85% NaCl. Confocal microscopy with a 488nm wavelength filter was then used to image the electrode biofilm (Figure 15 A). The electrode was then cleaned using a routine polishing method with 0.05µm alumina slurry and washed in deionized (DI) water for 20 minutes. The electrode was then immobilized in a clean glass coverslip and imaged again with identical microscope settings (Figure 15 B). Finally, an aggressive cleaning was performed, and the electrode was again washed, immobilized on a clean glass slip, and imaged (Figure 15 C). The images confirm that routine cleaning is insufficient for removing biofilms from the electrode surface, and that aggressive cleaning is required at the expense of electrode longevity.

59

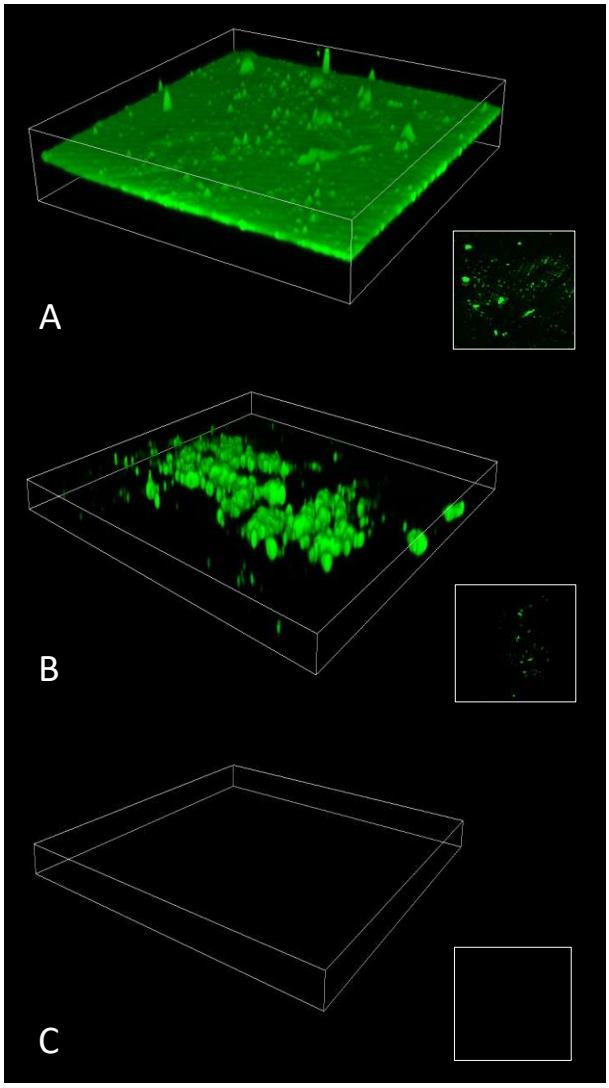

Figure 15: Confocal microscopy of glassy carbon electrodes with a 48 hour biofilm (A), after a standard electrode cleaning with 0.05 µm alumina slurry (B) and after thorough cleaning with 0.05 µm, 0.3 µm, and 1 µm alumina slurries (C).

3.3 Reactor design for BES

3.3.1 Common issues in BES reactor design

There are many unique considerations in BES design that are vital for obtaining meaningful data from experiments. Improper reactor design can lead to unintended variables caused by background electrochemical phenomena. Potentiostatic control, isolation of the

60

working electrode, and electrode and assembly materials must be evaluated. Controlling pH in BES presents additional challenges.

3.3.2 Potentiostatic control and isolation of working electrode

Mathew et al applied potentials ranging from 0 to 15V to fermentations of *S. cerevisiae* in a single-chamber reactor using a DC power supply [105]. Several common problems are exemplified by this work. First, using a two-electrode configuration and a DC power supply does not provide potentiostatic control. This means that the actual potential at the working electrode is unknown and can shift throughout the course of the experiment. Further, even the smallest applied voltages investigated in this study (3V and 10V) are large enough to result in significant background electrochemistry including rapid electrolysis of water. Finally, the use of a single-chamber reactor means that the effects of reactions occurring at the anode and cathode cannot be isolated.

Shin et al. performed electrically enhanced fermentations of *C. thermocellum* and *S. cerevisiae* in a dual-chamber reactor with a cation-selective membrane separating anode and cathode compartments. However, a two-electrode configuration was again used, and large voltages (-5.0V) were applied. Separation of the anode and cathode offers the benefit of isolating the effect of the electrode of interest, but without potentiostatic control, the actual applied potential at this electrode cannot be controlled. Additionally, at such large applied voltages, electrolysis is again likely. When electrolysis occurs in a dual-chamber reactor, hydroxide ions are produced at the cathode, and protons are reduced to hydrogen gas, thus driving the pH to increase significantly[106].

61

To study the effect of an applied electrochemical potential on a fermentation, the working electrode must be isolated from the counter electrode, which can swing to large potentials to generate current needed to drive reactions at the working electrode. Potentiostatic control using a three-electrode system is also necessary to control the working electrode at a known potential and avoid background electrochemistry such as water electrolysis.

3.3.3. Electrode and Electrode Assembly Materials

Another common pitfall in BES reactor design lies in the selection of electrode and wiring materials. Carbon and graphite felts are common materials for working electrodes in BES as carbon is relatively electrochemically inert and the high surface area and fibrous material encourage microbe-electrode interaction. However, little consideration is given to the materials used to attach working electrodes to external wiring. Stainless steel alligator clips are frequently used to connect working electrodes, but materials such as steel, copper, and alloys in solder will corrode quickly in BES.

Anaerobic corrosion is an electrochemical process that can occur on steel and other alloys that are submerged in an electrolyte by both abiotic and biotic mechanisms and results in production of hydrogen and soluble iron compounds[133]. The anaerobic corrosion process is accelerated by applied potentials and can catalyzed by sulfur reducing bacteria that are present in some inocula. The iron and hydrogen released in this process can the directly influence metabolic processes[134–136]. While iron and hydrogen supplementation may be beneficial to bioprocesses, the existence of corrosion in biased reactors makes it impossible to determine the

62

effect of direct electron transfer. Corrosion at the working electrode not only influences metabolic processes, but it also prevents the acquisition of meaningful electrochemical data.

To avoid corrosion, steel and other alloys should not be used in the working electrode, but metals used must also be electrochemically inert. For example, while platinum is an excellent material for preventing corrosion, it catalyzes hydrogen evolution through electrolysis and therefore is not suitable for the study of direct electron transfer. Gold and titanium

In contrast, materials used in the counter electrode assembly should be electrochemically reactive. Platinum and platinized metals make ideal counter electrode materials due to their reduced overpotential for water electrolysis, which is necessary to produce the necessary current to drive reactions at the working electrode.

3.3.4 Modes of pH Control for BES

pH is an important operating parameter for all biological processes. pH control becomes even more important in the context of BES, where it can influence metabolic as well as electrochemical processes. It is vital to control pH in BES research to understand the effects of applied potential under specific operating conditions. However, controlling pH in BES presents a challenge, as traditional pH probes cannot be used directly in electrochemical systems. Electrochemical pH probes function by measuring the electrical potential of a solution, thus inserting a pH electrode into an applied electric field results in inaccurate pH readings.

There are several possible solutions to enable pH control in BES. Here, we will explore 3 modes of pH control: A continuous cycling reactor system, pulsed chronoamperometry with intermittent pH monitoring, and manual adjustment.

63

A reactor system was developed for the application of electro-enhanced anaerobic digestion with continuous, automated pH control. In this system (Figure 16), the digestion took place in the working electrode compartment (A) of a dual-chamber (H-cell) reactor, and two peristaltic pumps were used to continuously circulate the sludge through an external pH adjustment chamber (C). To maintain liquid levels in chamber A, the pump for effluent had a fixed speed of 60 rpm (P_{60} in the schematic), with the outlet fixed at the liquid level, while the influent pump had a fixed speed of 20 rpm (P_{20}). Due to the pressure differential created by the peristaltic pumps, an additional segment of tubing was used to connect chamber A and chamber C. The pH adjustment chamber contained a pH probe connected to an Arduino pH controller (Figure 17A). The controller measured the pH at specified time increments (ranging from 1 minute to 1 hour) and powered on a dosing pump to dispense NaOH into the pH adjustment chamber when the measured pH dropped below a specified threshold. The volume of NaOH injected could be controlled by adjusting the dispensing time and voltage supply. This reactor was operated with four separate units (Figure 17 B).

64

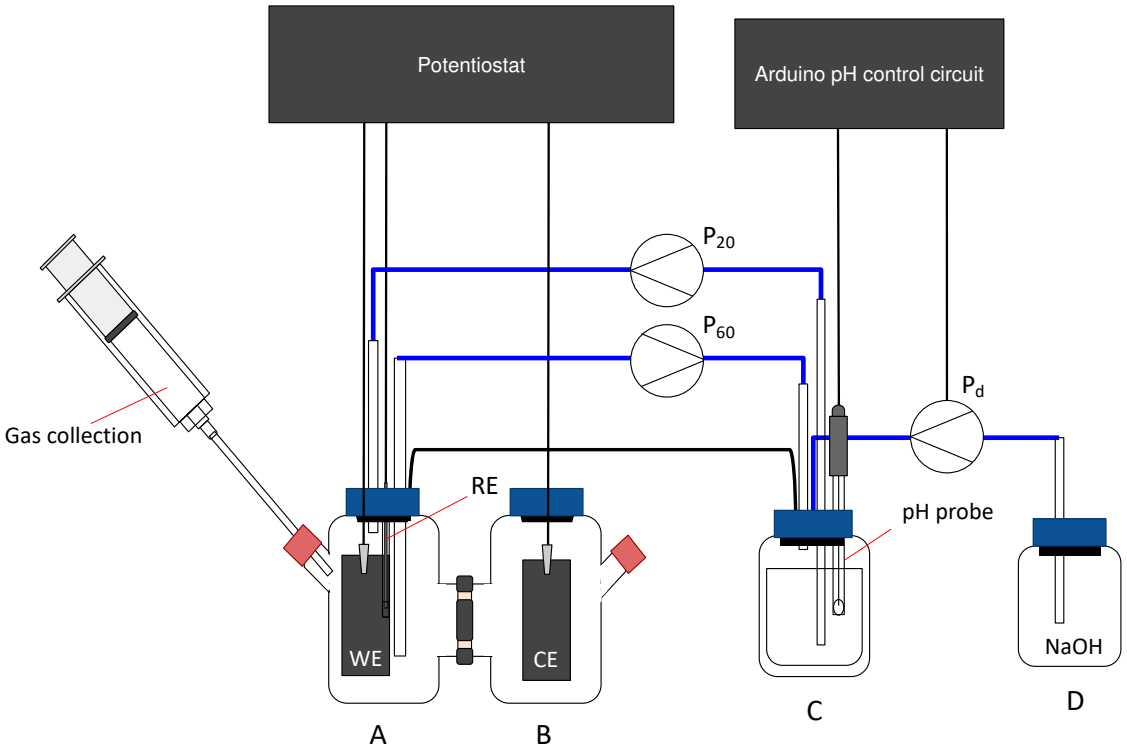

Figure 16: Schematic of one unit of the continuous cycling reactor system. A: working electrode compartment containing the anaerobic digestion, carbon felt working electrode, and Ag/AgCl reference electrode. B: Counter electrode compartment containing 200mM KCl and a platinized titanium mesh counter electrode. C: the pH adjustment chamber containing a pH probe and continuously circulated digestion from A. D: 2N NaOH.

65

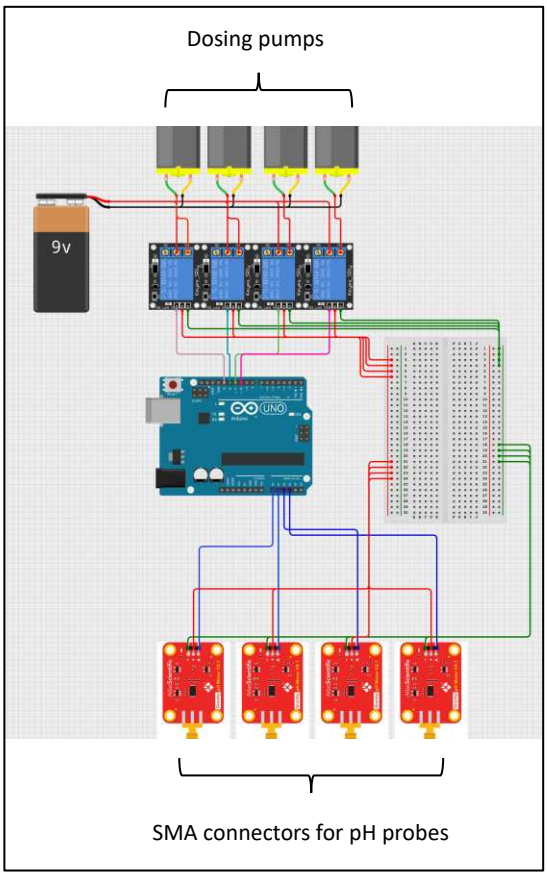

Figure 17: A: Circuit diagram of the Arduino pH controller for four reactor units.

66

Figure 18: Photo of the continuous cycling reactor system with four units.

The continuous cycling reactor system enabled accurate pH control with a threshold of ±0.1 of the desired pH at all times. The control could easily be adapted by changing parameters such as sampling and dosing frequency and dosing volume. Additional pumps for dispensing acid could also be added to the system as needed. However, this system presented several limitations. Due to the complexity of the system, set up and maintenance is laborious. Additionally, the many pumps, valves, and connectors involved increase the risk of leaks and blockages, and wearing of tubing segments in peristaltic pumps can cause small tears that result in aeration of reactors. Results from this system were unreliable, and the growth of mold on the gas-liquid interface suggested that aeration was significant. This system could be improved with alternative tubing and connector materials.

67

A second option for automated pH control involves pulsed chronoamperometry combined with intermittent pH monitoring. This option provides the benefit of a simpler reactor design and significantly decreased risk of aeration at the expense of more complex controller design, potentiostat capabilities, and unwanted effects on electrochemical data.

In this design, chronoamperometry must be switched off periodically so that pH can be read by a probe directly in the H-cell working electrode chamber. The pH is then adjusted by the Arduino pH controller. It may be necessary for multiple readings and injections to occur during the off period. Chronoamperometry then resumes at the specified potential. A theoretical waveform for the applied potential is shown in figure 18. However, while OCP is pictured as a constant potential here, OCP is actually variable over the course of an experiment. Therefore, traditional pulsed chronoamperometry cannot be used. If the potentiostat does not have the capability to perform pulsed chronoamperometry with steps at OCP, a switch would be required to stop the flow of current to the reactor. This would require the use of an additional circuit and increasd complexity of the controller. If the potentiostat does have this capability, the timing of the pulses must correspond exactly with the timing of the controller circuit. Finally, the frequent pulses would affect electrochemical data significantly and would prevent reliable observation of current generation or consumption in the reactor.

68

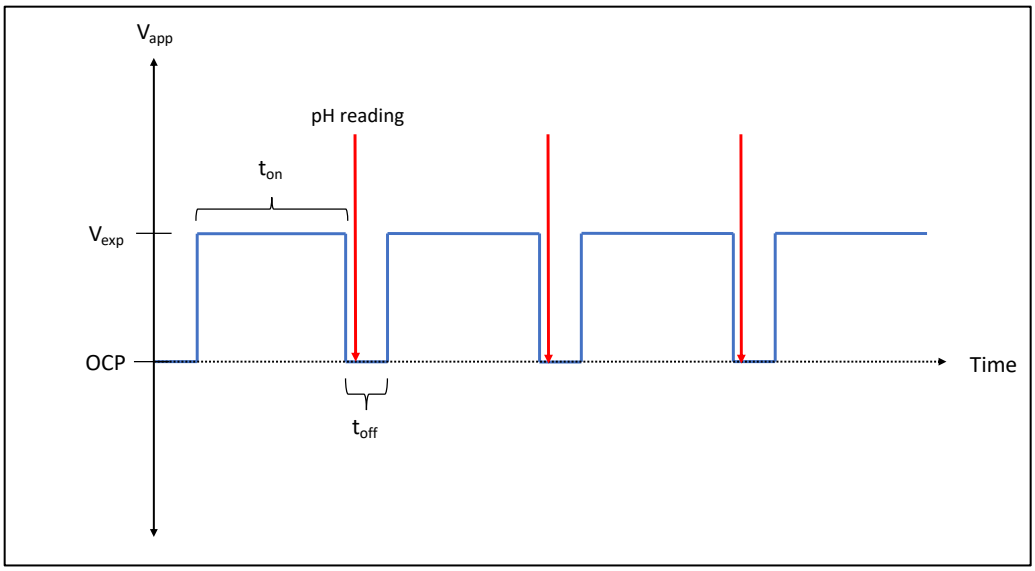

Figure 19: pulsed chronoamperometry waveform for intermittent pH monitoring and control, where V_{exp} indicates the applied bias for a given experiment and t_{on} and t_{off} represent the steps for applied potential and OCP, respectively.

A third option for pH control in BES is manual adjustment. Manual adjustment provides the least accurate pH control, but enables continuous (daily) chronoamperometry and simple reactor design with low risk for aeration and other malfunctions. For manual adjustment, a pH probe can be used when CA is stopped once daily for sampling. pH paper can also be used in place of a pH probe, or for more frequent measurements without interruption of CA. Figure 20 compares pH control in manually adjusted and continuous cycling reactors.

69

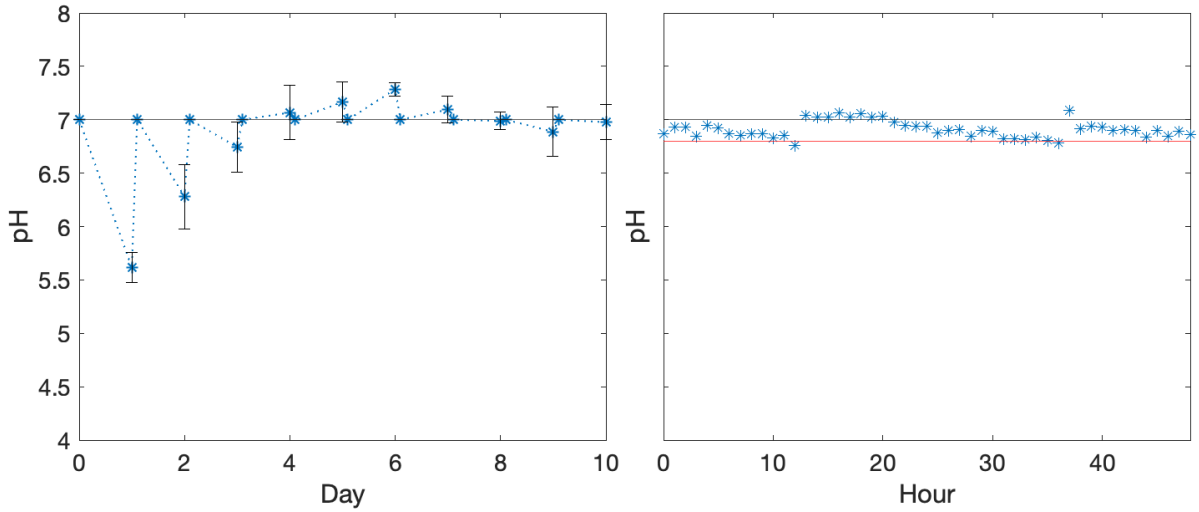

Figure 20: pH control in manual adjustment (left) and continuous cycling (right) reactors. A period of 10 days is shown for an experiment using once daily manual adjustments, and a period of 50 hours is shown for the continuous cycling system to show fluctuations.

3.4 Conclusions and Limitations

BES are promising technologies for sustainable production of fuels and chemicals, but there are many challenges in the development of successful electro-enhanced bioprocesses technologies, and much remains unknown about the mechanisms involved in BES, especially in cathodic systems. We have identified several of the challenges commonly faced in BES research and proposed solutions for improved methods in electrochemical analysis and reactor design for BES. Even with these proposed methods, the study of microbe-electrode interactions remains extremely challenging and there are limitations to the implementation of these methods.

It is difficult to propose standardized methods for evaluating EET across species given the diversity of microbial metabolism and the major knowledge gaps that still exist for cathodic electron transfer. Because EET may be dependent on a number of factors for any given species, including residual dissolved oxygen, iron availability, substrate, and pH, one must be cautious to not make over-simplified conclusions about the electroactivity of a given organism. However, using careful consideration of appropriate backgrounds and controls, and by implementing

70

adequate electrode cleaning techniques, electroanalytical methods can help to elucidate these mechanisms and conditions affecting them. Better understanding of EET mechanisms is necessary for the development of elecro-enhanced bioprocesses.

71

CHAPTER 4: ELECTRO-FERMENTATION OF *CLOSTRIDIUM PASTEURIANUM*

4.1 Introduction

Our current energy infrastructure depends on energy-dense carbon compounds, which are primarily derived from nonrenewable fossil fuels. Low-carbon bioprocesses have gained attention as sustainable alternatives for producing industrially valuable fuels and chemicals. While organic acids and alcohols can be produced microbially through fermentation, the large-scale production of many valuable metabolites is limited by low yields and high costs. Frequently, the metabolites of greatest interest are those that contain the most carbon molecules, such as higher alcohols and C4+ acids. These larger molecules contain more energy in covalently bonded carbon, making them more suitable for use as fuels and fuel precursors.

In fermentation, electrons enter cellular metabolism through the carbon substrate, and NAD^+ is reduced to NADH in glycolysis. NAD^+ is then regenerated as NADH donates electrons in other metabolic pathways, resulting in the production of reduced metabolites. The synthesis of higher alcohols and longer chain acids require more electrons through NAD regeneration than smaller organic acids like acetate. Because fermentation is controlled by redox balance, yields of more reduced metabolites are limited by redox constraints.

Electro-fermentation is a novel bioprocess technology that may provide a sustainable, low-cost, low-carbon process for microbial production of high-value, reduced metabolites by overcoming this redox limitation. In electro-fermentation, electrons from renewable energy can be delivered directly to microorganisms to alter the intracellular NADH/NAD+ balance, inducing a metabolic shift that favors NADH-consuming pathways.

72

Electro-fermentation, a is a cathodic process, requiring an electron transport mechanism for extracellular electron transfer (EET) to accept electrons from a cathode surface and shuttle them into the cell. The ability of a microbe to transfer electrons to an anode or to accept electrons from a cathode is referred to as electroactivity. While the mechanisms of 73nodic EET for known electroactive species, such as species of the genera *Shewanella* and *Geobacter,* have been studied extensively, little is known about electron transfer and utilization in cathodic EET.

Clostridium pasteurianum, a gram-positive, spore forming bacterium*,* is a natural producer of butanol, a four-carbon alcohol with high industrial value and potential as a biofuel component[137,138]. Previous studies have provided evidence that *C. pasteurianum* may be capable of direct electron consumption from a cathode[107,108]. Choi et al. used cyclic voltammetry (CV) to observe possible electroactive behavior in *C. pasteurianum,* and multiple studies have shown that fermentations of *C. pasteurianum* in a cathodic cell gave increased yields of butanol with an applied potential[83,108]. These results provide evidence that *C. pasteurianum* may be capable of direct cathodic electron transfer, and that electro-fermentation could be an effective process for biobutanol production.

In this work, we investigate electro-fermentation of *C. pasteuranium* under carefully controlled conditions in two types of growth medium. Our results indicate that redox control of *C. pasteurianum* fermentations using applied electrochemical potentials may be possible, but additional studies are required to investigate *C. pasteurianum* electroactivity.

4.2 Materials and Methods

4.2.1 Media and Culture Conditions

Clostridium pasteurianum DSM 525 was purchased from DSMZ as a freeze-dried pellet. The pellet was revived in an anaerobic chamber using 54b medium as specified by DSMZ. Glycerol stocks (2mL) were made from the initial revival culture and were stored in anaerobic, sealed serum bottles at -80C. For each experiment 1mL of glycerol stock was used to inoculate a 100mL overnight culture, which was incubated for approximately 15 hours for use as an inoculum in subsequent experiments.

Reinforced clostridial medium (RCM) was prepared with 10g peptone, 11.0g glucose, 13.0 g yeast extract, 5.0g NaCl, 1.0g soluble starch, 2.72g sodium acetate trihydrate, and 0.5g L-cysteine HCl in 1L deionized water. The pH was adjusted to 6.8, and the medium was autoclaved and cooled under a stream of nitrogen.

To prepare P2 medium, 18 g of glucose was dissolved in 790mL deionized water (solution 1). Three 100mL solutions were prepared with 0.5g K_2HPO_4, 0.5g KH_2PO_4, and 2.2g CH_3COONH_4 (solution 2), 2.0g $MgSO_4 \bullet 7H_2O$, 0.1g $MnSO_4 \bullet H_2O$, 0.1g NaCl, 0.1g $FeSO_4 \bullet 7H_2O$ (solution3), and 100mg p-aminobenzoic acid, 100mg thiamine, and 1mg biotin (solution 4). Solutions 1 and 2 were autoclaved separately and mixed after cooling under a stream of nitrogen. Solutions 3 and 4 were filter sterilized and added (10mL and 1mL, respectively) to the cooled medium. The pH was adjusted to 6.8 using 5mM NaOH, and 100mL of 1M MES stock solution was added.

4.2.2 Bioelectrochemical System

The bioelectrochemical system composed of an H-cell reactor with two compartments separated by a Nafion 117 cation exchange membrane. Nafion 117 was cut to the appropriate size, then stored in sterilized DI water. Carbon felt working electrodes ($13cm^2$) were pretreated

74

in 10% isopropanol and stored in DI water. Both chambers of the H-cell were sealed using rubber stoppers with the appropriate airtight fittings. On the working electrode side, titanium wire sealed in the stopper was used to attach working electrodes. Before autoclaving, pretreated working electrodes were woven onto the titanium wire. Platinized titanium mesh counter electrodes were attached to copper wire with alligator clips. H-cells were then filled with DI water and autoclaved. Growth medium was prepared and autoclaved separately as described. The Ag/AgCl reference electrodes were sterilized with UV radiation and 60% isopropanol. After autoclaving and electrode sterilization, H-cells were transferred to a biosafety cabinet, where the working electrode and counter electrode chambers were emptied, then filled with growth medium and 200mM NaCl, respectively. Sterilized reference electrodes were inserted into airtight fittings in working electrode chamber stoppers. Working electrode chambers were then purged for at least 2 hours with ultra-high purity nitrogen gas that passed through a 0.2-micron filter. The reactor was then sealed, and a 3L tedlar gas bag was attached to the working electrode compartment side port. H-cells were incubated at 37°C and agitated with magnetic stir bars at 200rpm. The electrodes were then connected to a potentiostat (both a CHI 1000 multichannel potentiostat and a Pine WaveDriver single channel potentiostat were used in these experiments depending on instrument availability).

4.2.3 Electro-fermentations

After the H-cell was assembled, purged, sealed, and placed in the incubator, background cyclic voltammograms were obtained. All CV scans were performed at a scan rate of 2mV/s unless otherwise specified. The working electrode compartment was then inoculated with 2.5mL overnight culture, and an inital (T_0) scan was taken. The specified electrochemical potential was

75

applied to biased reactors using chronoamperometry (CA). For unbiased controls, the reactor wire leads were not connected to the instrument except during CV scans.

pH was adjusted manually using 1N NaOH twice during exponential growth phase, then once daily. pH was measured using narrow-range pH paper, and NaOH was added using a sterile syringe and needle, which was inserted through the rubber stopper.

At each experimental time point, 1.5mL samples were obtained. OD_{600} was measured, then samples were centrifuged to separate the cell pellet and supernatant, which were stored separately at -80C for later analysis. At select time points, chronoamperometry was paused to perform CV. At the end of each experiment, the working electrode was removed and rinsed gently with phosphate-buffered saline (PBS) to remove planktonic cells and supernatant from the fibers. The electrode was then placed in a falcon tube containing 30mL PBS and vortexed for 20 minutes. The carbon felt was then removed and discarded, and the tube was centrifuged to pellet the removed biofilm.

In some cases, further electrochemical tests were performed before harvesting electrode biofilms. H-cells were moved to an anaerobic chamber, where the broth was drained from the WE chamber, centrifuged, and filtered for further electrochemical analysis. The electrode was then gently rinsed with PBS, and the WE compartment was refilled with PBS. The H-cell was then returned to the incubator to perform additional CV scans using the bioelectrode in electrolyte. PBS was then replaced with fresh, anaerobic growth medium inside the anaerobic chamber, and scans were repeated.

4.2.4 Analytical Methods

Supernatant samples were analyzed using HPLC. HPLC analysis was performed on a 300mm x 7.8mm Aminex HPX-87H column (Bio-Rad Laboratories GmbH). The mobile phase was 2.5mM sulfuric acid and the flow rate was 0.6mL/min. The injection volume was 20μL and oven temperature was controlled at 80°C with a pressure of 36 bar. Standard curves were generated using mixed standards at concentrations of 1, 5, 25, 50, and 100mM of glucose, lactic acid, acetic acid, butyric acid, ethanol, and butanol. Triplicate injections were performed for each sample.

4.2.5 Experimental design

Due to limitations of laboratory equipment availability, an adequate number of control and biased fermentations could not always be performed simultaneously. However, it was observed that high reproducibility could be achieved in sequential experiments. To reduce variability, the same batch of growth medium and the same glycerol stock was used for the controls corresponding to each reported treatment. Six control and six biased replicates were performed for RCM experiments, but no replicates have been performed for P2 medium experiments.

4.3 Results

4.3.1 Extracellular Electron Transfer

Chronoamperometry was used to maintain applied potentials and monitor current generation and consumption during electro-fermentations. Abiotic CA controls were performed on sterile medium to discern whether measured currents were produced by background electrochemistry or microbe-electrode interactions. Slow scan rate (2mV/s) CV was performed

77

on biased and unbiased control H-cells each day to monitor electron transfer behavior of biofilms.

4.3.1.1 P2 Medium

Figure 26 shows chronoamperograms for electro-fermentation of *C. pasteurianum* in P2 medium at -200mV vs. Ag/AgCl with an abiotic control of sterile P2 medium at -200mV vs. Ag/AgCl. In the abiotic reactor, current is consumed due to background electrochemical reactions, whereas very small (maximum ~4μA) positive current is observed in the *C. pasteurianum* electro-fermentation.

Background reactions can also be observed in cyclic voltammograms of P2 medium at time zero of the electro-fermentation (Figure 21). After 24 hours of growth, less redox behavior is observed. While the electron transfer behavior changes over the course of the electro-fermentation, there are no significant differences observed between the biased and control reactors.

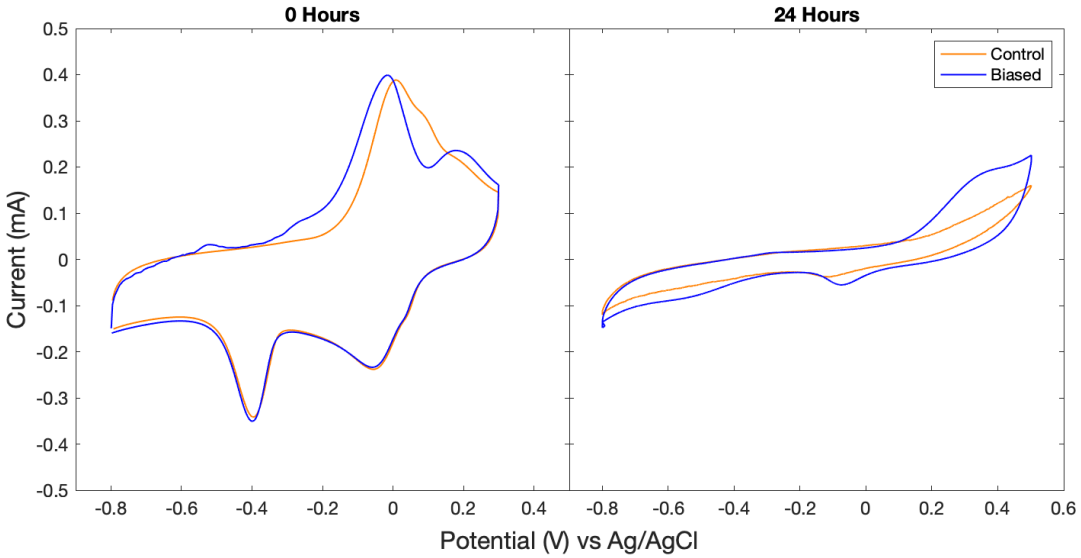

78

Figure 21: Cyclic voltammograms (2mV/s) of *C. pasteurianum* fermentations in biased (-200mV vs. Ag/AgCl) and control reactors at 0 and 24 hours of growth in P2 medium.

4.3.1.2 Reinforced Clostridial Medium

Figure 22 shows chronoamperograms for electro-fermentation of *C. pasteurianum* in RCM at -600mV and -700mV vs. Ag/AgCl with an abiotic control of sterile RCM at -600mV vs. Ag/AgCl. In all three cases a negative current is observed. In the biotic reactors at both -600 mV and -750 mV vs. Ag/AgCl, the magnitude of this cathodic current quickly drops within the first 20 hours after inoculation. In the abiotic control, a decrease in current magnitude is also observed, but at a significantly slower rate.

Cyclic voltammograms of RCM show two redox reactions centered at approximately -300 and -400mV vs. Ag/AgCl. Development of a biofilm does not appear to change electron transfer behavior in control reactors (Figures 23 and 24) or with an applied potential of -600mV vs. Ag/AgCl (Figure 23). However, when a potential of -750mV vs. Ag/AgCl was applied, electron transfer behavior changed significantly within 24 hours (Figure 24).

79

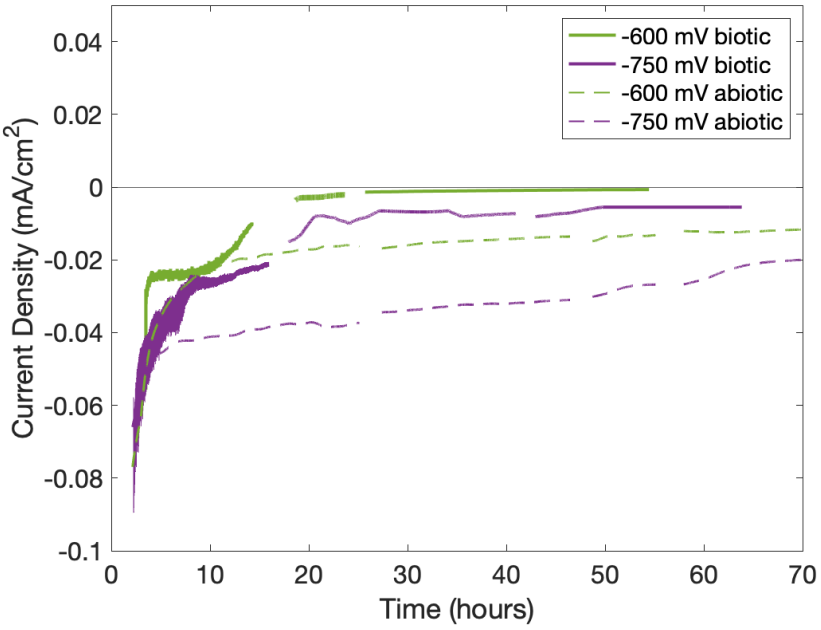

Figure 22: Chronoamperograms of *C. pasteurianum* fermentations in RCM at -750 mV and -600 mV vs. Ag/AgCl and abiotic controls at -600 mV and -750 mV vs. Ag/AgCl.

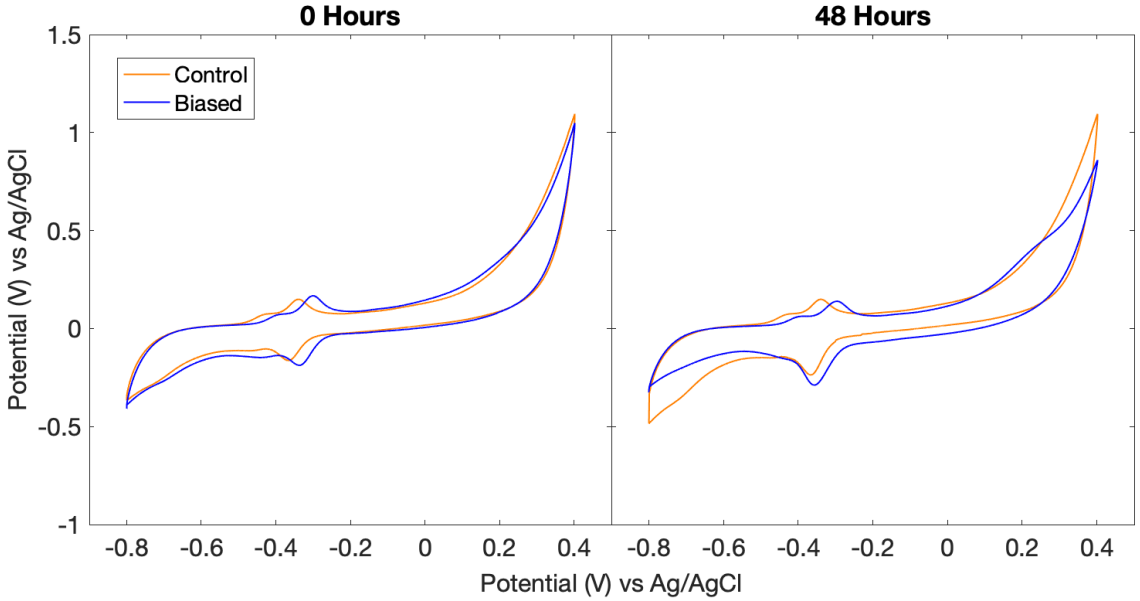

Figure 23: Cyclic voltammograms (2mV/s) of *C. pasteurianum* fermentations in biased (-600mV vs. Ag/AgCl) and control reactors at 0 and 48 hours of growth in RCM. Note that CV was also performed at 24 and 72 hours, but voltammograms showed the same behavior at all time points.

80

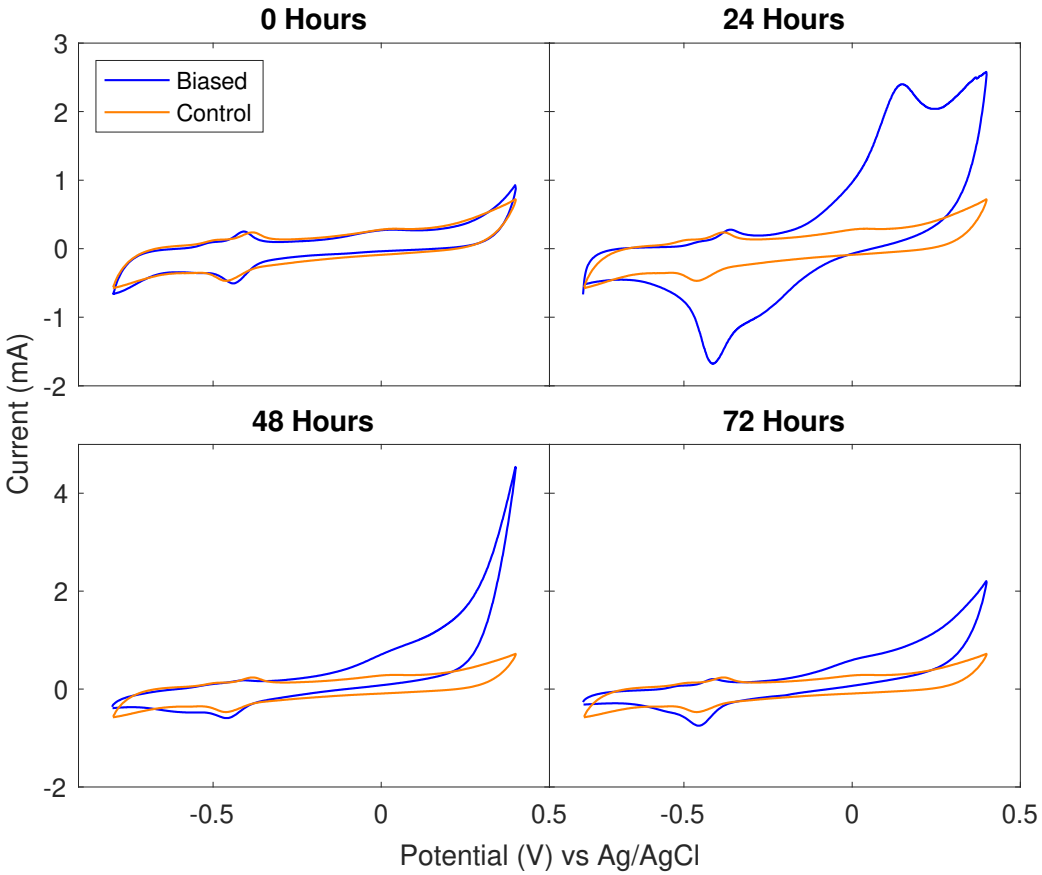

Figure 24: Cyclic voltammograms (2mV/s) of *C. pasteurianum* fermentations in biased (-750mV vs. Ag/AgCl) and control reactors at 0, 24, 48, and 72 hours of growth.

4.3.2 Growth and Metabolism

4.3.2.1 P2 medium

In P2 medium, turbid cell growth was observed after 12-15 lag phase, with exponential growth ending between 24 and 28 hours. Maximum optical densities reached 4.51 and 4.31 in biased and control reactors, respectively. Applied potential did not appear to influence planktonic cell growth (Figure 25). Applied potential also showed no influence on metabolite profiles (Figure 26).

81

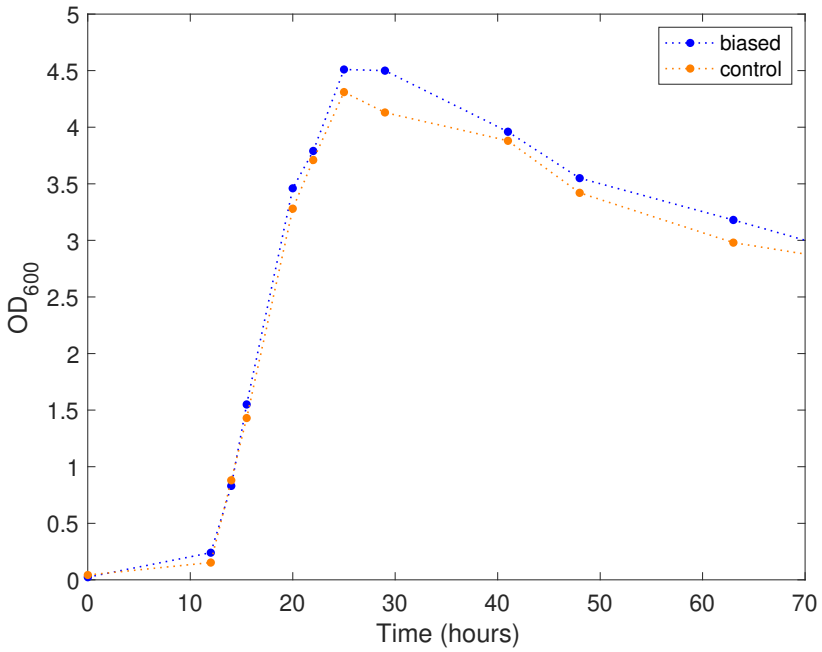

Figure 25: Growth curves for biased (-200 mV vs. Ag/AgCl) and unbiased control fermentations of *C. pasteurianum* in P2 medium.

82

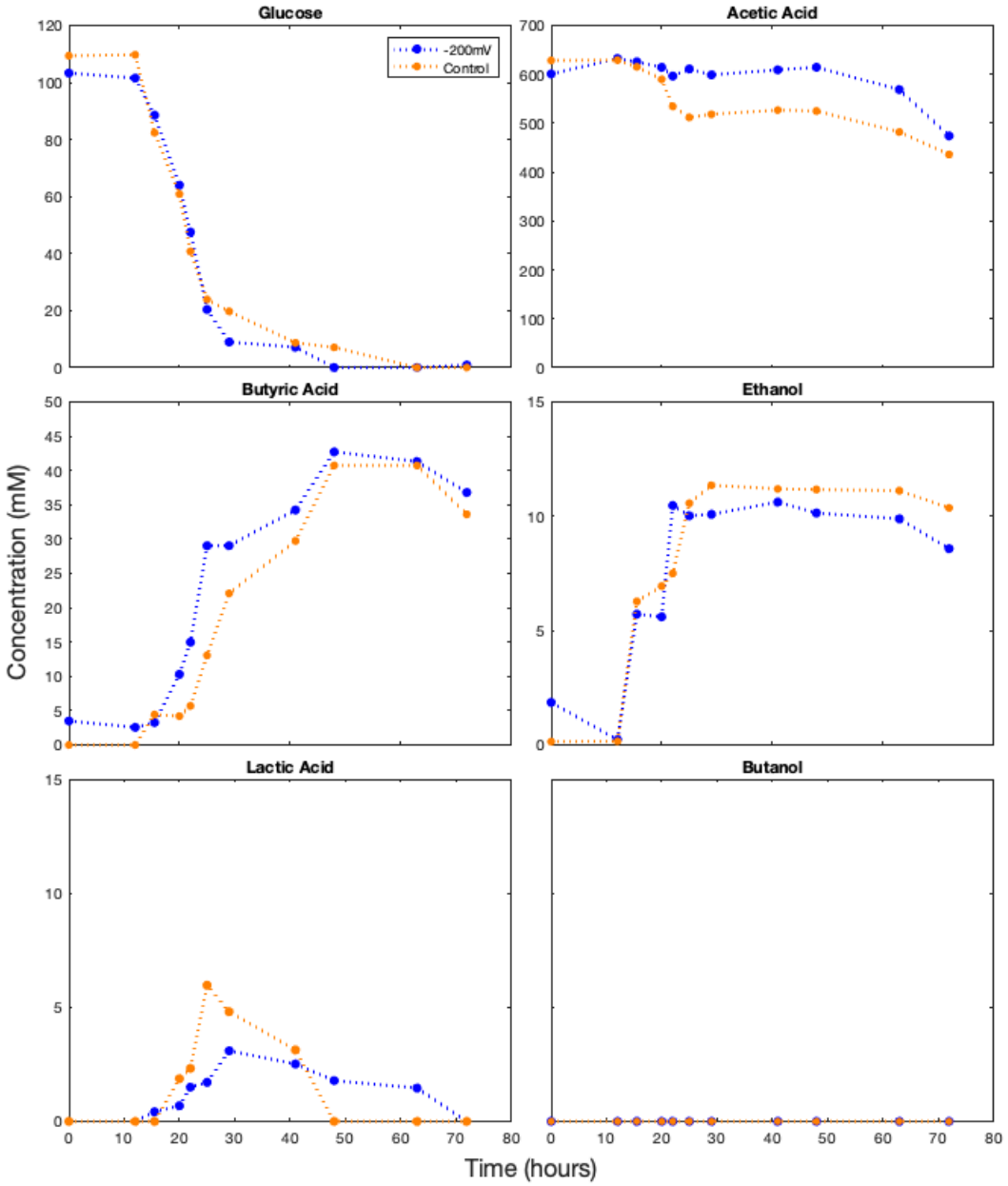

Figure 26: Metabolite profiles for biased (-200mV vs. Ag/AgCl) and unbiased control C. pasteurianum fermentations of P2 medium.

4.3.2.2 Reinforced Clostridial Medium

In reinforced clostridial medium, turbid cell growth is consistently observed after a ten-hour lag phase, with exponential growth ending at approximately 22 hours. Maximum optical

83

densities reached approximately 2.0 -2.5. A decrease in OD was observed shortly after exponential growth ended at approximately 24 hours, when glucose was depleted (Figures 27 and 28). An applied potential of -600mV vs. Ag/AgCl did not appear to affect planktonic cell growth (Figure 27), while planktonic cell growth was slightly lower in -750 mV biased reactors compared to their respective controls, reaching a 17% lower average maxiumum OD.

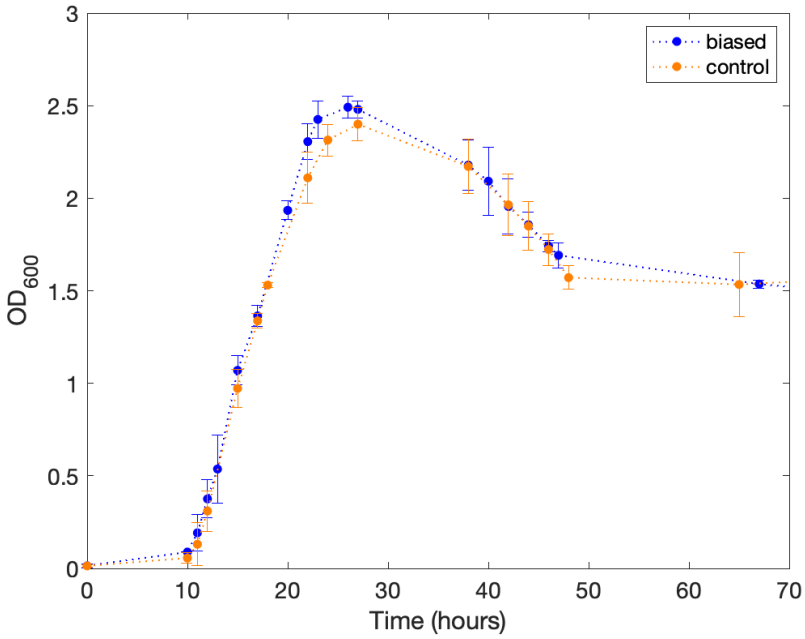

Figure 27: Growth of planktonic C. pasteurianum in bioelectrochemical system with an applied bias of -600mV vs. Ag/AgCl (blue) and no applied bias (orange).

84

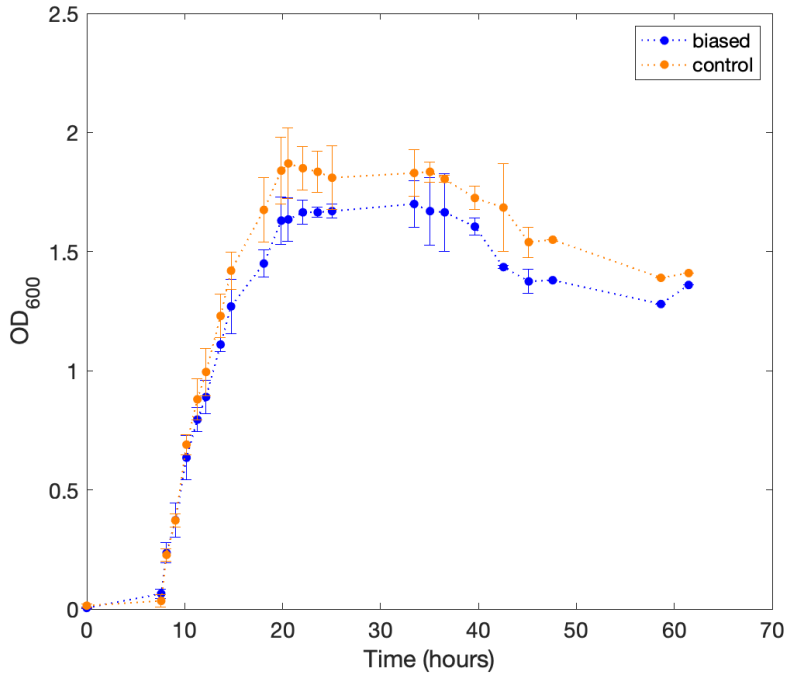

Figure 28: Growth of planktonic C. pasteurianum in bioelectrochemical system with an applied bias of -750mV vs. Ag/AgCl

Metabolic shifts were observed under applied potentials of -600mV and -750 mV vs. Ag/AgCl (Figures 29 and 30). At -600 mV, Butyric acid production increased by 38%, while acetic acid production decreased by 7.2%. Lactic acid reached a maximum concentration of 4.3 mM in both biased and control reactors, this lactic acid was then consumed less rapidly in biased reactors. Ethanol concentrations also reached similar levels in biased and control reactors. At -750 mV, higher butyric acid concentrations were again observed in biased reactors, but with a much smaller increase of only 7.5%. This increase was coupled with a 25% decrease in ethanol production and no lactic acid production. Butanol was not produced in any biased or control reactors.

85

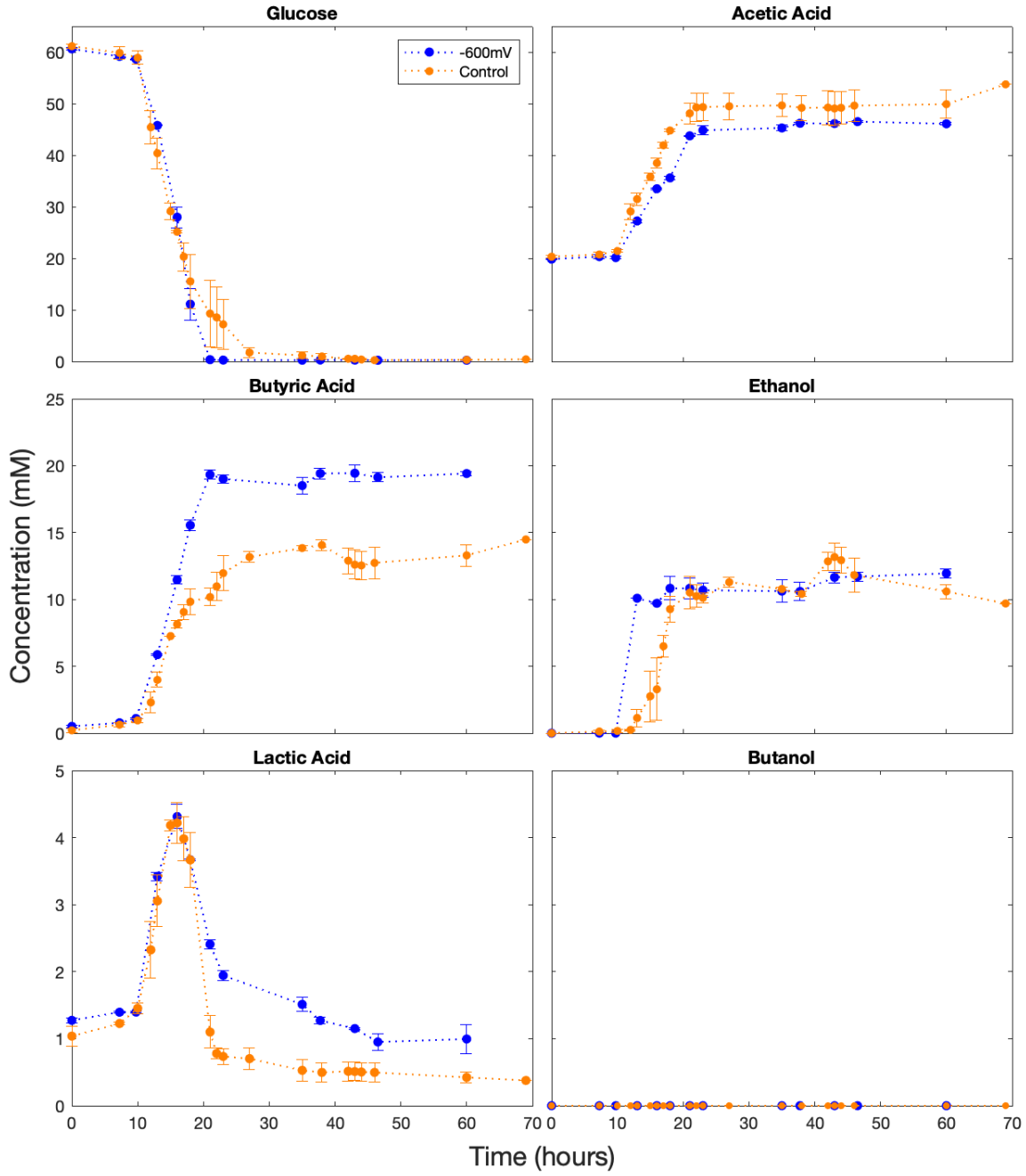

Figure 29: Metabolite profiles for biased (-600mV vs. Ag/AgCl) and unbiased control C. pasteurianum fermentations of RCM.

86

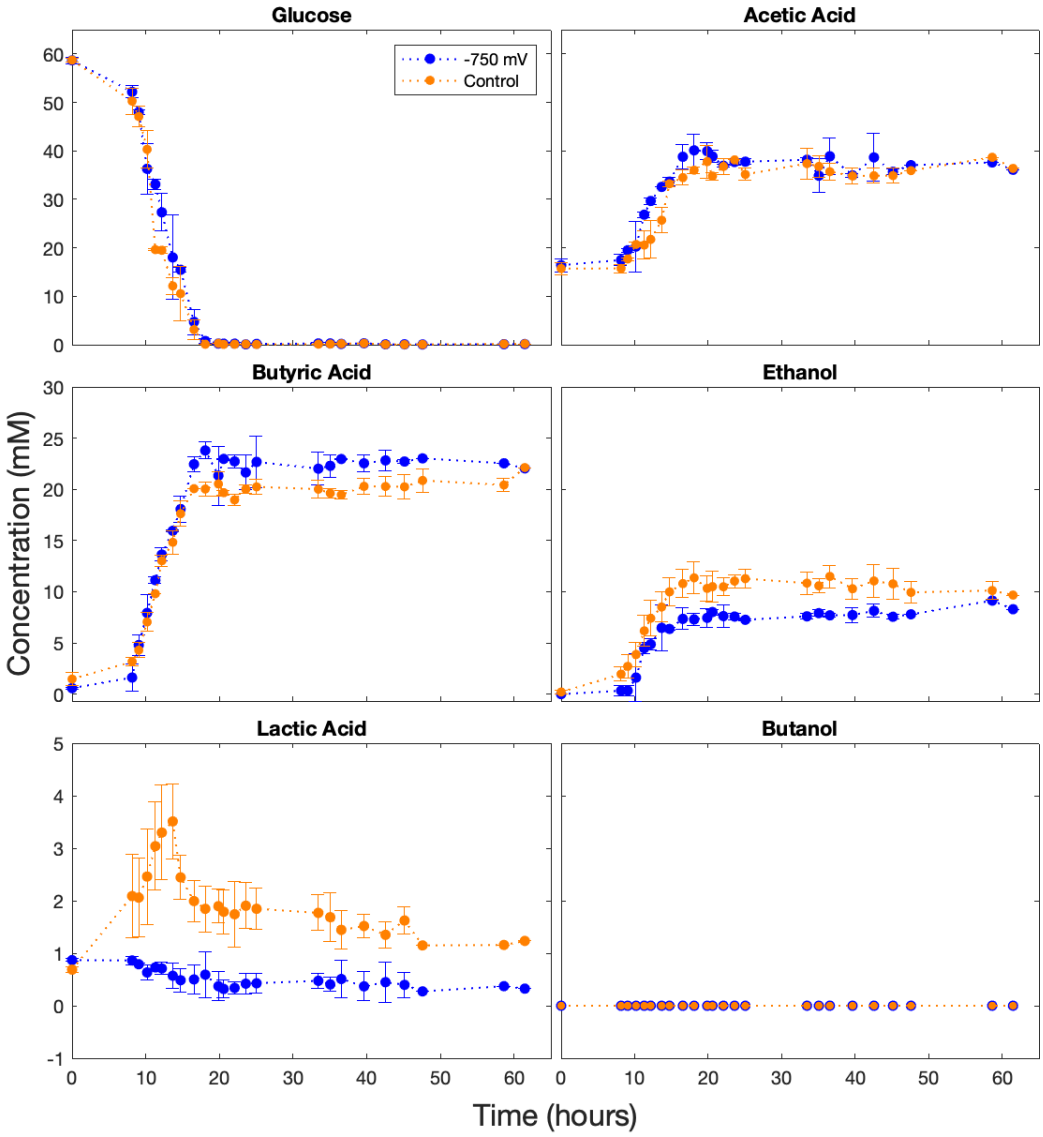

Figure 30: Metabolite profiles for biased (-750mV vs. Ag/AgCl) and unbiased control C. pasteurianum fermentations of RCM.

4.4 Discussion

4.4.1 Oxidation Reduction Potential in Fermentation

The oxidation-reduction potential (ORP) of a solution is a measurement of overall electron transfer in the solution. It is an open circuit potential (OCP), in that it represents the

87

potential measured between an electrode and a reference, with no external voltage applied. ORP is known to play an important role fermentation, as it corresponds to the net balance of reducing equivalents involved in metabolic processes[139]. ORP of unbiased controls was monitored by measuring the OCP between the carbon felt biocathode and Ag/AgCl reference electrode. Figure 31 shows a representative measured ORP of an unbiased control. The ORP of unbiased fermentations begin between -100 and +100 mV vs. Ag/AgCl due to residual dissolved oxygen and a lack of metabolic activity. However, within a few hours, the ORP decreases to approximately -300 mV vs. Ag/AgCl and remains constant for the remainder of the lag phase. When exponential growth begins at approximately 8 hours, the ORP further decreases to -500 mV vs. Ag/AgCl. Applied potentials below OCP will promote reduction, while applied potentials that are more positive promote oxidation. Based on representative ORP measurements, applied potentials must be lower than -500 mV vs. Ag/AgCl to promote reduction during the entire duration of a fermentation. Previous studies have reported metabolic shifts at applied potentials of -200 mV vs. Ag/AgCl, which were attributed to cathodic DET. However, it is unlikely that the working electrode was functioning as a cathode or that an applied potential of -200 mV vs. Ag/AgCl would induce cathodic DET. Redox control in the absence of DET, whether reductive or oxidative, may induce metabolic shifts regardless of microbial electroactivity, as it may influence the transmembrane electrochemical ion gradients that control metabolic redox reactions[140].

88

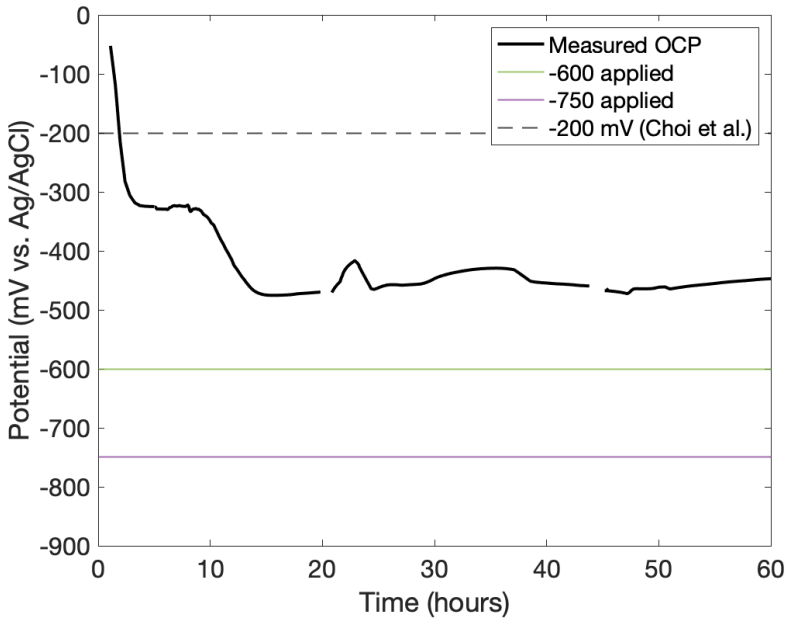

Figure 31: Oxidation-reduction potential (ORP) of an unbiased control reactor measured as the open circuit potential (OCP) between the biocathode and reference electrode

4.4.2 Electroactivity is not observed in P2 medium at oxidative potentials

Previous studies have reported electroactive behavior in CV of *C. pasteuriaunum* grown in P2 medium. However, our results do not provide evidence of C. pasteurianum electroactivity under the conditions studied. Choi et al. reported current consumption of up to 1.5 mA for C. pasteurianum grown in P2 medium with an applied potential of approximately -200mV vs. Ag/AgCl, but our results show that no current is consumed by *C. pasteurianum* biofilms grown under the same conditions. Furthermore, because the ORP in fermentation quickly drops to below -500mV vs. Ag/AgCl, an applied potential of -200mV in an active fermentation would promote oxidation rather than the reduction claimed by the authors. We observed significant background electrochemistry in P2 medium, and with an applied potential of -200mV vs. Ag/AgCl, currents of up to -0.24 mA were measured in the abiotic control. However, in reactors inoculated with *C. pasteurianum*, the current quickly fell to +4μA, indicating that the working

89

electrode was acting as an anode and that current was not being consumed nor produced by *C. pasteurianum.* Cyclic voltammograms of P2 medium and *C. pasteurianum* biofilms in P2 medium showed that redox-active species were present in the sterile medium. The activity of these redox reactions decreases over the course of the fermentation in both the control and biased reactor, which is likely the result of consumption of these redox active species as well as biofilm establishment which insulates the electrode.

Choi et al. reported a more than 2-fold increase in butanol productivity as the result of a -200mV applied potential[107], but HPLC analysis of fermentation supernatants showed no butanol production in biased or control reactors, and no influence of this applied potential on metabolism. While replication of this experiment is necessary, it is possible that the results reported by Choi et al. were caused by unintended background reactions, such as corrosion of the working electrode assembly.

4.4.3 Redox control without direct electron transfer

In RCM experiments, metabolic shifts were observed with an applied potential of -600mV vs. Ag/AgCl, but no changes were observed in electron transfer behavior between electrodes and biofilms as the result of this applied bias. This indicates that an applied potential of -600mV vs. Ag/AgCl, which is slightly more negative than the ORP of an unbiased control, can induce metabolic shifts through redox control, but direct microbe-electrode interaction likely did not occur. In the absence of direct electron transfer, extracellular redox control can alter the function of redox-dependent enzymes, therefore inducing metabolic changes without direct consumption of supplemented electrons[141,142].

90

The observed metabolic shift favored butyrate production over acetate, indicating that the application of a reducing potential can lead to increased production of more reduced products. Previous studies have indicated that redox control could induce earlier onset of solventogenesis in fermentations of *Clostridium acetobutylicum*[143]. However, solventogenesis was not induced by applied potentials in our pH-controlled experiments. Reports of ORP control inducing solventogenesis were observed using aeration, which may have triggered a stress response resulting in onset of solventogenesis. Furthermore, without pH control, it is possible that redox control can result in increased production of acids, leading to a drop in pH, which is known to trigger solvent production.

4.4.4 Evidence of Direct Electron Transfer

When a more negative potential of -750mV vs. Ag/AgCl was applied, changes in electron transfer behavior were observed, indicating that direct electron transfer may be induced. The redox reaction centered at -400 mV vs. Ag/AgCl corresponds closely with the redox potential of riboflavin. Figure 32 shows the CV scan of C. pasteurianum after 24 hours at an applied potential of -750 mV vs. Ag/AgCl overlayed with a CV scan of riboflavin. This result provides evidence that riboflavin may be secreted as redox mediator as a response to applied potential. However, despite electrochemical evidence for DET, metabolite profiles were less affected at -750 mV than at -600 mV vs. Ag/AgCl. While butyric acid production was increased slightly, this occurred at the expense of ethanol and lactic acid production rather than acetic acid. Additionally, while changes in cyclic voltammograms were observed, no measurable current was consumed. These results suggest that a flavin-based EET mechanism may be present in *C. pasteurianum,* but do not provide sufficient evidence for cathodic DET.

91

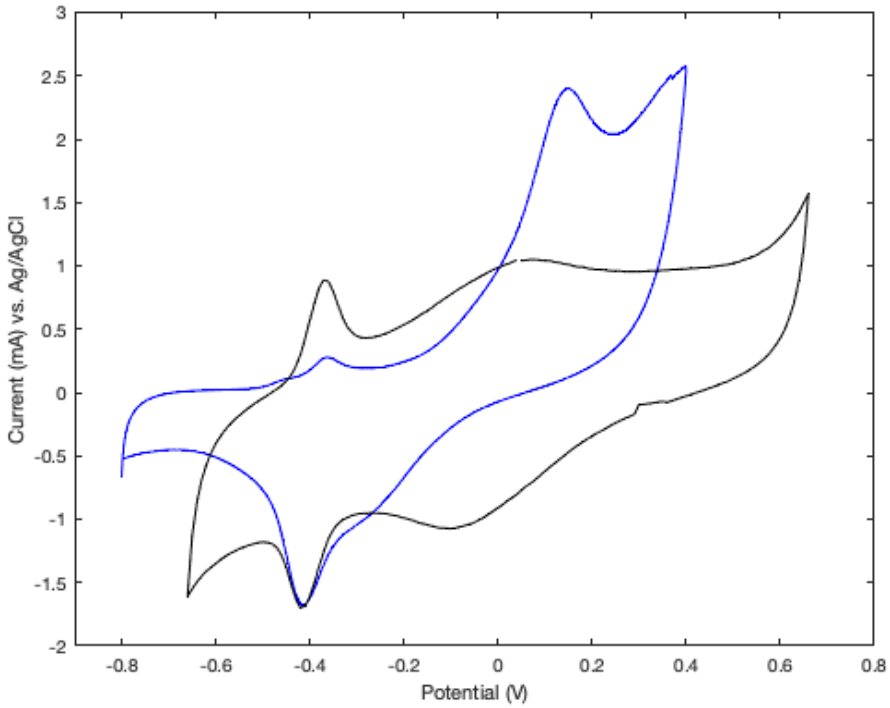

Figure 32: CV of *C. pasteurianum* after 24 hours at an applied potential of -750 mV vs. Ag/AgCl (blue) and riboflavin in growth medium (black).

4.5 Conclusions and Future Directions

This work provides evidence that *C. pasteurianum* metabolism can be influenced through redox control. Applied potentials may induce metabolic shifts by controlling the ORP of a fermentation and influencing transmembrane ion gradients involved in regulation of metabolic pathways, or by inducing direct microbe-electrode interactions. Further experiments are necessary to understand the effect of electrochemical bias on fermentation of *C. pasteurianum*.

Under the conditions investigated, butanol production through solventogenesis was not observed. *Clostridia* undergo biphasic fermentation, where solventogenesis is initiated as a response to both redox conditions and pH[144,145]. Solventogenic metabolism allows regeneration of NAD^+ and is induced by decreased pH associated with the accumulation of acetic and butyric acid [144,145]. Here, pH was controlled due to the complex interactions among pH, ORP, and

92

electrochemistry, and to determine whether an applied potential could induce solventogenesis in conditions that would not typically favor this metabolic switch. Future experiments should be performed without pH control to encourage solventogenesis. Other conditions affecting that may affect microbial EET should also be investigated. For example, EET mechanisms may only be induced under substrate or iron limitation[110,146].

Proteomic and transcriptomic analysis could provide valuable insights to the effect of applied potential on cellular processes. Proteomic analysis can be used to identify extracellular, cell-wall-bound, and membrane-bound proteins that may play a role in cathodic EET mechanisms. Biofilm quantification and characterization should be performed to determine the effect of applied potential on biofilm growth and composition. Biofilm imaging can be used to observe morphological changes that may be induced by applied potentials, such as growth of conductive cell appendages.

93

CHAPTER 5: ELECTRO-ENHANCED ANAEROBIC DIGESTION

5.1 Introduction

In traditional anaerobic digestion (AD), organic wastes such as manure and food waste are broken down by a series of complex microbial processes to produce biogas. While this technology couples waste management with the production of a renewable fuel, methane, the primary component of biogas, is a potent greenhouse gas with low economic value. In contrast, intermediate AD products, such as volatile fatty acids (VFAs), can be used to produce high-value chemicals and liquid transportation fuels. Increasing the production of VFAs while reducing biogas generation improves the economic and environmental sustainability of AD as a low-carbon technology.

In AD, feedstocks typically consist of a mixture of complex biopolymers, which cannot be readily metabolized by bacteria. In the first stage of anaerobic digestion, hydrolytic bacteria secrete enzymes to digest organic molecules into sugars, fatty acids, and amino acids[147]. These smaller molecules become accessible to acidogenic bacteria, which ferment sugars and amino acids to produce primarily VFAs and CO_2 but may also produce alcohols and H_2[148]. VFAs such as propionate and butyrate that are produced in acidogenesis may then be consumed by acetogens, producing acetate. Finally, in methanogenesis, intermediates are consumed by methanogenic archaea to produce methane. Acetate is consumed by acetoclastic methanogens, while hydrogen and CO_2 are consumed by hydrogenotrophic methanogens. The processes of AD are shown in figure 33.

94

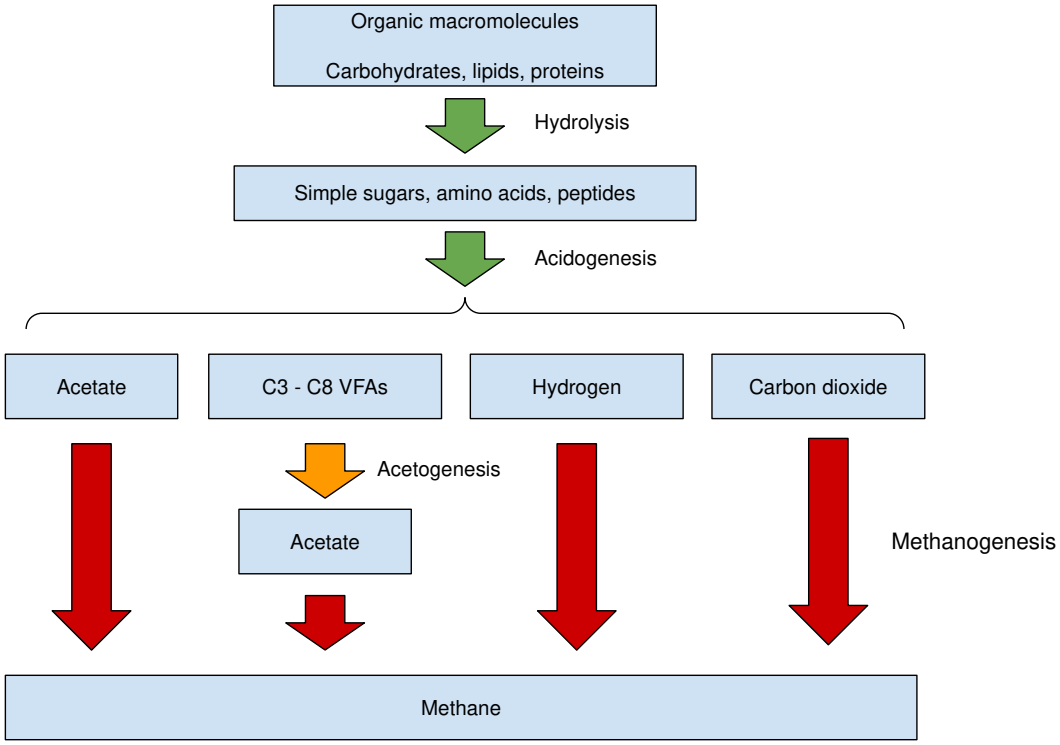

Figure 33: The processes involved in anaerobic digestion: hydrolysis, acidogenesis, acetogenesis, and methanogenesis.

Each of these processes, and the resulting product profile, is highly dependent on AD conditions such as pH, temperature, feedstock composition, and microbial community structure. In electro- enhanced anaerobic digestion (electro-AD), renewable electrons may influence these processes at the community and cellular levels, increasing production of more reduced VFAs and limiting their consumption through acetogenesis and methanogenesis.

In pure culture electro-fermentations with electroactive bacteria, it has been demonstrated that electrons can be delivered directly to microorganisms from an electrode to alter the intracellular NADH/NAD+ balance, inducing a metabolic shift that favors NADH-consuming pathways, therefore increasing yields of more valuable, reduced products. Similarly, it has been reported that applied electrochemical potentials may influence processes in AD[149–154].

95

Direct interspecies electron transfer (DIET) has also been observed in anerobic digestion. In DIET, DMRB can couple oxidation of organics to direct electron transfer to other bacteria, creating syntrophic relationships between electroactive bacteria and hydrogenotrophic methanogens[152]. With diverse, mixed-culture AD inocula, we have shown that applied potentials lead to the establishment of electroactive biofilm communities on the electrode, and under certain conditions, electro-AD significantly increases VFA yields. We hypothesize that, at the cellular level, supplemental electrons induce the metabolic shifts observed in electro-fermentation, leading to increased yields of more reduced metabolites. By combining electrochemical, metabolomic, and taxonomic analyses of small-scale electro-AD in a highly controlled reactor system, we can elucidate mechanisms of microbe-electrode interactions that lead to increased production of high-value metabolites. Understanding these complex interactions is necessary to design effective electro-AD systems in the future.

5.2 Materials and Methods

5.2.1 Inoculum and Feedstock Sourcing

Anaerobic sludge was obtained from anaerobic digesters at the Drake Wastewater treatment facility and stored in sealed bottles at 3C. New inoculum was sourced at least every 3 months. Food waste was sourced from the Academic Village Rams Horn Dining Hall at CSU. Immediately after collection, food waste was stored at 4C. Food waste was then homogenized in batches by mixing 500mL of food waste with 500mL deionized water and blending in a Vitamix blender. Batches were transferred to a 55-gallon container and further mixed using an electric paint mixer. Homogenized food waste was then aliquoted in Ziploc bags and frozen for long term storage. Prior to the start of electro-enhanced AD experiments, several bags of

96

homogenized food waste were thawed and further divided into 30 g aliquots in falcon tubes and refrozen until use.

5.2.2 Experimental Design

Each experiment consisted of two biased reactors, poised at a specified potential, as well as two unbiased control reactors, which were operated at open circuit potential (OCP). Due to the variability of the inoculum, it was determined that sequential experiments could not be compared directly, so replicates and controls needed to be operated simultaneously using the same inoculum. Abiotic controls with applied potentials were performed separately.

5.2.3 Bioelectrochemical System

Electro-enhanced anaerobic digestions were performed in H-cell reactors with Nafion 117 cation exchange membranes separating the working and counter electrodes. The counter electrode material was platinized titanium mesh. For the working electrodes, 2.5cm x 5cm pieces of carbon felt were pretreated by soaking in 10% isopropanol for at least 24 hours, followed by 3 rinses in deionized water. Titanium wire sealed in the working electrode compartment rubber stopper was woven through the carbon felt working electrode. The Ag/AgCl reference electrode was sealed in the same rubber stopper, which also held a pH probe. pH was monitored at open circuit potential on a PC using an Arduino-based controller and an analog pH circuit (Atlas Scientific).

5.2.4 Electro-Enhanced Anaerobic Digestions

For each experiment, H-cells were assembled and 250 mL of de-aired water (autoclaved and purged with nitrogen gas) was added to the working electrode chamber. Two falcon tubes of aliquoted homogenized food waste were thawed at room temperature, and 15 g of food waste

97

was added to each reactor for an organic loading rate of 5 gCOD/L. Reactors were then purged with high purity nitrogen for at least 2 hours, then sealed, and pH was adjusted using 1N HCl. After pH adjustment, each reactor was inoculated with 60mL of anaerobic sludge and purged for an additional 20 minutes. Tedlar gas bags were then attached to each reactor to collect biogas. Counter electrode chambers were filled with 100mM KCl. All experiments were performed at a pH of 7 unless otherwise noted. pH control was performed manually unless otherwise noted. Manual pH control was performed daily. pH was measured using pH paper, and adjusted with 1N HCl.

H-cells were incubated at 35°C and magnetic stir bars were used to maintain agitation at 200 rpm. A CH instruments 1000C multi-potentiostat was used to perform cyclic voltammetry (CV) and chronoamperometry (CA). CV was performed on all reactors immediately after inoculation and daily after pH adjustments at a scan rate of 2mV/s. CA was used to apply specified potentials in biased reactors only. Unbiased controls were left at OCP. Experiments were run for at least 10 days. In some cases, additional food waste was added after 10 days to see the effect of feeding on VFA production.

5.2.5 Analytical Methods

Gas chromatography with mass spectrometry (GC-MS) was used to quantify C2-C7 VFAs. An Agilent 6890 GC coupled with a 5973A MSD detector was used with an Agilent DB wax column of dimensions 30 m x 0.25 mmx 0.25 μm. Mixed VFA standards of concentrations 1 mM, 3 mM, 5 mM, 7 mM and 10 mM were made from a stock solution purchased from Sigma-Aldrich containing 10 mM acetic, propionic, isobutyric, butyric, isovaleric, valeric, isocaproic, caproic, and heptanoic acid. For GC-MS analysis, an injection volume of 1 μL was used with a

98

split ratio of 3:1. The carrier gas was helium at a flow rate of 1 mL/min. The inlet temperature was 250°C. The oven temperature started at 60°C for 5 minutes, then increased to 150°C at 5°C/min. The temperature was then held at 150°C for 5 minutes before increasing again at 5°C/min to 250°C and held constant for an additional 10 minutes.

Three mL of AD sludge (two 1.5 mL samples in 2 mL collection tubes) were collected from each reactor daily. Samples were centrifuged immediately after collection and the solid pellets and supernatant were stored separately at -80°C. Before GC-MS analysis, supernatant samples were thawed and recentrifuged to remove any residual solids. The pH of the supernatant was then acidified to a pH of 2-3 using 2N HCl then filtered through a 2 μm syringe filter. Two separate samples were prepared for each reactor at each sample time as technical replicates. Samples and standards were randomized for GC-MS analysis.Gas samples were analyzed for methane and CO_2 composition at room temperature via gas chromatography using a Hewlett Packard Series 2180 gas chromatograph equipped with an Alltech column packed with HayeSep Q 80/100 mesh. 10 μL of gas sample was injected and a split ratio of 40:1 was used. The carrier gas was helium at a flow rate of 3.3 mL/min. Inlet and detector temperatures were maintained at 200°C.

5.2.6 Electrochemical methods

A CH instruments 1000C multi-potentiostat was used for all electrochemical analysis. Electrochemical experiments were performed directly in H-cells using the bioelectrode as a working electrode, a Ag/AgCl reference electrode (Pine Research RRPEAGCL-110), and a platinized titanium counter electrode. CV was performed at a scan rate of 2 mV/s. For each CV, two sequential scans were performed, and the second scan was used.

99

5.2.7 16s Sequencing

Solid pellets from daily liquid sampling were stored at -80°C for later DNA extraction. Biofilms were harvested and pelleted at the end of each experiment. To pellet electrode biofilms, the electrodes were removed from each reactor and placed in 30 mL of PBS in falcon tubes. The tubes were then vortexed for 30 minutes and centrifuged. PBS supernatant was decanted, and the pellets were resuspended in 5 mL PBS and vortexed again for 5 minutes. The resuspended pellets were then dispensed into microcentrifuge tubes and centrifuged again. Supernatant PBS was again discarded, and the biofilm pellets were stored at -80°C. For DNA extraction, pellets were thawed at 3°C, and a ZymoBIOMICS DNA Miniprep kit was used.

The following procedure was followed for library preparation:

> "16S rRNA gene Illumina amplicon libraries were constructed based on the Earth Microbiome Project protocol (Earth-Microbiome-Project, 2018). Polymerase Chain Reaction (PCR) was performed on each of the DNA extracts using single barcoded primers (515F and 926R) flanking the 16S rRNA gene V4 region. Unique barcodes were present on each of the forward primers (Single-index Illumina sequencing). The PCR was carried out on a Bio-Rad thermocycler (Bio-Rad Laboratories, location), using a Platinum Hot Start PCR Master Mix (2X) (ThermoFisher, Waltham, Massachusetts); 50 µL reactions were conducted by a denaturation step at 94°C for 3 min, followed by 30 cycles of 94°C for 45 s, 50°C for 60 s, and 72°C for 90 s, concluding with an extension step at 72°C for 10 min. Amplicons were kept at 4°C before further library processing. Reaction products (5 µl) were screened on a 1% agarose TAE (Tris-acetate EDTA) gel, using a Gel electrophoresis system (Bio-Rad Laboratories, Hercules, CA) to verify successful amplification. Blank amplicon controls (PCR reactions without DNA template) and DNA extraction negative controls (PCR reactions with a template from a blank DNA extraction) were screened to account for potential contamination either in the PCR master mix or in the DNA extraction kit. After the gel electrophoresis verification, 3 µL of each PCR amplification product were combined in a single microcentrifuge tube. The pooled library was then purified using SPRI (Solid Phase Reversible Immobilization) magnetic beads (Sera-mag SpeedBeads, Fisher, Hampton, NH). 280 µL of SPRI beads were combined with the pooled library and incubated at room temperature for 2 min. The mix was then transferred to a magnetic rack (Reference, location) to allow magnetic bead separation (4 min). Three 70% ethanol washes were performed followed by 15 min room temperature drying. The dried pellet was then resuspended in 50 µL of nuclease-free water and incubated at room temperature for 2 min. The suspension was then transferred

> back to the magnetic rack for bead separation (~2 min). The DNA-containing supernatant was finally transferred into a new microcentrifuge tube. Sequencing was performed with the Illumina MiSeq platform (Illumina, Inc, San Diego, CA) at the Colorado State University Next Generation Sequencing Facility."[155]

Operational taxonomic units were identified using QIIME[156]. β-diversity was calculated in QIIME using weighted Unifrac distances and represented in Principal Coordinate Analyses (PCoA). PCoA was performed using all sequenced samples for each experiment, but only T0 and T12 are considered here. The inclusion of other time samples influences the analysis, and greater separation would be shown if these samples were omitted for statistical analysis. MaAsLin was used to identify differentially abundant features between biased and control reactors in each experiment[157].

5.3 Results

5.3.1 Chronoamperometry

Chronoamperometry was used to maintain applied potentials and monitor current generation and consumption during anaerobic digestion. Representative chronomaperograms from all potentials investigated are shown in figure 34. Detailed views of current measured at each applied potential are shown in figures 35-38. Charging currents are minimized my removing the first 50 data points from each segment. This manipulation allows sustained currents to be shown more clearly, especially when sustained currents are small relative to charging currents.

An applied potential of -300mV vs. Ag/AgCl resulted in a large anodic current that developed after several days of operation. At the beginning of the experiment, -300mV vs. Ag/AgCl produces a small negative (cathodic) current (Figure 35 inset). Within 30 hours, anodic currents of equally small magnitude were observed indicating that the oxidation reduction

101

potential of the digestion had decreased due to residual oxygen consumption and metabolic activity, but no significant biotic or abiotic redox reactions were occurring. During day 3, an anodic current becomes apparent, indicating the establishment of an electrode-respiring biofilm. Under batch operation, the current reaches a maximum of 4.54 mA on day 5, corresponding to a current density of 0.35 mA/cm^2. An applied potential of -500mV vs. Ag/AgCl results in very small magnitude currents. Here, it is difficult to propose a maximum value of the "sustained current" as background charging currents are significantly larger than sustained currents. However, in figure 36 a small, sustained current reaches a maximum of -1.2 μA, or 0.09 $\mu A/cm^2$, on the second day of the experiment. However, sustained current level quickly decrease to near zero. An applied potential of -600mV vs. Ag/AgCl results in a small cathodic potential, which reaches an average value of about -0.01 mV on day 2, then decreases to μA levels by day 4 (Figure 37). A bias of -700 mV was applied to two biased reactors (Figure 38).On day one, initial currents of -0.1mA are consumed, but rapidly decrease to approximately -0.025mA. These initial currents may be the result of background electrochemistry. By day three, currents in both reactors have stabilized at levels suggesting they are within the cathodic regime, but without significant biotic or abiotic reactions. On day three, the applied potential of one biased reactor was increased to -750mV vs. Ag/AgCl, resulting in small but constant current consumption.

102

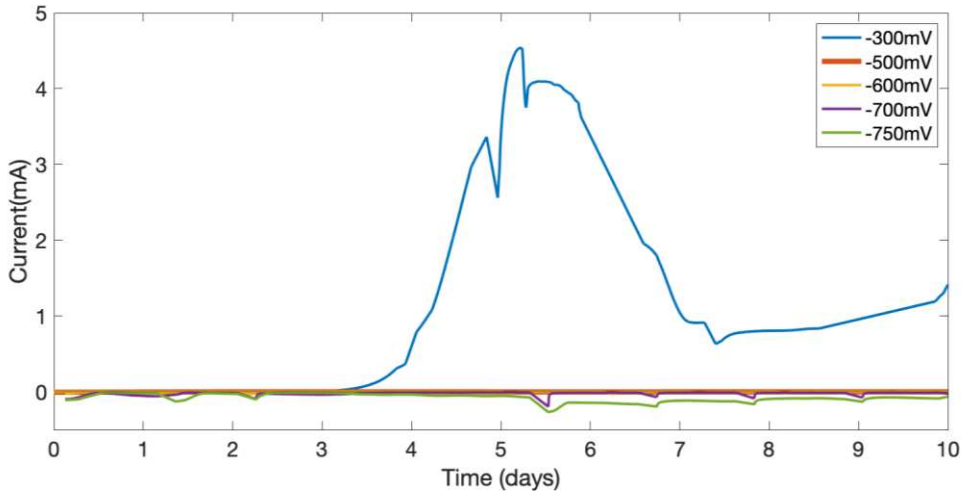

Figure 34: Chronoamperograms of all tested potentials: all potentials are vs Ag/AgCl. -300mV (blue), -500mV (orange), -600mV (yellow), -700mV (purple), and -700 to -750mV (green). For experiments with biological replicates (all traces except -700mV and -750mV), chronoamperograms displayed are the average of current measured for the duplicate reactors.

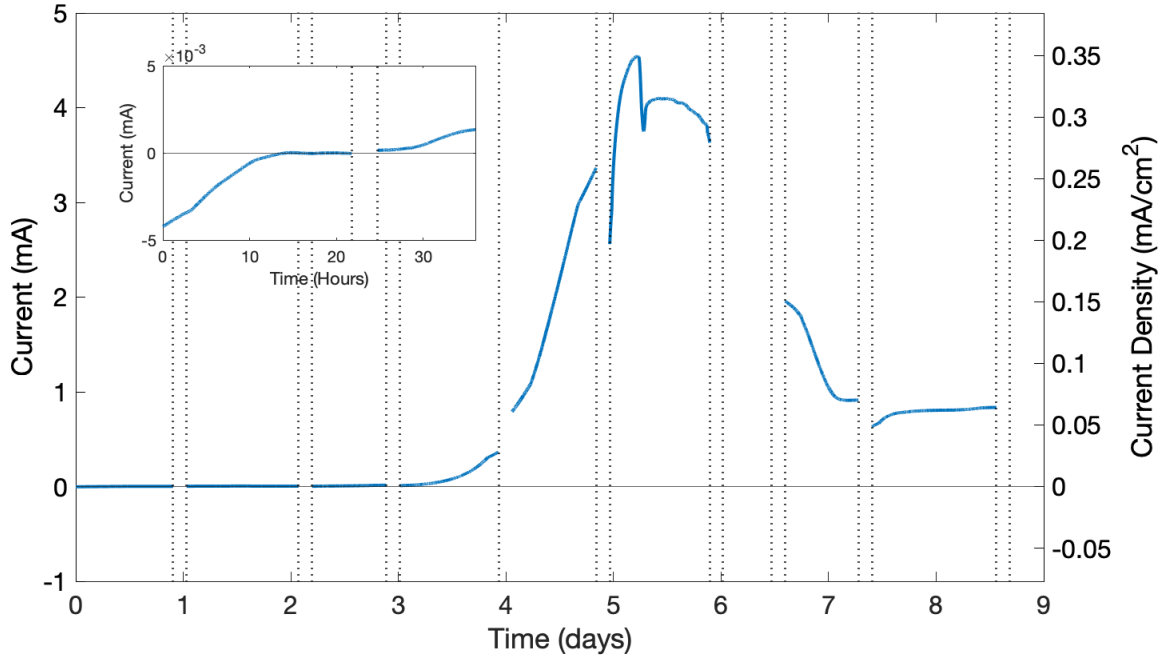

Figure 35: Detailed view representative chronoamperogram of reactors in -300mV experiment. Dashed vertical lines indicate when CA was paused to perform CV and collect samples. Note that CA data for day six and day nine is omitted due to technical issues, but CA was performed during these times.

103

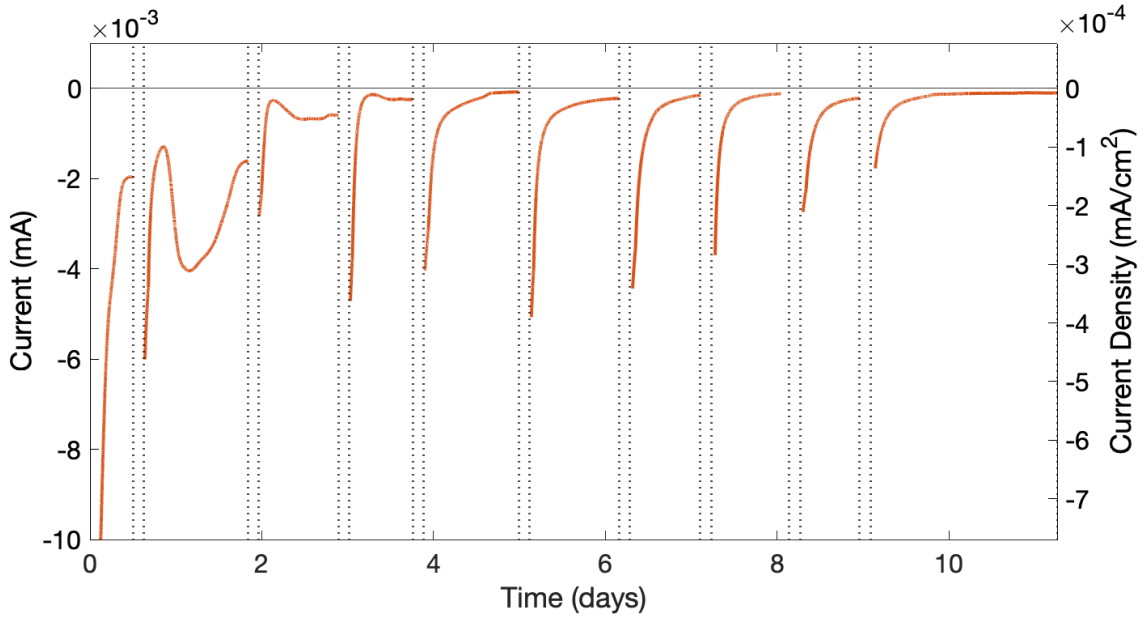

Figure 36: Detailed view representative chronoamperogram of reactors in -500mV experiment. Dashed vertical lines indicate when CA was paused to perform CV and collect samples.

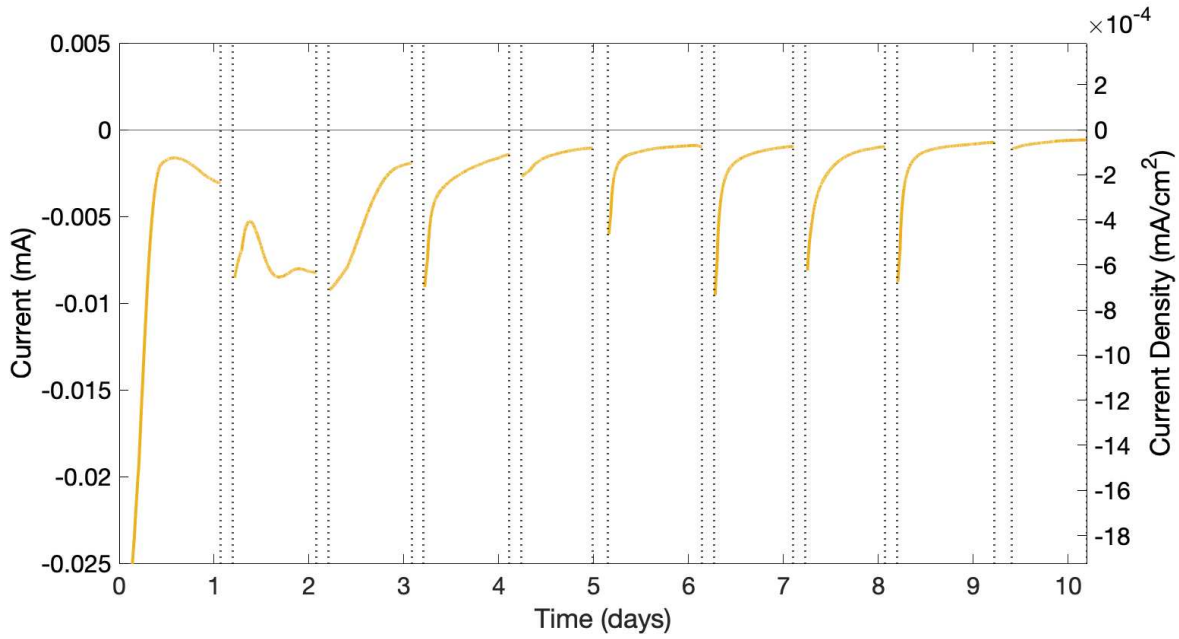

Figure 37: Detailed view representative chronoamperogram of reactors in -600mV experiment. Dashed vertical lines indicate when CA was paused to perform CV and collect samples.

104

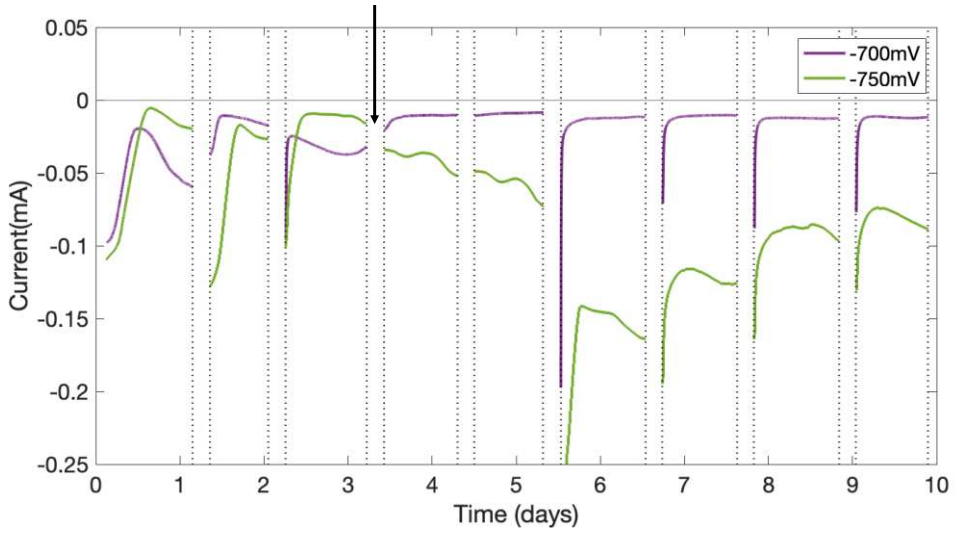

Figure 38: Detailed view representative chronoamperograms from reactors in -700/750mV experiment. Both biased reactors were poised at -700mV vs. Ag/AgCl for the first 3 days, when the applied bias in one reactor was increased to -750mV vs. Ag/AgCl, indicated by the arrow. Dashed vertical lines indicate when CA was paused to perform CV and collect samples.

5.3.2 Cyclic Voltammetry

Slow scan rate (2mV/s) CV was performed on biased and control H-cells each day to monitor electron transfer behavior of biofilms. Figure 39 shows cyclic voltammograms taken in biased and control reactors throughout the experiment at -300mV vs. Ag/AgCl. The scan from day 6 shows catalytic turnover, indicative of an electroactive biofilm. By day 10 the magnitude of this catalytic wave decreased. The last panel shows how the electron transfer behavior in the biased reactor changed over time. Note that, while replicates were performed, only one CV per treatment is shown when replicates exhibited the same electron transfer behavior. CV scans taken over the course of the experiments at -500mV and -600mV vs. Ag/AgCl (Figures 40 and 41) show that the applied bias has no effect on biofilm redox behavior. At an applied potential of -700mV vs. Ag/AgCl, additional reductive peaks are observed in biased reactors (Figure 42). When the applied potential of one reactor (biased 2) was changed from -700mV to -750-mV vs. Ag/AgCl on day three, further changes are observed in cyclic voltammograms by day six, with

105

additional oxidation and reduction peaks appearing at -560mv and -464mV vs. Ag/AgCl, respectively.

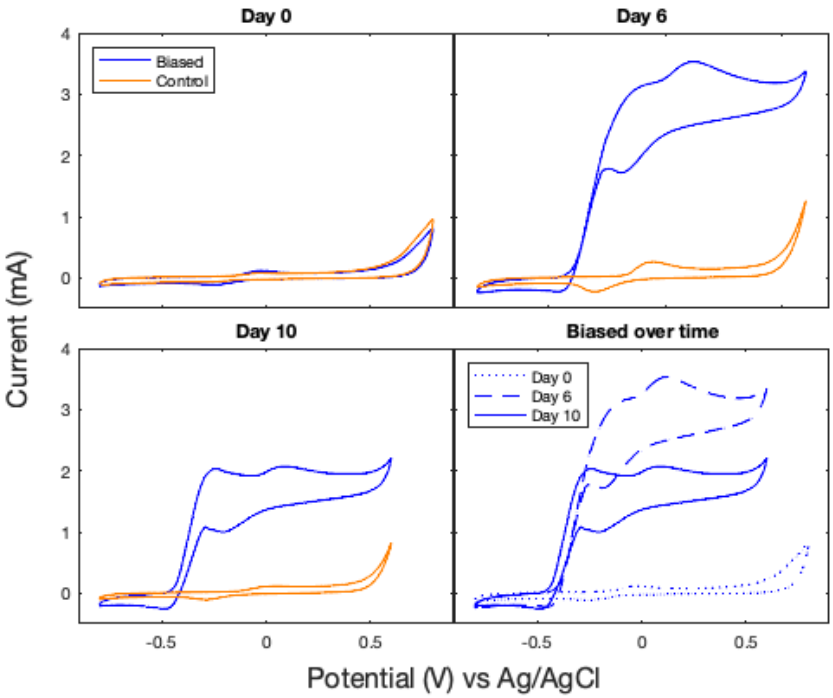

Figure 39: Slow scan rate (2mV/s) cyclic voltammograms of biased (-300mV vs. Ag/AgCl) and unbiased (OCP) reactors immediately after inoculation (day 0), on day 6, and day 10. The last panel provides a comparison of the biased reactor at each of these times.

106

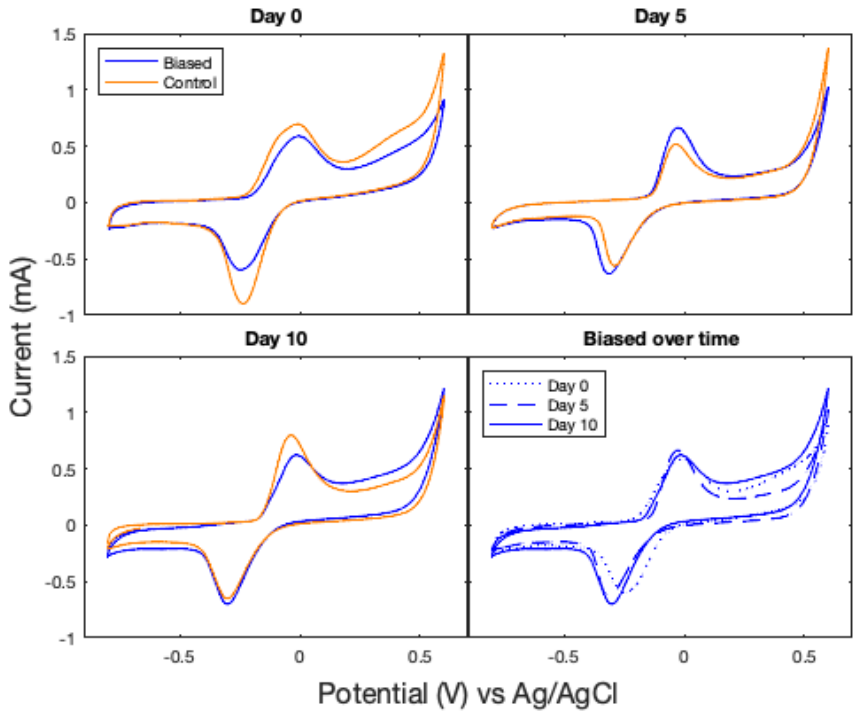

Figure 40: Slow scan rate (2mV/s) cyclic voltammograms of biased (-500mV vs. Ag/AgCl) and unbiased (OCP) reactors immediately after inoculation (day 0), on day 5, and day 10. The last panel provides a comparison of the biased reactor at each of these times.

107

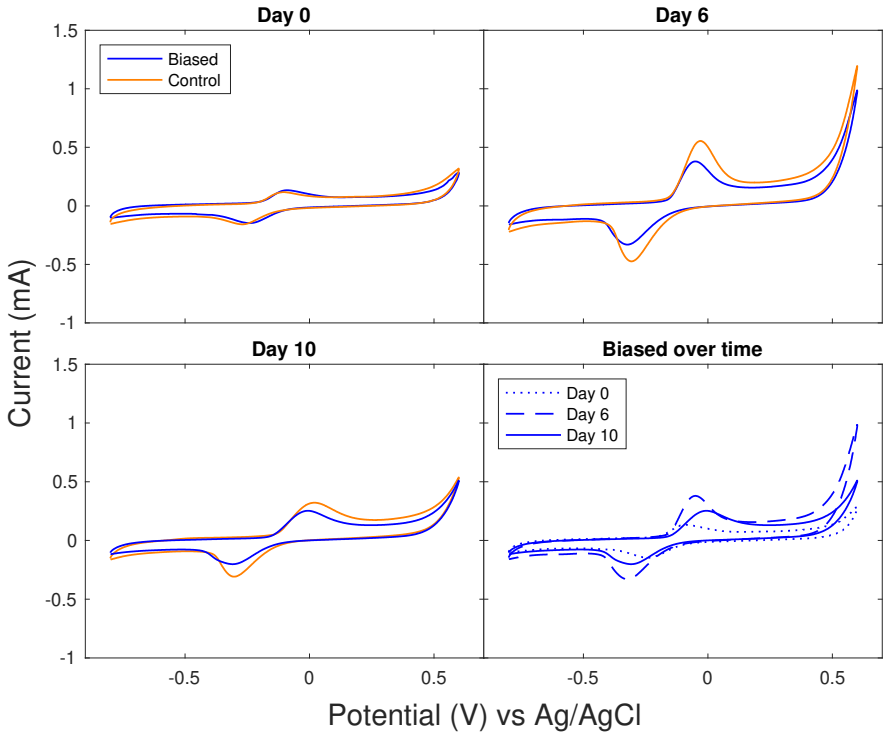

Figure 41: Slow scan rate (2mV/s) cyclic voltammograms of biased (-600mV vs. Ag/AgCl) and unbiased (OCP) reactors immediately after inoculation (day 0), on day 6, and day 10. The last panel provides a comparison of the biased reactor at each of these times.

108

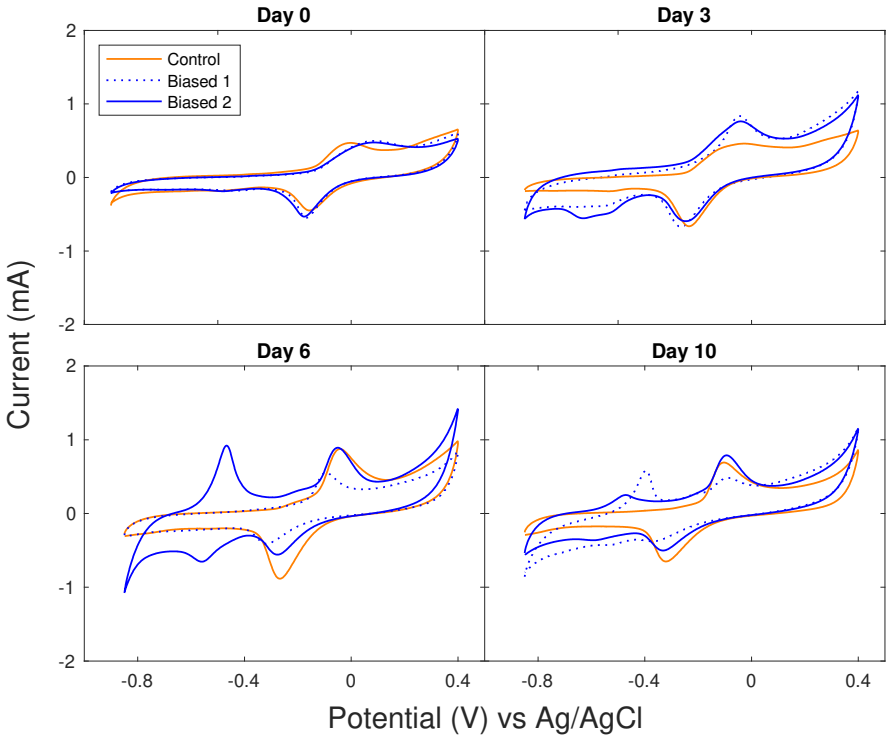

Figure 42: Slow scan rate (2mV/s) cyclic voltammograms of biased (-700mV and -750mV vs. Ag/AgCl) and unbiased (OCP) reactors immediately after inoculation (day 0), on day 3, day 6, and day 10.

5.3.3 Volatile Fatty Acid Profiles

VFA and gas profiles for each applied potential are shown with their respective unbiased controls in figures 43-54. Scatterplots show total VFA concentrations for biased and control reactors, and stacked bar plots are used to show VFA and biogas compositions. Error bars represent the standard deviation of biological and technical replicates unless otherwise noted. Figure 55 provides comparison of total VFA production across all experiments as the percent change in maximum total VFA concentration from each applied potential compared to its respective controls. An applied potential of -600 mV vs. Ag/AgCl showed the most significant increase in maximum total VFA concentration, while -300 mV and -750 mV vs. Ag/AgCl

109

showed the most significant decreases. This result indicates that applied potentials between -500 and -700 mV vs. Ag/AgCl are likely optimal for increasing total VFA concentrations.

5.3.3.1 -300mV vs. Ag/AgCl

The maximum total VFA concentration reached about 2.5 g/L in the biased system, maintaining a steady total VFA concentration between days 2 and 4. The control reactor reached a higher maximum total concentration of approximately 3.5 g/L on day 2. However, in the control system, methanogenesis began immediately after the maximum concentration was reached, with total VFA levels decreasing steadily from day 3 until day 8. Methanogenesis begins after day 4 in the biased system, and total VFA concentrations in biased and control reactors decrease to approximately 1 g/L. VFA distributions are similar in biased and control reactors (Figure 44), with acetic acid accounting for the difference in maximum total VFA concentration between treatments. In both treatments, acetic acid is rapidly consumed during methanogenesis, and propionic and butyric acid concentrations slowly decrease as a result of acetogenesis. On day ten, butyric acid has been consumed almost entirely, and small amounts of C6 acids are measured. Despite producing similar VFA profiles, metabolic processes appear to be affected by this oxidative applied potential, as made evident by differences in final gas composition (Figure 45). While total gas volumes were similar in biased and control reactors (562 and 630 mL, respectively), biased reactors produced an average of 50% CH_4 and 31% CO_2, compared to 70% CH_4 and 10% CO_2 in control reactors.

110

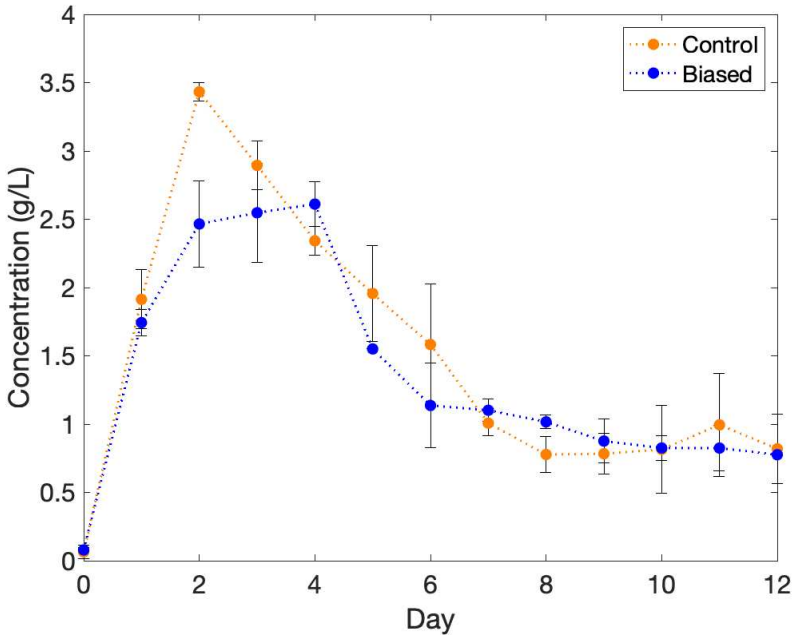

Figure 43: Total VFA concentrations in control and biased (-300mV vs. Ag/AgCl) reactors.

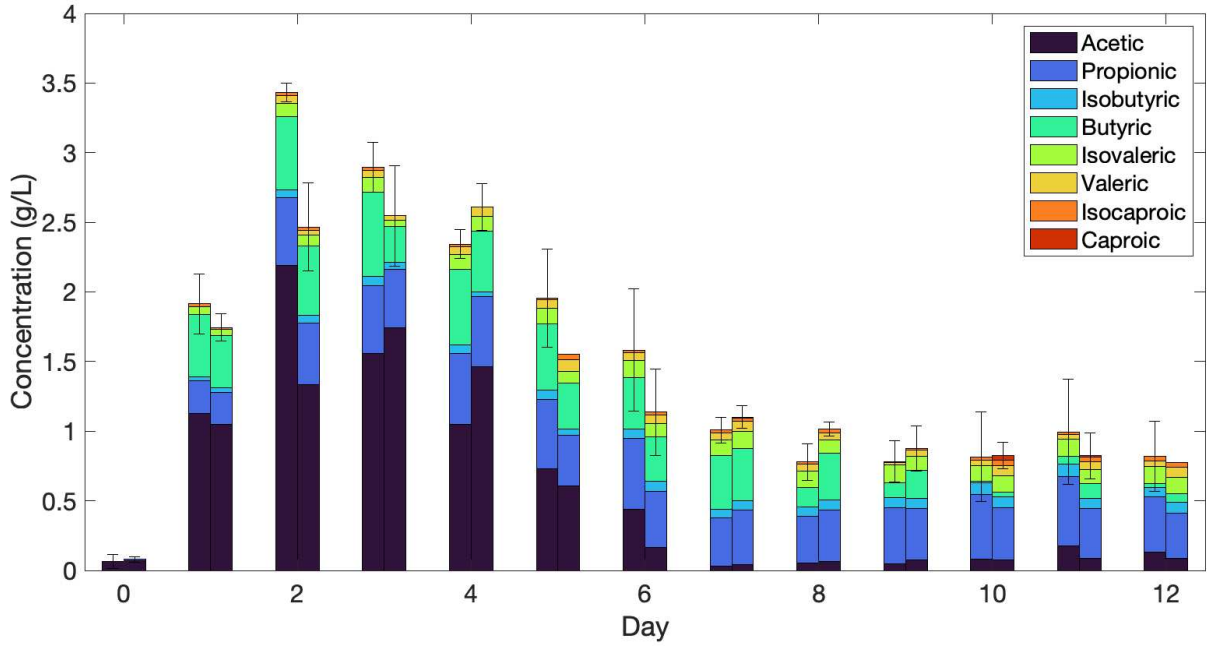

Figure 44: VFA profiles in control (left columns) and -300mV vs. Ag/AgCl biased (right columns) reactors.

111

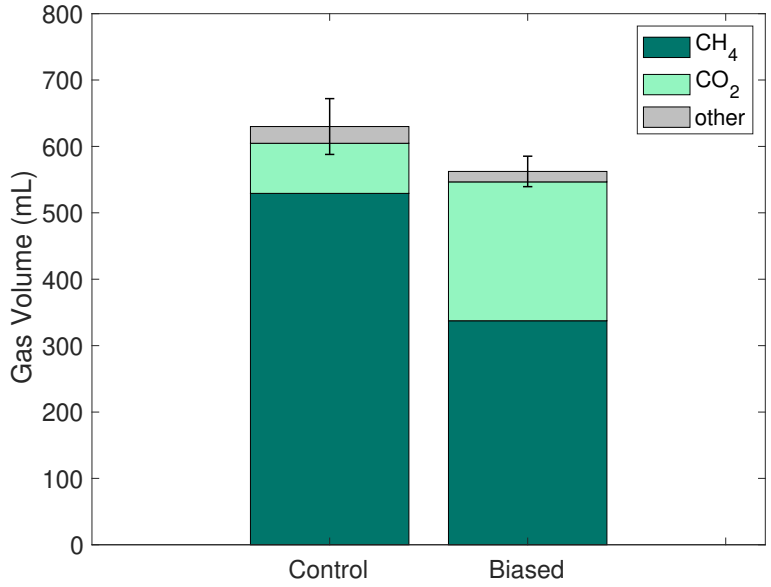

Figure 45: Biogas composition in control and -300mV vs. Ag/AgCl biased reactors

5.3.3.2 -500mV vs. Ag/AgCl

Both biased and control reactors reach similar maxima of approximately 4.5g/L, with controls reaching this maximum on day two, and biased reactors reaching maximum VFA concentrations on day five. As in previous controls, methanogenesis begins in control reactors immediately after the maximum total VFA concentration is reached on day 2. Biased and control reactors reach nearly identical total VFA concentrations on day 10. Acid profiles remain similar between biased and controlled reactors, and again differences in total VFA concentration are primarily attributed to acetic acid (Figure 47). In this experiment, additional food waste was fed to each reactor on day 11, and total VFA concentrations began to increase again. Total gas volumes of 705 mL and 645 mL were collected in biased and control reactors, respectively, with almost identical compositions (Figure 48).

112

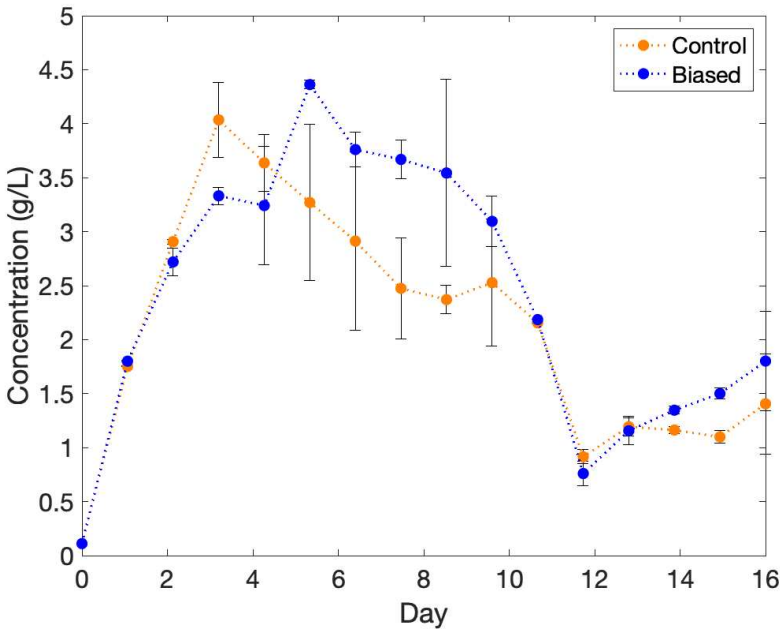

Figure 46: Total VFA concentrations in control and biased (-500mV vs. Ag/AgCl) reactors. Error bars represent standard deviation for two replicates of each treatment.

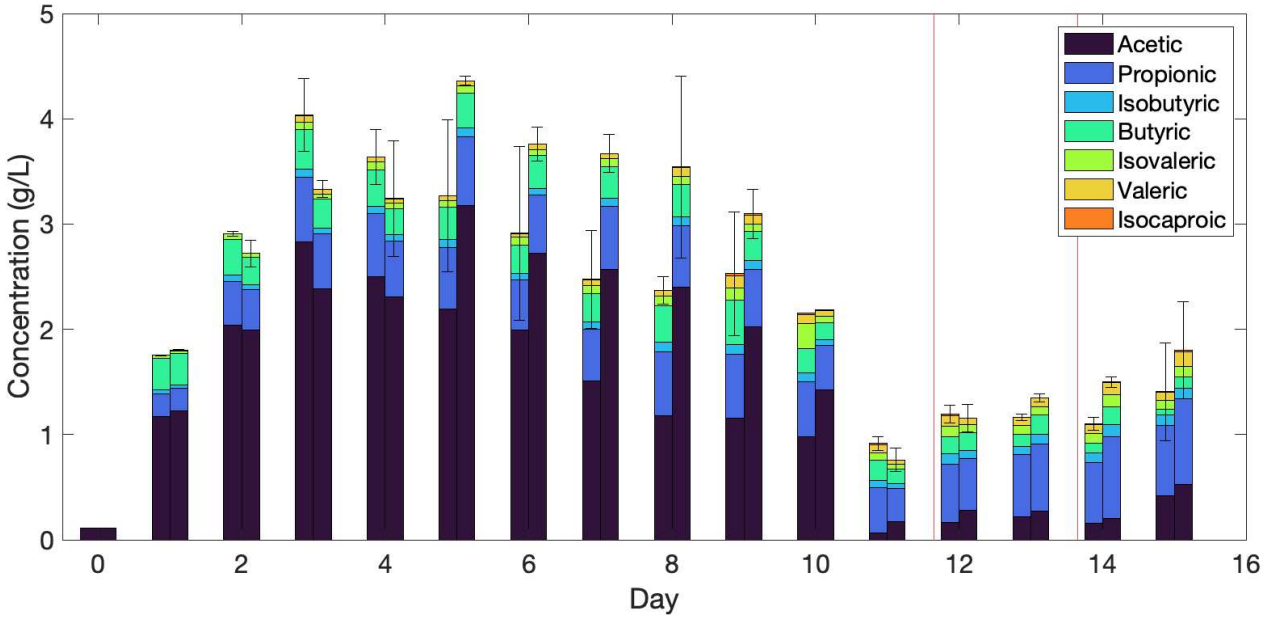

Figure 47: VFA profiles in control (left columns) and -500mV vs. Ag/AgCl biased (right columns) reactors. Red vertical lines indicate the addition of 5g of food waste.

113

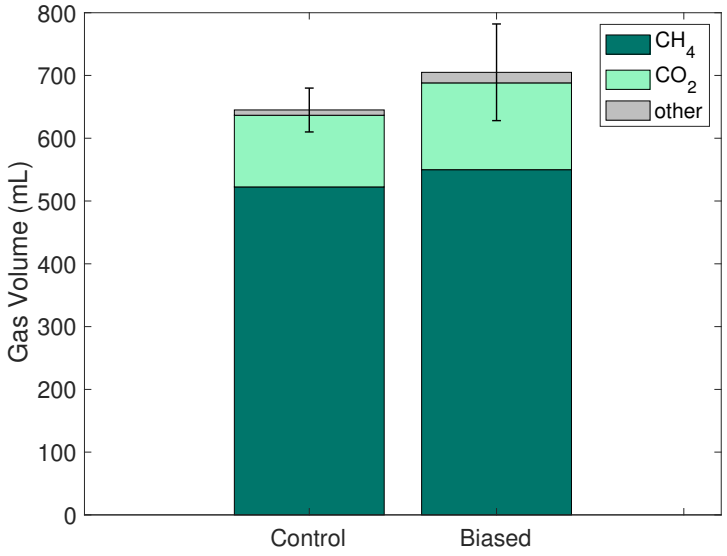

Figure 48: Biogas composition in control and -500mV vs. Ag/AgCl biased reactors

5.3.3.3 -600mV vs. Ag/AgCl

In this experiment, biased reactors reached a maximum total VFA concentration of 2.8 g/L on day five, while control reactors reached a maximum of 2.0 g/L on day 3 (Figure 49). In this experiment, behavior across control reactors showed high variability, with VFA concentrations rapidly decreasing in one control reactor as observed in previous controls. However, in the second control reactor, total VFA concentrations remained relatively constant. The average total VFA concentration in control reactors slowly decreases to approximately 1 g/L by day 12. Total VFA concentrations in biased reactors slowly decrease to 2.25 g/L by day 12. Again, acetic acid accounts for the largest fraction of differences in total VFA concentration, however, isobutyric acid production increases significantly in biased reactors by day 12 (Figure 50). While gas production was varied between control reactors, on average, more gas was produced in controls (425 mL) than biased reactors (305 mL). Methane accounted for most of this volume difference (Figure 51).

114

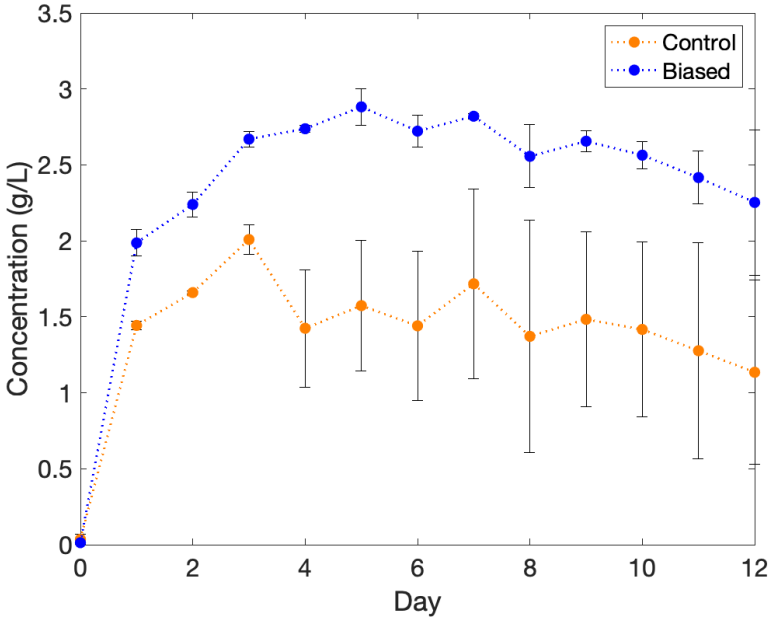

Figure 49: Total VFA concentrations in control and biased (-600mV vs. Ag/AgCl) reactors. Error bars represent standard deviation for two replicates of each treatment.

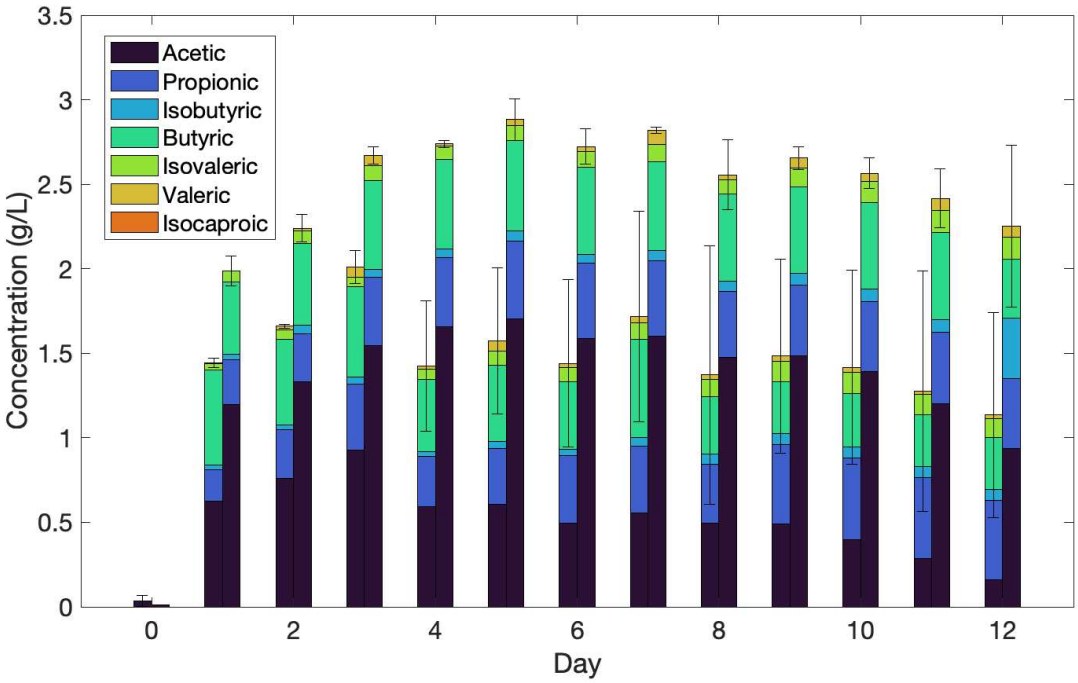

Figure 50: VFA profiles in control (left columns) and -600mV vs. Ag/AgCl biased (right columns) reactors.

115

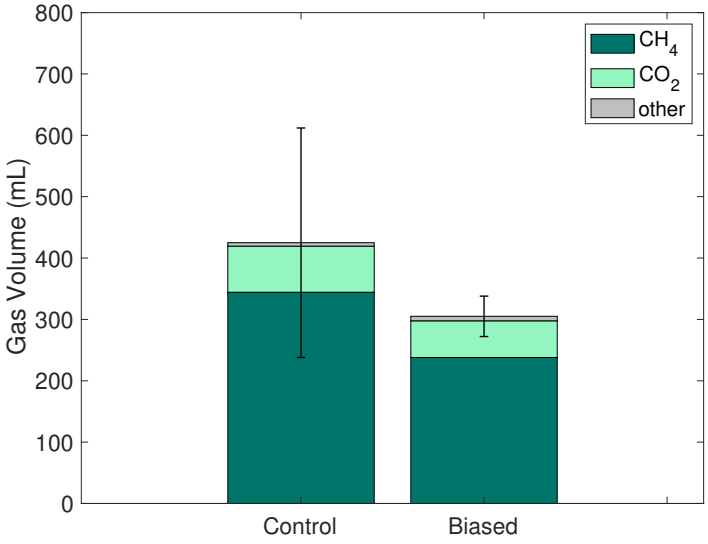

Figure 51: Biogas composition in control and -600mV vs. Ag/AgCl biased reactors

5.3.3.4 -700mV and -750mV vs. Ag/AgCl

In days one to three, lower total VFA concentrations are observed in biased reactors, but the acid profiles begin to shift, with C5-6 acids produced only in biased reactors. On day 3, the applied potential of one biased reactor was changed from -700 mV to -750 mV vs. Ag/AgCl, as indicated by the arrows in figures 52 and 53. This change in applied potential led to a rapid decrease in total VFA concentration, but also resulted in the production of longer chain acids (figures 53 and 64). Interestingly, this consumption of VFAs does not appear to have resulted from methanogenesis, as almost no methane was measured in biogas from this reactor (Figure 54). An applied potential of -700 mV vs. Ag/AgCl resulted in increased CO_2 and decreased CH_4 production, while no CO_2 was detected in the -500 mV reactor.

116

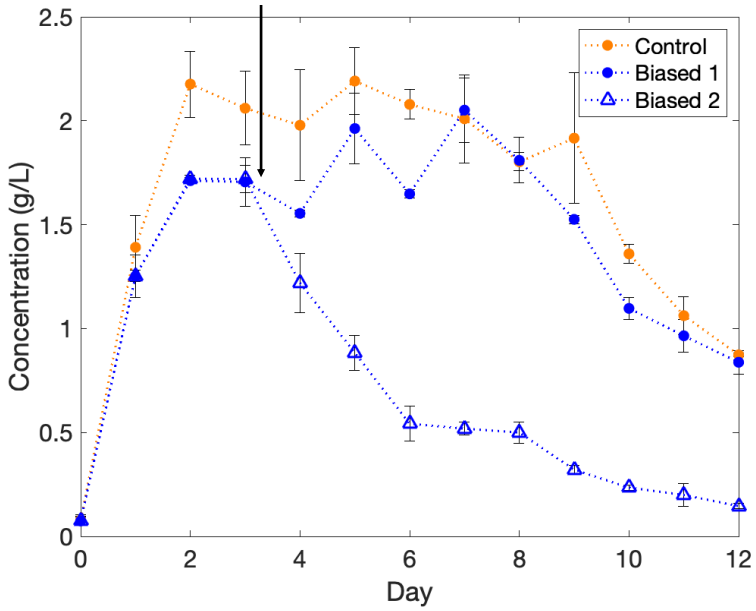

Figure 52: Total VFA concentrations in control and biased (-700mV and -750mV vs. Ag/AgCl) reactors. Error bars represent standard deviation for two biological replicates of the control and technical replicates of B1 and B2 samples. The arrow indicates when the potential of B2 was changed from -700 to -750mV vs. Ag/AgCl.

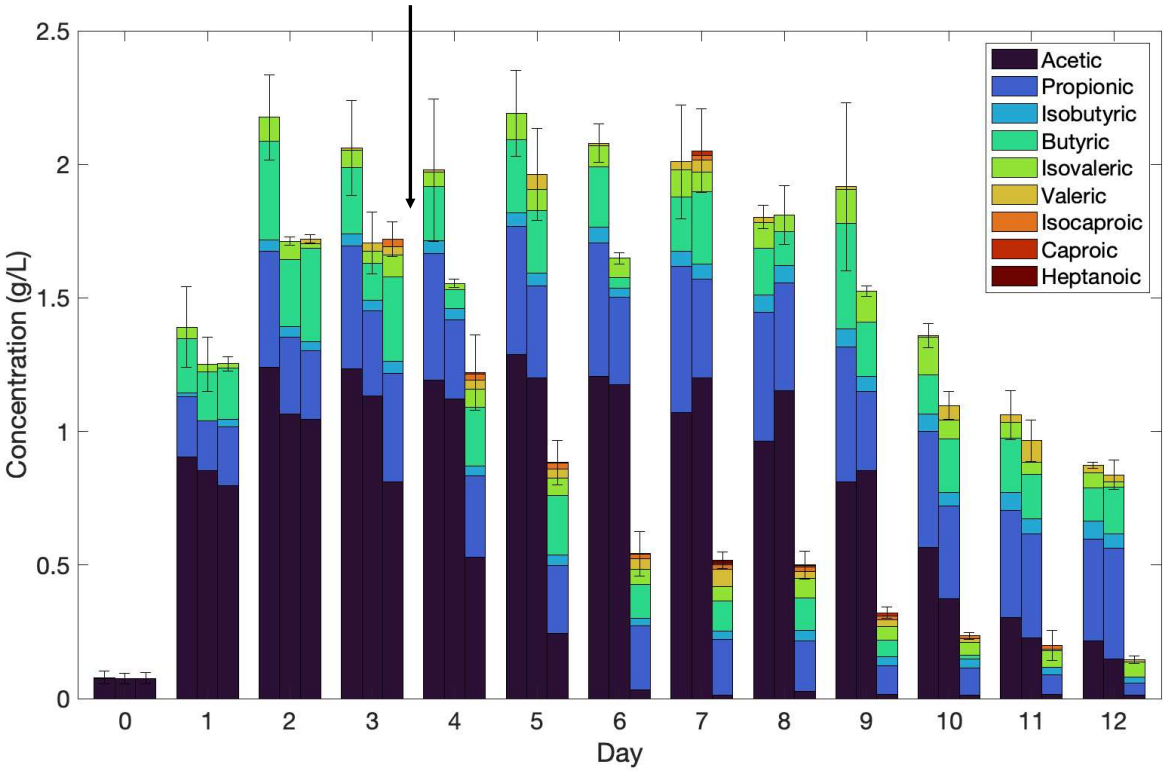

117

Figure 53: VFA profiles in control (left columns), -700 mV vs. Ag/AgCl (middle columns) and -750 mV vs. Ag/AgCl (right colums) reactors. The arrow indicates when the potential of B2 was changed from -700 to -750mV vs. Ag/AgCl.

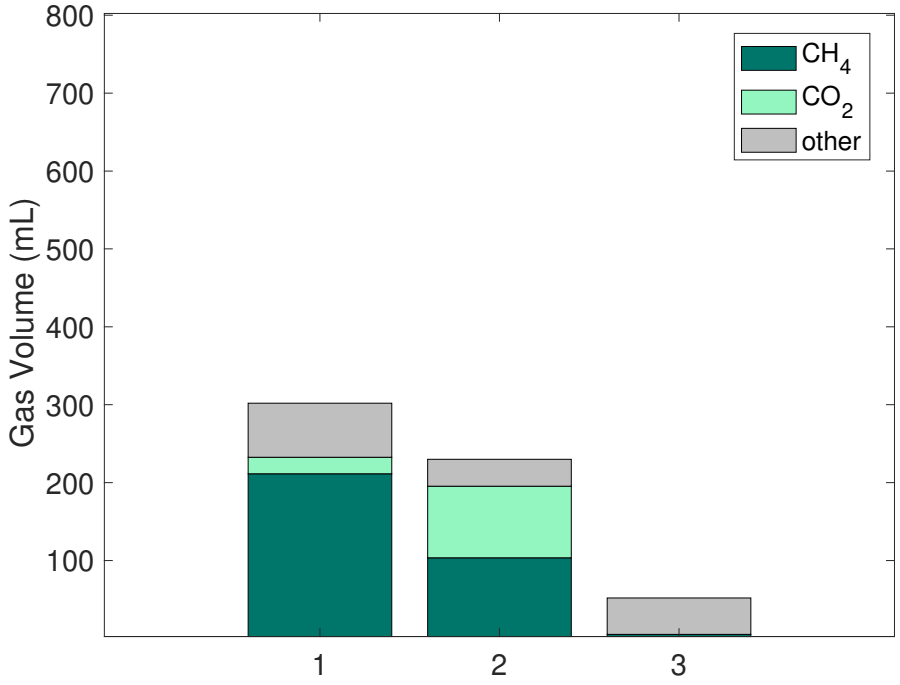

Figure 54: Biogas composition in control, -700 mV, and -750mV vs. Ag/AgCl biased reactors.

118

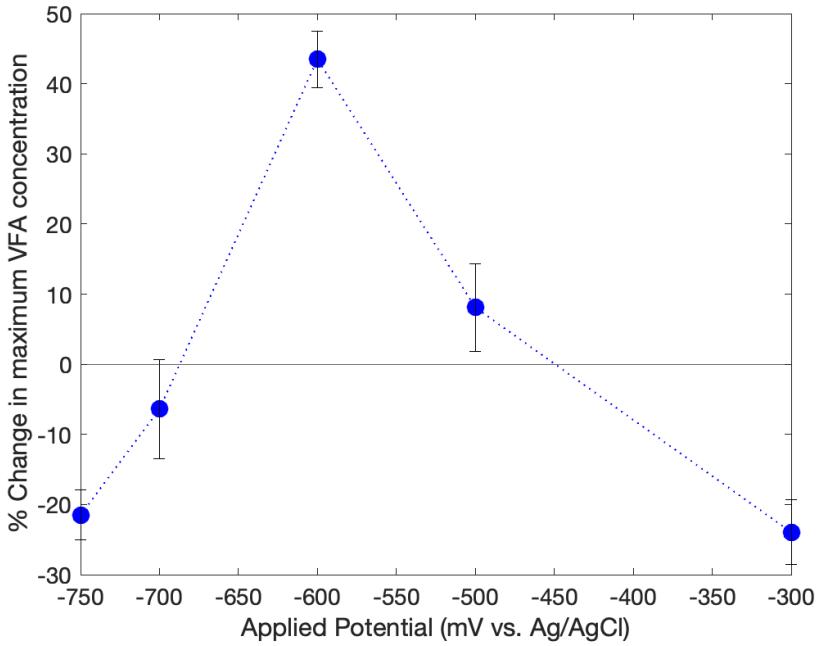

Figure 55: Percent change in maximum total VFA concentration for each applied potential relative to respective controls.

5.3.4 16s Sequencing

Across all samples, 869 features were identified using 16s sequencing. Further information on raw abundance data and DNA amplification can be found in Appendix 2. PCoA of weighted Unifrac distances was used to visualize β-diversity among biased and control samples over the course of each experiment (Figures 56 - 59). UniFrac is a distance metric that uses phylogenetic information to compare samples. PCoA of these phylogenetic distances shows differences in the microbial communities of samples[158]. For each experiment, samples from biased and control reactors are clustered at time zero, showing that the microbial communities are nearly identical at the time of inoculation. Separation of samples along multiple axes by day 12 shows how each treatment affected microbial community structure in reference to controls. At -300 mV vs. Ag/AgCl, clear separation is observed between control and biased samples at day 12, indicating that an applied potential of -300mV vs. Ag/AgCl significantly affects microbial

119

community structure (Figure 56). In contrast, at an applied potential of -500mV vs. Ag/AgCl, we do not see distinct clustering of biased and control samples (Figure 57), suggesting that this applied potential has no influence on microbial community structure. Clustering of biased and control samples can again be observed at an applied potential of -600 mV vs. Ag/AgCl (Figure 58).

MaAsLin was used to identify differentially abundant features between each applied potential and its respective controls. The significant associations identified by MaAsLin represent OTUs that are likely associated with each treatment, i.e., taxa that are augmented or reduced by each applied potential. Thirty-five significant associations were identified in experiments at -300 mV and -600 mV vs. Ag/AgCl, while no associations were found for experiments at -500 mV, -700 mV, or -750mV vs. Ag/AgCl. The top ten most significant features identified by this analysis for experiments at -300 mV and -600 mV are shown in tables 8 and 9.

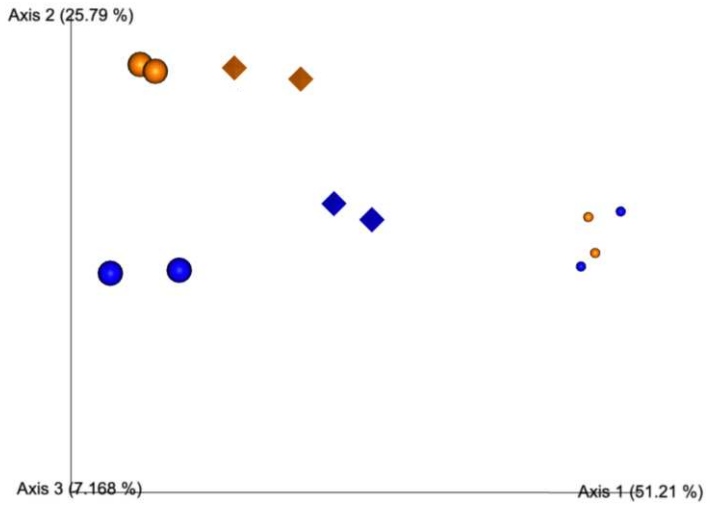

Figure 56: Principal coordinate analysis of weighted Unifrac distances for samples from -300 mV (blue) and unbiased control (orange) reactors at inoculation (small spheres) and on day 12 (large spheres). Diamonds represent biofilm pellet samples.

120

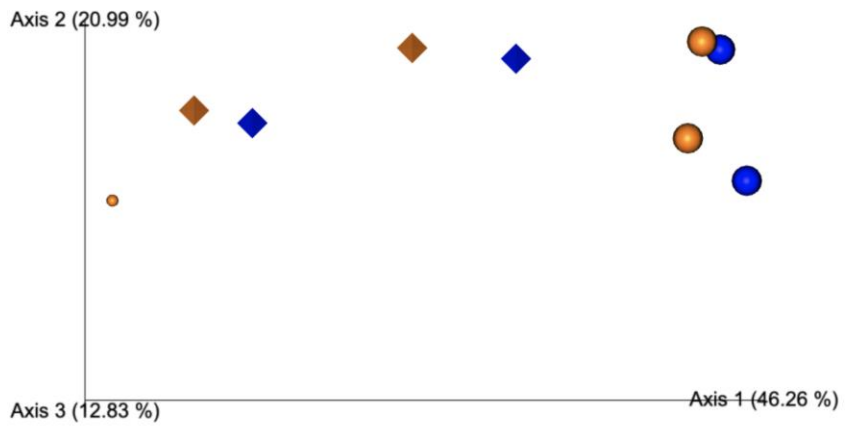

Figure 57: Principal coordinate analysis of weighted Unifrac distances for samples from -500 mV (blue) and unbiased control (orange) reactors at inoculation (small spheres) and on day 12 (large spheres). Diamonds represent biofilm pellet samples.

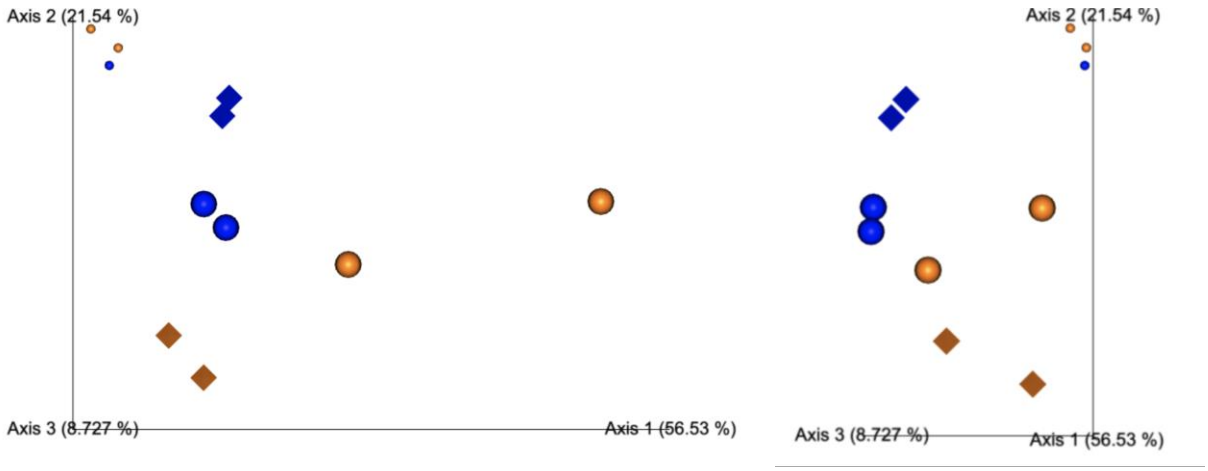

Figure 58: Principal coordinate analysis of weighted Unifrac distances for samples from -600 mV (blue) and unbiased control (orange) reactors at inoculation (small spheres) and on day 12 (large spheres). Diamonds represent biofilm pellet samples.

121

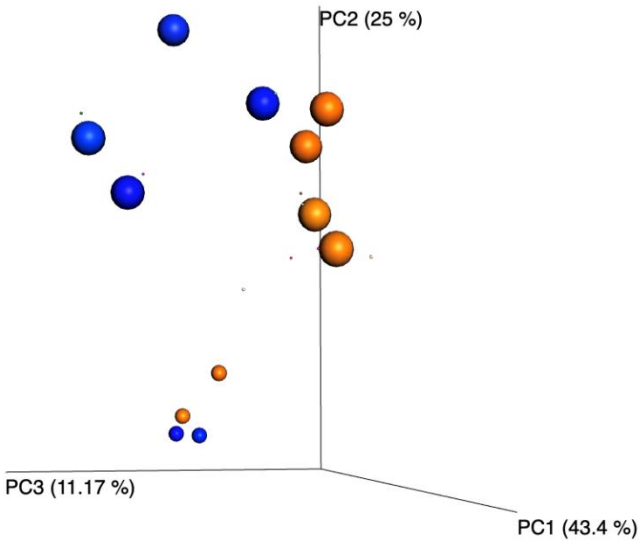

Figure 59: Principal coordinate analysis of weighted Unifrac distances for samples from -700 and -750 mV (blue) and unbiased control (orange) reactors at inoculation (small spheres) and on day 12 (large spheres).

122

Table 8: Top ten most significant features associated with treatment (biased vs. control) in experiment at -300 mV vs. Ag/AgCl. Coefficients are relative to control.

Phylum	Class	Order	Family	Genus	Species	Coeff.	P value
Firmicutes	Clostridia	Peptostreptococcales	Peptostreptococcaceae	Terrisporobacter		-2.03	1.4E-07
Firmicutes	Clostridia	Peptostreptococcales	Anaerovoracaceae	Eubacterium	nodatum	-2.37	3.5E-05
Campilobacterota	Campylobacteria	Campylobacterales	Arcobacteraceae			-3.70	9.1E-05
Proteobacteria	Gammaproteobacteria	Burkholderiales	Rhodocyclaceae	Azospira		-2.28	6.0E-04
Firmicutes	Clostridia	Oscillospirales	Ruminococcaceae			-1.59	6.9E-04
Bacteroidota	Bacteroidia	Bacteroidales	Bacteroidaceae	Bacteroides	iron reducing bacterium	-1.51	1.3E-03
Bacteroidota	Bacteroidia	Sphingobacteriales	ST-12K33	ST-12K33		2.73	2.6E-03
Campilobacterota	Campylobacteria	Campylobacterales	Sulfurospirillaceae	Sulfurospirillum	deleyianum	-2.16	2.3E-03
Firmicutes	Syntrophomonadia	Syntrophomonadales	Syntrophomonadaceae			1.78	3.1E-03
Bacteroidota	Bacteroidia	Bacteroidales	Rikenellaceae	Alistipes		2.61	5.1E-03

Table 9: Top ten most significant features associated with treatment (biased vs. control) in experiment at -600 mV vs. Ag/AgCl.

Phylum	Class	Order	Family	Genus	Species	Coeff.	P value
Desulfobacterota	Desulfovibrionia	Desulfovibrionales	Desulfovibrionaceae	Desulfovibrio		1.56	1.1E-05
Firmicutes	Clostridia	Lachnospirales	Lachnospiraceae	Lachnospiraceae NK4A13		-2.37	2.1E-05
Firmicutes	Clostridia	Peptostreptococcales	Peptostreptococcaceae	Acetoanaerobium		2.21	6.3E-05
Bacteroidota	Bacteroidia	Bacteroidales	Rikenellaceae	Anaerocella		-5.04	1.4E-04

Firmicutes	Clostridia	Oscillospirales	Oscillospiraceae	Colidextribacter		-1.49	1.7E-04
Firmicutes	Clostridia	Clostridiales	Clostridiaceae	Clostridium	butyricum	-1.90	6.1E-04
Campilobacterota	Campylobacteria	Campylobacterales	Arcobacteraceae			-3.63	1.2E-03
Euryarchaeota	Methanobacteria	Methanobacteriales	Methanobacteriaceae	Methanosphaera		-2.20	1.2E-03
Firmicutes	Clostridia	Eubacteriales	Eubacteriaceae			-2.26	1.2E-03
Proteobacteria	Gammaproteobacteria	Enterobacterales	Enterobacteriaceae			-2.63	5.2E-03

124

5.4 Discussion

5.4.1 Oxidation-reduction potential in AD

The oxidation-reduction potential (ORP) of a solution is a measurement of overall electron transfer in solution. It is an open circuit potential (OCP), in that it represents the potential measured between an electrode and a reference, with no external voltage applied. ORP is known to play an important role in bioprocesses such as anaerobic digestion and fermentation, as it corresponds to the net balance of reducing equivalents involved in metabolic processes[139].

The ORP of an anaerobic digestion system depends heavily on oxygen concentration, substrate, inoculum, pH, and biofilm development. The ORP of an AD system without an electrochemical bias can be measured as the OCP or using a redox probe. OCP was measured at the beginning and end of select experiments, with the initial OCP ranging from +100 to +300mV vs. Ag/AgCl, and the final OCP between -560 and -520 mV vs. Ag/AgCl. OCP of unbiased reactors was not measured continuously during experiments due to instrument limitations. However, in future experiments, OCP of unbiased controls should be monitored continuously.

Figure 60 shows the ORP measured with a redox probe in a conventional 2L batch anaerobic digestion using a high starch mock food waste, inoculated with UASB granules, and operated at 35°C and pH 5. The ORP of this system cannot be used quantitatively here due to differences in reactor conditions (pH, inoculum, substrate) as well as data acquisition. OCP in the H-cell reactors used in this study is measured between the bioelectrode and reference electrode, whereas a redox probe measures only the ORP of solution. Despite these differences, we can obtain valuable information from the redox behavior of traditional AD systems.

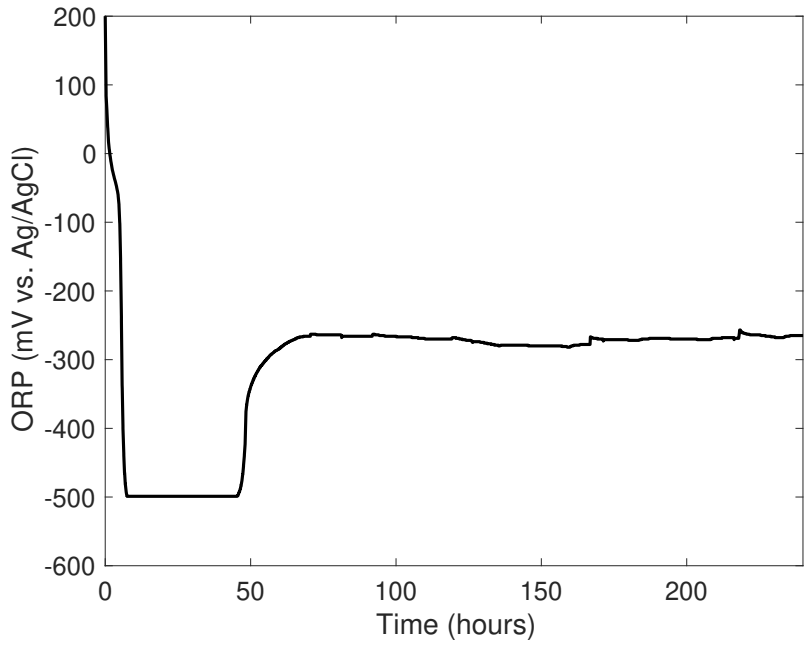

Figure 60: Measured ORP for a batch anaerobic digestion of high starch food waste inoculated with UASB granules and operated at 35°C and pH 5. Acknowledgement: Shyanne Lambrecht, South Dakota School of Mines

The initial ORP is high, as small amounts of dissolved oxygen remain in solution and metabolic activity has not yet begun. The ORP quickly drops as residual oxygen is consumed and hydrolysis begins. The plateau at -500mV is believed to result from the metabolism of soluble substrates. At 50 hours, the ORP quickly increases to -300mV, corresponding to a sharp decrease in VFA concentration, likely indicative of the onset of methanogenesis.

Based on our periodic OCP measurements, electrochemical data, and continuous ORP measurements provided by our collaborators, we can consider theoretical OCP for an unbiased control reactor (Figure 61). Theoretical OCP is plotted with the five electrochemical potentials investigated in this work to help us consider the effect that each applied potential may have in the context of ORP.

126

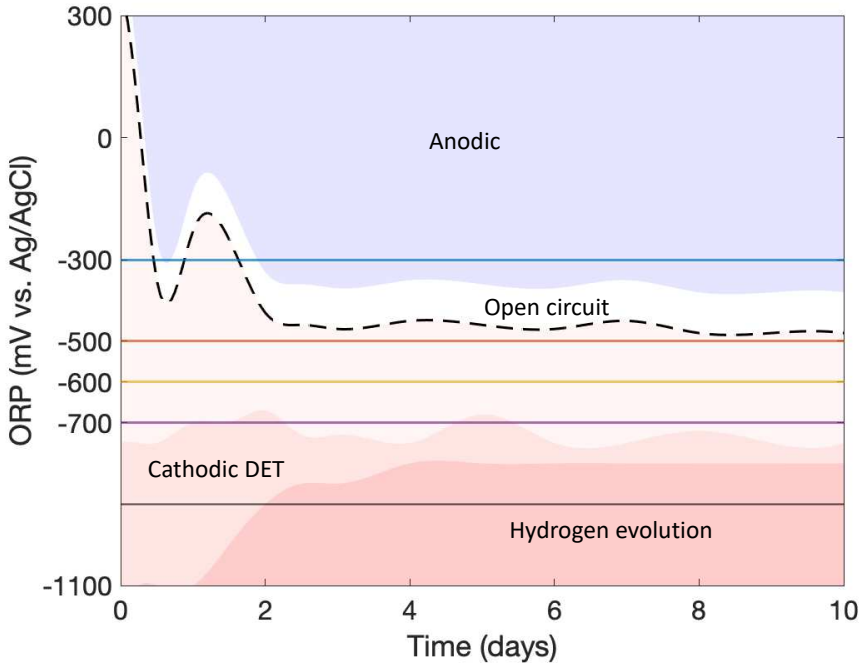

Figure 61: Theoretical OCP of an unbiased reactor (black dotted line) compared to the five applied potentials tested. The blue shaded area represents the working electrode acting as an anode, and the red shaded regions represent the WE acting as a cathode. The unshaded region corresponds to open circuit conditions. The four bioelectrochemical regimes defined in this work are identified in the figure.

The complexity of this analysis lies in the fact that the ORP of an anaerobic digestion is not constant and depends on many factors, so a constant applied potential may pass through several *bioelectrochemical regimes* over time. Further, the ORP, and therefore the boundaries of these regimes, can fluctuate from one experiment to the next due to the heterogeneity of AD and unavoidable variability of feedstock and inoculum.

When the applied potential is lower than OCP, the WE acts as a cathode, and when the applied potential is above OCP, the WE acts as an anode. In applied potentials near OCP, no current generation or consumption is observed. Because the OCP represents the largest potential with no current flow in the absence of an applied voltage, we define the OCP as the lower limit of the *OCP regime*. The *anodic regime* defines the upper limit of the OCP regime. Potentials

127

lower than OCP are reductive and can be further divided into the *cathodic DET* and *cathodic MET regimes*.

We define the cathodic DET regime as the range of applied potentials that facilitate "direct" electron transfer between microbes and the electrode, via the EET mechanisms discussed in chapter 3. In other words, in this range of potentials, the electrode serves as an electron donor for cellular metabolism. The cathodic MET regime is characterized by the onset of hydrogen evolution from water electrolysis. While DET may also occur in this region, it is not possible to distinguish the effects of DET from hydrogen-mediated electron transfer in this regime. The establishment of a biofilm decreases the overpotential for hydrogen evolution, causing the background limit for these systems to shorten over time. Figure 62 shows a wide background scan at time 0, where no biofilm has formed. Here, hydrogen evolution begins at approximately -1300 mV vs. Ag/AgCl. In contrast, the same scan was performed on the reactor after 10 days, and hydrogen evolution can be seen at -800mV vs. Ag/AgCl.

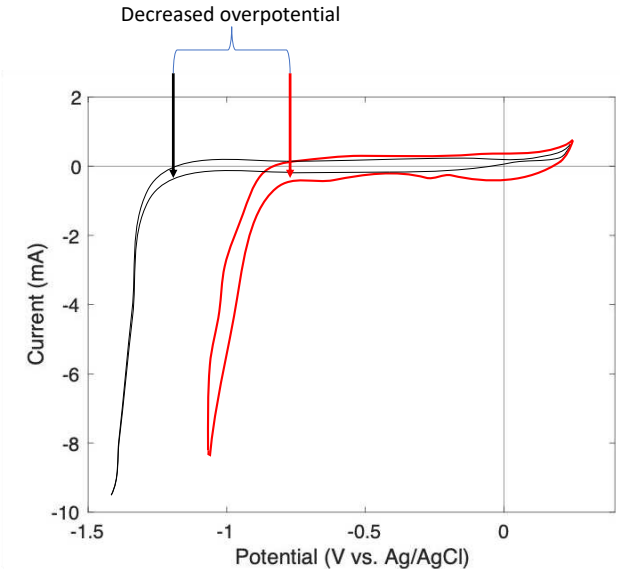

Figure 62: Cyclic voltammograms (5 mV/s) of a bare carbon felt electrode (black trace) and a developed bioelectrode (red trace) in an electro-AD reactor, demonstrating the decreased

128

overpotential for hydrogen evolution caused by electrode biofilms. Arrows indicate approximate onset of hydrogen evolution.

5.4.2 Applied potential affects product profile and microbial community structure

Statistical analyses of 16s sequencing data shows that applied potential has a statistically significant effect on microbial community structure. Beta diversity and MaAsLin analyses illustrate these effects. At -300 mV vs. Ag/AgCl, an electrode respiring biofilm is established. The establishment of an electroactive biofilm can be observed in electrochemical data and was confirmed by sequencing both planktonic and biofilm pellets from biased and control reactors. Electrode respiring species augmented by a -300 mV bias are discussed in section 5.4.3.1. at -500 mV vs. Ag/AgCl applied potential has little to no effect on microbial community structure, and no significant features were identified in MaAsLin analysis. This supports the hypothesis that an applied potential in the OCP regime will have no effect on AD processes. At -600 mV, where the most significant effects on VFA profile were observed, the effect of applied potential is confirmed by 16s data. MaAsLin analysis identified 35 significant features, many of which are fermentative bacteria such as Clostridia. Only one of the top ten most significantly associated taxa was found to be a putative DMRB, while no evidence was found in the literature for electroactivity of the remaining 9 most significant features. This finding supports the hypothesis that changes observed at -600 mV vs. Ag/AgCl are primarily the result of redox control rather than DET.

5.4.3 Influence of redox control

Reductive redox control may hinder hydrolysis. In the beginning of AD experiments, OCP is typically between 0 and +300 mV vs. Ag/AgCl, meaning that all applied potentials investigated

129

here promoted reduction in the early phases of each experiment. During this time, the dominant process occurring is hydrolysis of complex biomolecules to simple sugars. Because hydrolytic processes are oxidative, reducing potentials may hinder hydrolysis. This effect is demonstrated by observed delays in biased reactors reaching maximum VFA concentrations. These initial delays correspond with small cathodic currents. Sequencing results further support the hypothesis that oxidative conditions support hydrolytic activity. Among the top ten significant associations between -300mV applied potential and controls identified using MaAsLin analysis, two taxa, *Ruminococcaceae* and *Eubacterium nodatum,* are hydrolytic bacteria.

In contrast, cathodic potentials may accelerate acidogenesis/fermentative pathways. With an applied potential of -600 mV vs. Ag/AgCl, no delay in VFA production was observed. While this applied potential may slow hydrolysis of complex molecules, it may also accelerate the conversion of fermentable substrates to acids. At -700 and -750 mV vs. Ag/AgCl, it is likely that both redox control and direct microbe-electrode interaction begin to play a role in AD processes, where favorable redox conditions for fermentative pathways lead to chain elongation and production of C5 and C6 acids[140.]

Anodic potentials may inhibit methanogenesis. At an applied potential of -300 mV vs. Ag/AgCl, the applied bias becomes oxidative as OCP drops. Effects of methanogenesis can be observed on day 2 in the control reactor, but these effects are not observed until day 4 in the biased system. In the context of redox control, this could indicate that anodic potentials may slow the consumption of VFAs in methanogenesis. Inhibition of methanogenesis at oxidizing potentials has been reported in the literature, and it has been hypothesized that activity of hydrogenase enzymes required for methanogenesis improves at significantly lower ORPs[159]. Ultimately, methanogenesis was not inhibited entirely, and total VFA concentrations in both

130

biased and control reactors dropped below 1g/L by day 10. Direct electrode respiration also occurred at -300mV, and the role of this direct electrode interaction will be discussed in section 5.4.3.

5.4.4 Direct Microbe-Electrode Interactions

Applied potential may also influence anaerobic digestion through direct microbe-electrode interactions. Direct electron transfer is shown clearly at an applied potential of -300mV vs. Ag/AgCl, where large currents are produced, and a catalytic wave indicative of direct electrode respiration is observed in CV. Evidence of direct microbe-electrode interaction is also provided by changes in electrode biofilm microbial communities.

5.4.3.1 Anodic electrode respiration

When oxidating potentials are applied in electro-enhanced AD, an anode-respiring biofilm develops within a few days. Direct electrode respiration can be monitored through CA as a positive current. In electro-enhanced AD experiments at -300 mV vs. Ag/AgCl, an oxidative current of 4.5 mA was measured by day 4. 16s sequencing confirmed the presence of known DRMB as well as significant augmentation of putative electrode respiring species.

When direct electrode respiration was observed, the impact on VFA production was not significant during a twelve-day experiment. However, biogas compositions showed decreased methanogenesis and increased production of CO_2. Previous studies have concluded that oxidative potentials lead to inhibition of methanogenesis[159]. We observed that total VFA concentration decreased by 74% in biased reactors and 77% in controls, with almost all acetate being consumed. This decrease was accompanied by an increase in gas production, usually indicative of methanogenesis. However, while the typical gas composition is 70-80% methane and 15-20%

131

CO_2, biased reactors at -300 mV produced biogas with 37% CO_2. One possible explanation for decreased methanogenesis accompanied by consumption of acetate is that electrode respiring bacteria may outcompete methanogens due to the metabolic advantage provided by an external electron acceptor. Electrode respiring bacteria, such as *Geobacter* and *Shewanella* species, utilize acetate as a carbon source and H_2 as an electron donor, as do hydrogenotrophic methanogens (figure 63)[94,160].

Many of the species identified as significant associations when comparing -300 mV vs. Ag/AgCl reactors with their respective controls are known or putative electroactive bacteria. Known electrode-respiring bacterium *Geobacter sulfurreducens*, for example, was found to be augmented in biased reactors. Among the top he top ten associations shown in Table 8, five of the identified taxa have been shown to possess alternative respiratory capabilities, including DET. Li et al.[161] hypothesized that *Terrisporobacter* sp. May be electroactive due to the correlation between generated electricity and *Terrisporobacter* abundances in soil MFCs. *Arcobacteraceae* are capable of dissimilatory manganese reduction[162], while *Azospira* are capable of dissimilatory perchlorate reduction[163], and Sulfurospirillum posses unique electron transfer capabilities through sulfur cycling[164]. *Bacteriodes iron reducing bacterium,* named for its dissimilatory iron reducing respiration, was also augmented at -300 mV.

132

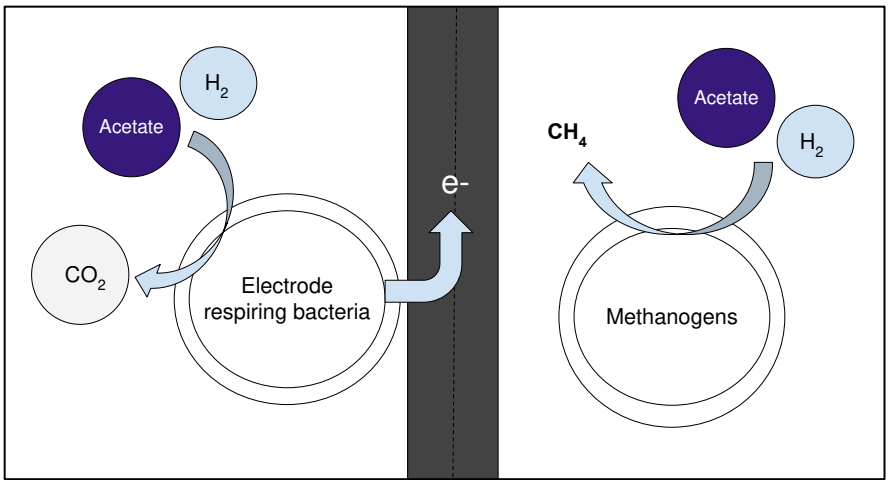

Figure 63: electrode Respiring bacteria consume H_2 and acetate to produce CO_2, while hydrogenotrophic methanogens consume acetate and H_2 to produce CH_4.

5.4.3.3 Cathodic DET

Changes in electron transfer behavior and current consumption at -700 and -750mV vs. Ag/AgCl suggest that cathodic DET may have occurred. At –750 mV, total VFA concentration decreased significantly, but C5-C7 acids were produced. Figure 64 shows the distribution of VFAs in the control reactor compared to biased reactors at -700 and -750mV vs, Ag/AgCl. Typically, decreasing VFA concentrations are accompanied by methanogenesis. However, only 5.2mL of methane was measured in the reactor at -750 mV vs. Ag/AgCl, and no CO_2 was detected. Fermentation of acetate to alcohols would be accompanied by CO_2 production, but gas fermenting bacteria consume CO_2 to perform chain elongation. It is possible that cathodic potentials benefit chain-elongation either through redox control or direct electron transfer.

Cyclic voltammograms of biased reactors at -700 and -750 mV vs. Ag/AgCl showed changes in electron transfer behavior that suggest an electroactive biofilm community may have been established. The peak that developed in biased reactors may correspond to a secreted redox mediator. Figure 65 shows a cyclic voltammogram of the biased reactor at -750 mV vs. Ag/AgCl

133

overlayed with a cyclic voltammogram of riboflavin, which is known to be secreted by electroactive species to facilitate electron transfer. Despite this evidence of direct electron transfer, no significant associations were found between applied potential and microbial community structure in this experiment. However, analysis of beta diversity shows clustering of control and biased samples, suggesting that these applied potentials did influence microbial communities. The lack of significant associations may result from -700 mV and -750 mV being combined for MaAsLin analysis. These experiments need to be repeated with biological replicates to determine the effect of these applied potentials on microbial community structure and direct electron transfer.

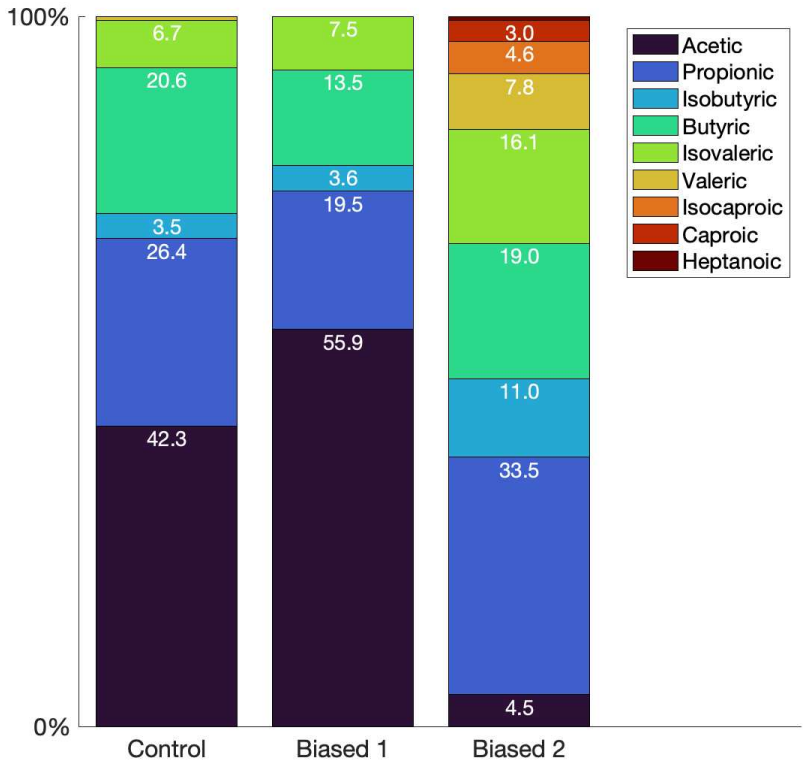

Figure 64: Distribution of VFAs in an unbiased control and biased reactors at -750 mV and -75 mV vs. Ag/AgCl. Values shown are percent of total VFAs.

134

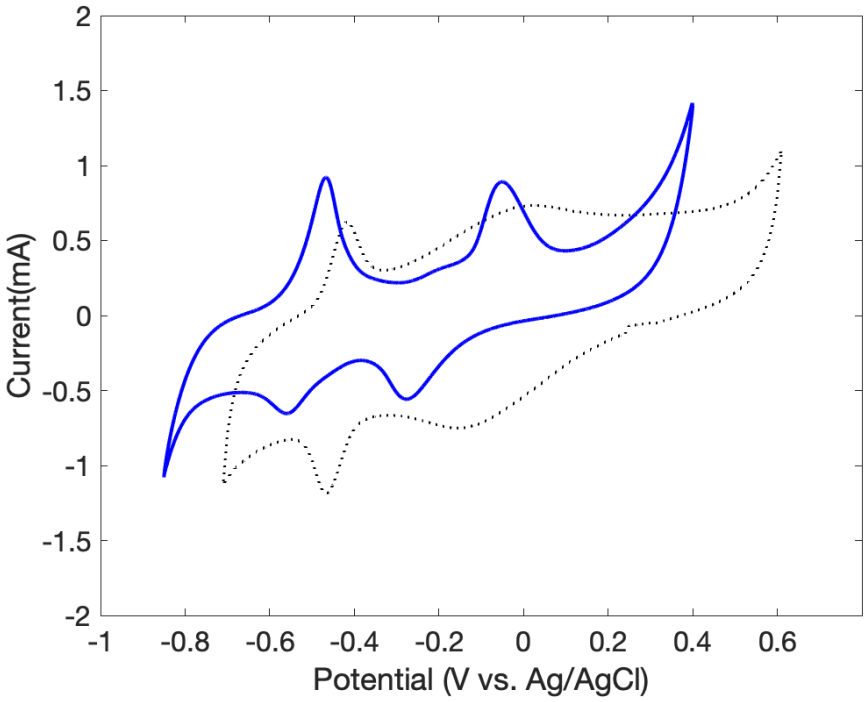

Figure 65: Cyclic voltammograms of biased (-750 mV vs. Ag/AgCl) AD biofilm (blue trace) and riboflavin in growth medium.

5.5 Conclusions and Future Directions

Electro-enhancement may provide a method of increased product selectivity in anaerobic digestion. The ability to rapidly change the ORP of an anaerobic digestion could allow fine-tuning of product profiles. However, further investigation is necessary to understand how applied potential can be implemented to improved AD.

Additional conditions should be investigated, such as potentials within the cathodic mediated electron transfer regime. While mediated electron transfer lies beyond the scope of this work, hydrogen evolution at the electrode is likely to alter AD processes significantly. Additionally, the effect of pH on electro-enhanced AD should be explored. Lower pH has been found to improve butyric acid production, while higher pH has been shown to increase total VFA concentration. Furthermore, in preliminary experiments, it was observed that an applied potential

135

of -500mV vs. Ag/AgCl had a significant effect on biofilm electrochemistry and VFA profile. Because ORP is pH dependent, the effect of applied potential is also pH dependent.

In future experiments, the ORP of control reactors should be monitored as the OCP between the bioelectrode and reference. While we can propose a theoretical ORP based on observed electrochemical behavior, measurements of actual ORP are necessary to identify boundaries of anodic and cathodic regimes over the course of a digestion. Because AD processes depend on and respond to changes in ORP, it may be beneficial to vary applied potential over the course of a digestion. For example, oxidative potentials may be beneficial for increased hydrolysis, while reducing potentials may benefit fermentative stages of AD.

Another important consideration for future experiments is the timescale of biofilm development and anaerobic digestion. It may be beneficial to perform acclimations with an applied bias to promote development of a particular electrode biofilm microbial community.

CHAPTER 6: CONCLUSIONS AND FUTURE DIRECTIONS

6.1 Significance and contributions of work

The field of BES research has existed for decades yet has remained relatively stagnant due to major challenges in the design and analysis of these systems. Successful study of BES requires interdisciplinary knowledge of microbial metabolism, bioprocess engineering, and electrochemistry. Failure to tackle challenges in BES from each of these perspectives simultaneously has led to inconsistent and erroneous studies as well as a lack of standardized approaches for studying electrode-microbe interactions. The present work attempts to reconcile these approaches by applying understanding of electrochemistry to the design of BES reactors and experiments and by combining electrochemical analysis with metabolomic and taxonomic or

136

other omic analyses. Chapter 3 describes in depth the limitations of previous work in BES research and details contributions to the field. Chapters 4 and 5 applied the methods developed in Chapter 3 to pure and mixed culture electro-enhanced processes.

6.2 Future directions and concluding remarks

The present work aimed to explore mechanisms of cathodic EET and electron utilization. However, applying proper bioelectrochemical techniques to electro-enhanxed systems, it is evident that cathodic EET is significantly less favorable and more complex than anodic EET. Other studies have also suggested that, in anaerobic conditions, it is more difficult to obtain electron-accepting biofilms on cathodes than it is to produce electrode respiring biofilms on anodes[165]. This finding is illustrated clearly by the rapid, obvious, and reproducible establishment of electro-respiring biofilms in electro-enhanced AD experiments at -300 mV vs. Ag/AgCl. Many preliminary experiments (not presented in this document) were performed at several applied potentials under varying conditions. In all cases, at -300 mV vs Ag/AgCl, direct electrode respiration and catalytic electron transfer behavior were observed. In contrast, at reducing potentials, direct electron transfer cannot be clearly discerned, and reproducibility is a major challenge. The dominance of anodic DET can be explained by its evolutionary role.

DMRB found in marine sediments have evolved mineral respiratory capabilities, which confer an adaptational advantage and play an important biogeochemical role in these environments[94,97]. Diverse bacteria in other environments, such as the digestive tracts of animals, have evolved flavin-based EET mechanisms as anaerobic respiratory capabilities. Anodic EET is primarily found in nutrient-rich environments where it is the lack of a highly oxidized terminal electron acceptor, not a lack of electron-rich substrate that creates metabolic limitations[166]. In

137

contrast, cathodic EET is less likely to occur in natural environments and does not facilitate alternative respiratory pathways. Therefore, it makes sense that mechanisms for cathodic EET have not evolved as ubiquitously as those for anodic EET.

Cathodic EET does occur naturally in iron oxidizing aerobic bacteria[167]. Despite the energetic disadvantages of iron oxidation, bacteria have evolved to utilize naturally occurring redox boundaries characterized by fluxes of iron from anoxic sources and oxygen from oxygenated water in environments such as wetlands and the rhizosphere[167]. It has been shown that, like DMRB, iron oxidizing bacteria are also able to utilize electrodes, and that electrochemical techniques can be used to observe and quantify this transfer[166]. The existence of Iron oxidizing bacteria in the environment provides evidence for cathodic DET, but also shows that cathodic transfer may not provide any advantage in anaerobic metabolism and application for the production of organic products may be limited. Furthermore, there are greater challenges in the study of cathodic transfer than anodic systems.

Cathodic EET, including iron oxidation, requires low redox potentials to drive electron transfer [166], which together with the catalysis of hydrogen evolution by biofilms, makes isolation of cathodic DET from hydrogen evolution and utilization extremely difficult. Low level sustained current consumption is difficult to discern from charging and background currents. Even if definitive boundaries exist between the DET and hydrogen evolution regimes exist in any given system, they may be impossible to discern.

While this work was unable to provide definitive proof of cathodic DET, additional conditions and techniques need to be explored. One technique that has been shown to induce cathodic EET is electro-inversion[168], where anodic potentials are first applied to encourage establishment of electrode-respiring biofilms, then cathodic potentials are applied to developed

138

bioanodes, reversing the direction of electron flow. Electro-inversion encourages the development of electroactive biofilms by inducing EET mechanisms used by electrode respiring bacteria, then utilizes these same mechanisms in reverse to enable direct electron uptake from a cathode. In addition to techniques for inducing EET, alternative conditions need to be considered. For example, studies of iron oxidizing bacteria show that the establishment of electrode-oxidizing biofilms may take significantly longer than the establishment of electrode-reducing biofilms by DMRB[166]. Acclimations and serial dilutions over extended periods of time may be required to induce transfer mechanisms and develop quantifiable sustained current consumption. Finally, growth conditions such as pH, substrate, and iron availability need to be considered.

REFERENCES

1. *Executive summary – World Energy Outlook 2022 – Analysis - IEA*. https://www.iea.org/reports/world-energy-outlook-2022/executive-summary (2022).
2. Razza, F. & Innocenti, F. D. Bioplastics from renewable resources: the benefits of biodegradability. *Asia-Pacific Journal of Chemical Engineering* **7**, S301–S309 (2012).
3. Emadian, S. M., Onay, T. T. & Demirel, B. Biodegradation of bioplastics in natural environments. *Waste Management* **59**, 526–536 (2017).
4. Tokiwa, Y., Calabia, B., Ugwu, C. & Aiba, S. Biodegradability of Plastics. *Int J Mol Sci* **10**, 3722–3742 (2009).
5. US EPA, OA,OEAEE, O. New Oxygenated Fuels Program. https://www.epa.gov/archive/epa/aboutepa/new-oxygenated-fuels-program.html#:~:text=The%20oxygenated%20fuels%20program%20is,carbon%20monoxide%20air%20quality%20standard.
6. Liu, Y. *et al.* Leading Edge Biofuels for a sustainable future. *Cell* **184**, 1636–1647 (2021).
7. USDA ERS - Feed Grains Sector at a Glance. https://www.ers.usda.gov/topics/crops/corn-and-other-feed-grains/feed-grains-sector-at-a-glance/.
8. Martin, M. A. First generation biofuels compete. *N Biotechnol* **27**, 596–608 (2010).
9. Naik, S. N., Goud, V. V., Rout, P. K. & Dalai, A. K. Production of first and second generation biofuels: A comprehensive review. *Renewable and Sustainable Energy Reviews* **14**, 578–597 (2010).

10. Zoghlami, A. & Paës, G. Lignocellulosic Biomass: Understanding Recalcitrance and Predicting Hydrolysis. *Front Chem* **7**, 874 (2019).
11. Zelikoff, J. T. *et al.* Effects of Inhaled Ambient Particulate Matter on Pulmonary Antimicrobial Immune Defense. *Inhal Toxicol* **15**, 131–150 (2003).
12. Polichetti, G., Cocco, S., Spinali, A., Trimarco, V. & Nunziata, A. Effects of particulate matter (PM10, PM2.5 and PM1) on the cardiovascular system. *Toxicology* **261**, 1–8 (2009).
13. Watkinson, W. P., Campen, M. J., Nolan, J. P. & Costa, D. L. Cardiovascular and systemic responses to inhaled pollutants in rodents: effects of ozone and particulate matter. *Environ Health Perspect* **109**, 539–546 (2001).
14. Afshin, A. *et al.* Health effects of dietary risks in 195 countries, 1990–2017: a systematic analysis for the Global Burden of Disease Study 2017. *The Lancet* **393**, 1958–1972 (2019).
15. Burnett, R. *et al.* Global estimates of mortality associated with long-term exposure to outdoor fine particulate matter. *Proceedings of the National Academy of Sciences* **115**, 9592–9597 (2018).
16. Amin, F. R. *et al.* Pretreatment methods of lignocellulosic biomass for anaerobic digestion. *AMB Express* **7**, 72 (2017).
17. Zhou, M. & Tian, X. Development of different pretreatments and related technologies for efficient biomass conversion of lignocellulose. *Int J Biol Macromol* **202**, 256–268 (2022).
18. Naber, J. D. & Johnson, J. E. Internal combustion engine cycles and concepts. in *Alternative Fuels and Advanced Vehicle Technologies for Improved Environmental Performance* 197–224 (Woodhead Publishing, 2014). doi:10.1533/9780857097422.2.197.
19. Jacobson, M. Z. Short-term effects of controlling fossil-fuel soot, biofuel soot and gases, and methane on climate, Arctic ice, and air pollution health. *J Geophys Res* **115**, D14209 (2010).
20. Bond, T. C. *et al.* Bounding the role of black carbon in the climate system: A scientific assessment. *Journal of Geophysical Research: Atmospheres* **118**, 5380–5552 (2013).
21. Ren, Y. *et al.* Combustion and emissions of a DI diesel engine fuelled with diesel-oxygenate blends. (2008) doi:10.1016/j.fuel.2008.02.017.
22. Charles K. Westbrook, William J. Pitz, A. & Curran, H. J. Chemical Kinetic Modeling Study of the Effects of Oxygenated Hydrocarbons on Soot Emissions from Diesel Engines†. (2006) doi:10.1021/JP056362G.
23. Vijayashree, P. & Ganesan, V. Oxygenated Fuel Additive Option for PM Emission Reduction from Diesel Engines—A Review. in 141–163 (Springer, Singapore, 2019). doi:10.1007/978-981-13-3299-9_7.
24. Hansen, A. C., Zhang, Q. & Lyne, P. W. L. Ethanol–diesel fuel blends — a review. *Bioresour Technol* **96**, 277–285 (2005).
25. Arcoumanis, C., Bae, C., Crookes, R. & Kinoshita, E. The potential of di-methyl ether (DME) as an alternative fuel for compression-ignition engines: A review. *Fuel* **87**, 1014–1030 (2008).
26. McEnally, C. S. & Pfefferle, L. D. The effects of dimethyl ether and ethanol on benzene and soot formation in ethylene nonpremixed flames. *Proceedings of the Combustion Institute* **31**, 603–610 (2007).

27. Burke, S. C., Ratcliff, M., McCormick, R., Rhoads, R. & Windom, B. Distillation-based Droplet Modeling of Non-Ideal Oxygenated Gasoline Blends: Investigating the Role of Droplet Evaporation on PM Emissions. *SAE Int J Fuels Lubr* **10**, 2017-01–0581 (2017).
28. Miyamoto, N., Ogawa, H., Nurun, N. Md., Obata, K. & Arima, T. Smokeless, Low NOx, High Thermal Efficiency, and Low Noise Diesel Combustion with Oxygenated Agents as Main Fuel on JSTOR. *SAE Transactions* **107**, 171–177 (1998).
29. McEnally, C. S. & Pfefferle, L. D. Sooting Tendencies of Oxygenated Hydrocarbons in Laboratory-Scale Flames. *Environ Sci Technol* **45**, 2498–2503 (2011).
30. He, B.-Q., Shuai, S.-J., Wang, J.-X. & He, H. The effect of ethanol blended diesel fuels on emissions from a diesel engine. *Atmos Environ* **37**, 4965–4971 (2003).
31. Paul J. Squillace, John S. Zogorski, William G. Wilber, A. & Price, C. V. Preliminary Assessment of the Occurrence and Possible Sources of MTBE in Groundwater in the United States, 1993−1994. (1996) doi:10.1021/ES9507170.
32. US EPA. Overview | Methyl Tertiary Butyl Ether (MTBE) | US EPA. https://archive.epa.gov/mtbe/web/html/faq.html (2016).
33. Sun, R., Delidovich, I. & Palkovits, R. Dimethoxymethane as a Cleaner Synthetic Fuel: Synthetic Methods, Catalysts, and Reaction Mechanism. (2019) doi:10.1021/acscatal.8b04441.
34. Burger, J., Siegert, M., Ströfer, E. & Hasse, H. Poly(oxymethylene) dimethyl ethers as components of tailored diesel fuel: Properties, synthesis and purification concepts. *Fuel* **89**, 3315–3319 (2010).
35. Ouda, M. *et al.* Poly(oxymethylene) dimethyl ether synthesis – a combined chemical equilibrium investigation towards an increasingly efficient and potentially sustainable synthetic route. *React Chem Eng* **2**, 50–59 (2017).
36. Schmitz, N., Homberg, F., Berje, J., Burger, J. & Hasse, H. Chemical equilibrium of the synthesis of poly (oxymethylene) dimethyl ethers from formaldehyde and methanol in aqueous solutions. *Ind Eng Chem Res* **54**, 6409–6417 (2015).
37. Zhao, Y., Xu, Z., Chen, H., Fu, Y. & Shen, J. Mechanism of chain propagation for the synthesis of polyoxymethylene dimethyl ethers. *Journal of Energy Chemistry* **22**, 833–836 (2013).
38. Lautenschütz, L. *et al.* Physico-chemical properties and fuel characteristics of oxymethylene dialkyl ethers. *Fuel* **173**, 129–137 (2016).
39. Gao, X.-J. *et al.* Synthesis of Polyoxymethylene Dimethyl Ethers from Dimethyl Ether Direct Oxidation over Carbon-Based Catalysts. *ChemCatChem* **10**, 273–279 (2018).
40. Keil, F. J. Methanol-to-hydrocarbons: process technology. *Microporous and Mesoporous Materials* **29**, 49–66 (1999).
41. Stöcker, M. Methanol-to-hydrocarbons: catalytic materials and their behavior. *Microporous and Mesoporous Materials* **29**, 3–48 (1999).
42. Holmgren, K. M., Andersson, E., Berntsson, T. & Rydberg, T. Gasification-based methanol production from biomass in industrial clusters: Characterisation of energy balances and greenhouse gas emissions. *Energy* **69**, 622–637 (2014).
43. Feng, W., Ji, P., Chen, B. & Zheng, D. Analysis of Methanol Production from Biomass Gasification. *Chem Eng Technol* **34**, 307–317 (2011).
44. Pahima, E., Hoz, S., Ben-Tzion, M. & Major, D. T. Computational design of biofuels from terpenes and terpenoids. *Sustain Energy Fuels* **3**, 457–466 (2019).

45. ASTM International. *Standard Test Method for Smoke Point of Kerosene and Aviation Turbine Fuel*. (2019).
46. Das, D. D. *et al.* Sooting tendencies of diesel fuels, jet fuels, and their surrogates in diffusion flames. *Fuel* **197**, 445–458 (2017).
47. Dwivedi, G. & Sharma, M. P. Impact of cold flow properties of biodiesel on engine performance. *Renewable and Sustainable Energy Reviews* **31**, 650–656 (2014).
48. ASTM International. *Designation: D975 − 20a Standard Specification for Diesel Fuel 1*. (2020) doi:10.1520/D0975-20A.
49. Saldana, D. A., Starck, L., Mougin, P., Rousseau, B. & Creton, B. Prediction of Flash Points for Fuel Mixtures Using Machine Learning and a Novel Equation. *Energy & Fuels* **27**, 3811–3820 (2013).
50. US EPA. Estimation Program Interface Suite for Microsoft® Windows, v 4.11. Preprint at (2012).
51. Butler, R. M., Cooke, G. M. & Lukk, G. G. Prediction of Flash Points of Middle Distillates. *Ind Eng Chem Res* **48**, 808–812 (1956).
52. Prugh, R. W. Estimation of flash point temperature. *J Chem Educ* **50**, A85 (1973).
53. Kraetsch, E. J. *Application of Dulong's Formula in the Ultimate Analysis of Coal*. (1934).
54. Boie, W. Fuel technology calculations. *Energietechnik* **3**, 309–316 (1953).
55. Lloyd, W. G. & Davenport, D. A. Applying thermodynamics to fossil fuels: Heats of combustion from elemental compositions. *J Chem Educ* **57**, 56 (1980).
56. Mason, D. M. & Gandhi, K. Formulas for calculating the heating value of coal and coal char: development, tests, and uses. *Institute of Gas and Technology* (1980).
57. ASTM International. *Standard Test Method for Heat of Combustion of Liquid Hydrocarbon Fuels by Bomb Calorimeter 1*. (2019) doi:10.1520/D0240-19.
58. Das, D. D., St. John, P. C., McEnally, C. S., Kim, S. & Pfefferle, L. D. Measuring and predicting sooting tendencies of oxygenates, alkanes, alkenes, cycloalkanes, and aromatics on a unified scale. *Combust Flame* **190**, 349–364 (2018).
59. Dahmen, M. & Marquardt, W. A Novel Group Contribution Method for the Prediction of the Derived Cetane Number of Oxygenated Hydrocarbons. *Energy & Fuels* **29**, 5781–5801 (2015).
60. ASTM International. *Standard Test Method for Determination of Ignition Delay and Derived Cetane Number (DCN) of Diesel Fuel Oils by Combustion in a Constant Volume Chamber 1,2*. (2019) doi:10.1520/D6890-18.
61. Kessler, T., Sacia, E., Bell, A., Fuel, J. M.- & 2017, U. Artificial neural network based predictions of cetane number for furanic biofuel additives. *Fuel* **26**, 171–179 (2017).
62. St. John, P. C., Guan, Y., Kim, Y., Kim, S. & Paton, R. S. Prediction of organic homolytic bond dissociation enthalpies at near chemical accuracy with sub-second computational cost. *Nat Commun* **11**, 2328 (2020).
63. McCormick, R. L. *et al.* Selection Criteria and Screening of Potential Biomass-Derived Streams as Fuel Blendstocks for Advanced Spark-Ignition Engines. *SAE Int J Fuels Lubr* **10**, (2017).
64. Stefanis, E. & Panayiotou, C. Prediction of Hansen Solubility Parameters with a new group-contribution method. *Int J Thermophys* **29**, 568–585 (2008).
65. Batista, M. M., Guirardello, R. & Krähenbühl, M. A. Determination of the Hansen Solubility Parameters of Vegetable Oils, Biodiesel, Diesel, and Biodiesel–Diesel Blends. *J Am Oil Chem Soc* **92**, 95–109 (2015).

66. Wickey, R. & Chittenden, D. Flash Points of Blends Correlated. *Hydrocarbon Processing* **42**, 157 (1963).
67. Tesfa, B., Gu, F., Mishra, R. & Ball, A. D. LHV predication models and LHV effect on the performance of CI engine running with biodiesel blends. *Energy Convers Manag* **71**, 217–226 (2013).
68. Gülüm, M. & Bilgin, A. Density, flash point and heating value variations of corn oil biodiesel–diesel fuel blends. *Fuel Processing Technology* **134**, 456–464 (2015).
69. McEnally, C. S. *et al.* Sooting tendencies of co-optima test gasolines and their surrogates. *Proceedings of the Combustion Institute* **37**, 961–968 (2019).
70. Mueller, C. J. *et al.* Diesel Surrogate Fuels for Engine Testing and Chemical-Kinetic Modeling: Compositions and Properties. *Energy & Fuels* **30**, 1445–1461 (2016).
71. Aghahossein Shirazi, S. *et al.* Effects of dual-alcohol gasoline blends on physiochemical properties and volatility behavior. *Fuel* **252**, 542–552 (2019).
72. Chen, Z. *et al.* Study on performance and emissions of a passenger-car diesel engine fueled with butanol–diesel blends. *Energy* **55**, 638–646 (2013).
73. McEnally, C. S. & Pfefferle, L. D. Improved sooting tendency measurements for aromatic hydrocarbons and their implications for naphthalene formation pathways. *Combust Flame* **148**, 210–222 (2007).
74. McEnally, C. S., Das, D. D. & Pfefferle, L. D. Yield Sooting Index Database Volume 2: Sooting Tendencies of a Wide Range of Fuel Compounds on a Unified Scale - Pfefferle Research Group: Combustion and Nanomaterials Dataverse. *Harvard Dataverse* https://dataverse.harvard.edu/dataset.xhtml?persistentId=doi:10.7910/DVN/7HGFT8 (2017).
75. St. John, P. C. *et al.* A Quantitative Model for the Prediction of Sooting Tendency from Molecular Structure. *Energy & Fuels* **31**, 9983–9990 (2017).
76. Lide, D. R. *CRC handbook of chemistry and physics*. (2012).
77. Boyd, R. H. Some physical properties of polyoxymethylene dimethyl ethers. *Journal of Polymer Science* **50**, 133–141 (1961).
78. Marchionna, M. & Patrini, R. Patent Application EP1505049A1, European Patent Office: A process for the selective production of dialkyl-polyformals. Preprint at (2000).
79. Yang, Y., Xu, M., Guo, J. & Sun, G. Bacterial extracellular electron transfer in bioelectrochemical systems. *Process Biochemistry* **47**, 1707–1714 (2012).
80. Marsili, E. *et al.* Shewanella secretes flavins that mediate extracellular electron transfer. *Proc Natl Acad Sci U S A* **105**, 3968–73 (2008).
81. von Canstein, H., Ogawa, J., Shimizu, S. & Lloyd, J. R. Secretion of Flavins by *Shewanella* Species and Their Role in Extracellular Electron Transfer. *Appl Environ Microbiol* **74**, 615–623 (2008).
82. Reguera, G. Microbial nanowires and electroactive biofilms. *FEMS Microbiol Ecol* **94**, (2018).
83. Choi, O. & Sang, B. Extracellular electron transfer from cathode to microbes: application for biofuel production. *Biotechnol Biofuels* **9**, (2016).
84. Shi, L. *et al.* The roles of outer membrane cytochromes of Shewanella and Geobacter in extracellular electron transfer. *Environ Microbiol Rep* **1**, 220–227 (2009).
85. Shi, L., Squier, T. C., Zachara, J. M. & Fredrickson, J. K. Respiration of metal (hydr)oxides by *Shewanella* and *Geobacter* : a key role for multihaem *c* -type cytochromes. *Mol Microbiol* **65**, 12–20 (2007).

86. Bond, D. R. & Lovley, D. R. Electricity Production by Geobacter sulfurreducens Attached to Electrodes. *Appl Environ Microbiol* **69**, 1548–1555 (2003).
87. Schuetz, B., Schicklberger, M., Kuermann, J., Spormann, A. M. & Gescher, J. Periplasmic electron transfer via the c-type cytochromes MtrA and FccA of Shewanella oneidensis MR-1. *Appl Environ Microbiol* **75**, 7789–96 (2009).
88. Bond, D. R., Holmes, D. E., Tender, L. M. & Lovley, D. R. Electrode-Reducing Microorganisms That Harvest Energy from Marine Sediments. *Science (1979)* **295**, 483–485 (2002).
89. Ross, D. E., Flynn, J. M., Baron, D. B., Gralnick, J. A. & Bond, D. R. Towards Electrosynthesis in Shewanella: Energetics of Reversing the Mtr Pathway for Reductive Metabolism. *PLoS One* **6**, e16649 (2011).
90. Kim, B.-H., Kim, H.-J., Hyun, M.-S. & Park, D.-H. Direct Electrode Reaction of Fe(III)-Reducing Bacterium, Shewanella putrefaciens. *J Microbiol Biotechnol* **9**, 127–131 (1999).
91. Baron, D., Labelle, E., Coursolle, D., Gralnick, J. A. & Bond, D. R. Electrochemical Measurement of Electron Transfer Kinetics by Shewanella oneidensis MR-1 *. *J Biol Chem* **284**, 28865–28873 (2009).
92. Lovley, D. R., Stolz, J. F., Nord, G. L. & Phillips, E. J. P. Anaerobic production of magnetite by a dissimilatory iron-reducing microorganism. *Nature* **330**, 252–254 (1987).
93. Lovley, D. R. *et al.* Geobacter metallireducens gen. nov. sp. nov., a microorganism capable of coupling the complete oxidation of organic compounds to the reduction of iron and other metals. *Arch Microbiol* **159**, 336–344 (1993).
94. Lovley, D. R. DISSIMILATORY METAL REDUCTION. *Annu Rev Microbiol* **47**, 263–290 (1993).
95. Lovley, D. R., Phillips, E. J. P. & Lonergan, D. J. Hydrogen and Formate Oxidation Coupled to Dissimilatory Reduction of Iron or Manganese by *Alteromonas putrefaciens*. *Appl Environ Microbiol* **55**, 700–706 (1989).
96. Caccavo, F. *et al.* Geobacter sulfurreducens sp. nov., a hydrogen- and acetate-oxidizing dissimilatory metal-reducing microorganism. *Appl Environ Microbiol* **60**, 3752–9 (1994).
97. Lovley, D. R. Dissimilatory Fe(III) and Mn(IV) reduction. *Microbiol Rev* **55**, 259–87 (1991).
98. Reimers*, C. E., Tender*, L. M., Fertig, S. & Wang, W. Harvesting Energy from the Marine Sediment−Water Interface. (2000) doi:10.1021/ES001223S.
99. Hongo, M. & Iwahara, M. Application of Electro-energizing Method to l -Glutamic Acid Fermentation. *Agric Biol Chem* **43**, 2075–2081 (1979).
100. Hongo, M. & Iwahara, M. Determination of Electro-energizing Conditions for l -Glutamic Acid Fermentation. *Agric Biol Chem* **43**, 2083–2086 (1979).
101. Kim, T. S. & Kim, B. H. Electron flow shift inClostridium acetobutylicum fermentation by electrochemically introduced reducing equivalent. *Biotechnol Lett* **10**, 123–128 (1988).
102. Gregory, K. B., Bond, D. R. & Lovley, D. R. Graphite electrodes as electron donors for anaerobic respiration. *Environ Microbiol* **6**, 596–604 (2004).
103. Strycharz ∗, S. M. *et al.* Gene expression and deletion analysis of mechanisms for electron transfer from electrodes to Geobacter sulfurreducens. (2010) doi:10.1016/j.bioelechem.2010.07.005.
104. Firer-Sherwood, M. A., Bewley, K. D., Mock, J.-Y. & Elliott, S. J. Tools for resolving complexity in the electron transfer networks of multiheme cytochromes cwz. *Cite this: Metallomics* **3**, 344–348 (2011).

105. Mathew, A. S., Wang, J., Luo, J. & Yau, S.-T. Enhanced ethanol production via electrostatically accelerated fermentation of glucose using Saccharomyces cerevisiae. *Sci Rep* **5**, 15713 (2015).
106. Shin, H., Zeikus, J. & Jain, M. Electrically enhanced ethanol fermentation by Clostridium thermocellum and Saccharomyces cerevisiae. *Appl Microbiol Biotechnol* **58**, 476–481 (2002).
107. Choi, O., Kim, T., Woo, H. M. & Um, Y. Electricity-driven metabolic shift through direct electron uptake by electroactive heterotroph Clostridium pasteurianum. *Sci Rep* **4**, 6961 (2015).
108. Khosravanipour Mostafazadeh, A. *et al.* Enhancement of biobutanol production by electromicrobial glucose conversion in a dual chamber fermentation cell using C. pasteurianum. *Energy Convers Manag* **130**, 165–175 (2016).
109. Utesch, T. *et al.* Enhanced electron transfer of different mediators for strictly opposite shifting of metabolism in *Clostridium pasteurianum* grown on glycerol in a new electrochemical bioreactor. *Biotechnol Bioeng* **116**, 1627–1643 (2019).
110. Engel, M., Bayer, H., Holtmann, D., Tippkötter, N. & Ulber, R. Flavin secretion of Clostridium acetobutylicum in a bioelectrochemical system - Is an iron limitation involved? *Bioelectrochemistry* **129**, 242–250 (2019).
111. Engel, M. *et al. Clostridium Acetobutylicum* 's Connecting World: Cell Appendage Formation in Bioelectrochemical Systems. *ChemElectroChem* **7**, 414–420 (2020).
112. Kracke, F., Virdis, B., Bernhardt, P. V., Rabaey, K. & Krömer, J. O. Redox dependent metabolic shift in Clostridium autoethanogenum by extracellular electron supply. *Biotechnol Biofuels* **9**, 249 (2016).
113. Nevin, K. P., Woodard, T. L., Franks, A. E., Summers, Z. M. & Lovley, D. R. Microbial Electrosynthesis: Feeding Microbes Electricity To Convert Carbon Dioxide and Water to Multicarbon Extracellular Organic Compounds. *mBio* **1**, (2010).
114. Rabaey, K. & Rozendal, R. A. Microbial electrosynthesis — revisiting the electrical route for microbial production. *Nat Rev Microbiol* **8**, 706–716 (2010).
115. Gong, Z., Yu, H., Zhang, J., Li, F. & Song, H. Microbial electro-fermentation for synthesis of chemicals and biofuels driven by bi-directional extracellular electron transfer. *Synth Syst Biotechnol* **5**, 304–313 (2020).
116. Srikanth, S., Marsili, E., Flickinger, M. C. & Bond, D. R. Electrochemical characterization ofGeobacter sulfurreducens cells immobilized on graphite paper electrodes. *Biotechnol Bioeng* **99**, 1065–1073 (2008).
117. Chin, K.-J., Esteve-Núñez, A., Leang, C. & Lovley, D. R. Direct Correlation between Rates of Anaerobic Respiration and Levels of mRNA for Key Respiratory Genes in *Geobacter sulfurreducens*. *Appl Environ Microbiol* **70**, 5183–5189 (2004).
118. Khare, T. *et al.* Differential protein expression in the metal-reducing bacteriumGeobacter sulfurreducens strain PCA grown with fumarate or ferric citrate. *Proteomics* **6**, 632–640 (2006).
119. Kim, B.-C. *et al.* OmcF, a Putative *c* -Type Monoheme Outer Membrane Cytochrome Required for the Expression of Other Outer Membrane Cytochromes in *Geobacter sulfurreducens*. *J Bacteriol* **187**, 4505–4513 (2005).
120. Leang, C. *et al.* Adaptation to Disruption of the Electron Transfer Pathway for Fe(III) Reduction in *Geobacter sulfurreducens*. *J Bacteriol* **187**, 5918–5926 (2005).

121. Leang, C., Coppi, M. V. & Lovley, D. R. OmcB, a *c* -Type Polyheme Cytochrome, Involved in Fe(III) Reduction in *Geobacter sulfurreducens*. *J Bacteriol* **185**, 2096–2103 (2003).
122. Shi, L. *et al.* Isolation of a High-Affinity Functional Protein Complex between OmcA and MtrC: Two Outer Membrane Decaheme *c* -Type Cytochromes of *Shewanella oneidensis* MR-1. *J Bacteriol* **188**, 4705–4714 (2006).
123. Ross, D. E. *et al.* Characterization of Protein-Protein Interactions Involved in Iron Reduction by *Shewanella oneidensis* MR-1. *Appl Environ Microbiol* **73**, 5797–5808 (2007).
124. Xiaoting Tang *et al.* Profiling the Membrane Proteome of Shewanella oneidensis MR-1 with New Affinity Labeling Probes. (2006) doi:10.1021/PR060480E.
125. Mehta, T., Coppi, M. V., Childers, S. E. & Lovley, D. R. Outer Membrane *c* -Type Cytochromes Required for Fe(III) and Mn(IV) Oxide Reduction in *Geobacter sulfurreducens*. *Appl Environ Microbiol* **71**, 8634–8641 (2005).
126. Reguera, G. *et al.* Extracellular electron transfer via microbial nanowires. *Nature* **435**, 1098–1101 (2005).
127. Light, S. H. *et al.* A flavin-based extracellular electron transfer mechanism in diverse Gram-positive bacteria. *Nature* **562**, 140–144 (2018).
128. Elgrishi, N. N. *et al.* A Practical Beginner's Guide to Cyclic Voltammetry. (2017) doi:10.1021/acs.jchemed.7b00361.
129. Léger, C. & Bertrand, P. Direct Electrochemistry of Redox Enzymes as a Tool for Mechanistic Studies. *Chem Rev* **108**, 2379–2438 (2008).
130. Meitl, L. A. *et al.* Electrochemical interaction of Shewanella oneidensis MR-1 and its outer membrane cytochromes OmcA and MtrC with hematite electrodes. *Geochim Cosmochim Acta* **73**, 5292–5307 (2009).
131. Marsili, E., Rollefson, J. B., Baron, D. B., Hozalski, R. M. & Bond, D. R. Microbial Biofilm Voltammetry: Direct Electrochemical Characterization of Catalytic Electrode-Attached Biofilms. *Appl Environ Microbiol* **74**, 7329–7337 (2008).
132. *Pine Research Electrode Polishing Guide*. www.buehler.com (2008).
133. Melchers, R. E. Microbiological and abiotic processes in modelling longer-term marine corrosion of steel. *Bioelectrochemistry* **97**, 89–96 (2014).
134. Hu, Y., Hao, X., Zhao, D. & Fu, K. Enhancing the CH4 yield of anaerobic digestion via endogenous CO2 fixation by exogenous H2. *Chemosphere* **140**, 34–39 (2015).
135. Wei, J., Hao, X., van Loosdrecht, M. C. M. & Li, J. Feasibility analysis of anaerobic digestion of excess sludge enhanced by iron: A review. *Renewable and Sustainable Energy Reviews* **89**, 16–26 (2018).
136. Huang, Q., Liu, Y. & Ranjan Dhar, B. A multifaceted screening of applied voltages for electro-assisted anaerobic digestion of blackwater: Significance of temperature, hydrolysis/acidogenesis, electrode corrosion, and energy efficiencies. *Bioresour Technol* **360**, 127533 (2022).
137. Bartholet, D. L. *et al.* Property predictions demonstrate that structural diversity can improve the performance of polyoxymethylene ethers as potential bio-based diesel fuels. *Fuel* **295**, 120509 (2021).
138. Arellano-Treviño, M. A. *et al.* Synthesis of Butyl-Exchanged Polyoxymethylene Ethers as Renewable Diesel Blendstocks with Improved Fuel Properties. *ACS Sustain Chem Eng* **9**, 6266–6273 (2021).

139. Chen, Q., Wu, W., Qi, D., Ding, Y. & Zhao, Z. Review on microaeration-based anaerobic digestion: State of the art, challenges, and prospectives. *Science of The Total Environment* **710**, 136388 (2020).
140. Reddy, M. V., ElMekawy, A. & Pant, D. Bioelectrochemical synthesis of caproate through chain elongation as a complementary technology to anaerobic digestion. *Biofuels, Bioproducts and Biorefining* **12**, 966–977 (2018).
141. Liu, C.-G., Qin, J.-C. & Lin, Y.-H. Fermentation and Redox Potential. in *Fermentation Processes* (InTech, 2017). doi:10.5772/64640.
142. Liu, C.-G., Xue, C., Lin, Y.-H. & Bai, F.-W. Redox potential control and applications in microaerobic and anaerobic fermentations. *Biotechnol Adv* **31**, 257–265 (2013).
143. Wang, S., Zhu, Y., Zhang, Y. & Li, Y. Controlling the oxidoreduction potential of the culture of Clostridium acetobutylicum leads to an earlier initiation of solventogenesis, thus increasing solvent productivity. *Appl Microbiol Biotechnol* **93**, 1021–1030 (2012).
144. Patakova, P. *et al.* Acidogenesis, solventogenesis, metabolic stress response and life cycle changes in Clostridium beijerinckii NRRL B-598 at the transcriptomic level. *Sci Rep* **9**, 1371 (2019).
145. Wietzke, M. & Bahl, H. The redox-sensing protein Rex, a transcriptional regulator of solventogenesis in Clostridium acetobutylicum. *Appl Microbiol Biotechnol* **96**, 749–761 (2012).
146. Roy, J. N. *et al.* A study of the flavin response by Shewanella cultures in carbon-limited environments. *RSC Adv* **2**, 10020 (2012).
147. Meegoda, J., Li, B., Patel, K. & Wang, L. A Review of the Processes, Parameters, and Optimization of Anaerobic Digestion. *Int J Environ Res Public Health* **15**, 2224 (2018).
148. Kamusoko, R., Jingura, R. M., Chikwambi, Z. & Parawira, W. Biogas: microbiological research to enhance efficiency and regulation. *Handbook of Biofuels* 485–497 (2022) doi:10.1016/B978-0-12-822810-4.00025-7.
149. Zakaria, B. S. & Dhar, B. R. Progress towards catalyzing electro-methanogenesis in anaerobic digestion process: Fundamentals, process optimization, design and scale-up considerations. *Bioresour Technol* **289**, 121738 (2019).
150. Zhao, Z., Zhang, Y., Quan, X. & Zhao, H. Evaluation on direct interspecies electron transfer in anaerobic sludge digestion of microbial electrolysis cell. *Bioresour Technol* **200**, 235–244 (2016).
151. Clauwaert, P. *et al.* Combining biocatalyzed electrolysis with anaerobic digestion. *Water Science and Technology* **57**, 575–579 (2008).
152. Mostafa, A., Im, S., Song, Y.-C., Ahn, Y. & Kim, D.-H. Enhanced Anaerobic Digestion by Stimulating DIET Reaction. *Processes* **8**, 424 (2020).
153. Barrios, J. A., Cano, A., Rivera, F. F., Cisneros, M. E. & Durán, U. Efficiency of integrated electrooxidation and anaerobic digestion of waste activated sludge. *Biotechnol Biofuels* **14**, (2021).
154. De Vrieze, J., Arends, J. B. A., Verbeeck, K., Gildemyn, S. & Rabaey, K. Interfacing anaerobic digestion with (bio)electrochemical systems: Potentials and challenges. *Water Research* vol. 146 244–255 Preprint at https://doi.org/10.1016/j.watres.2018.08.045 (2018).
155. Jorge L. Rico Reyes. Rewiring anaerobic digestion: production of biofuel intermediates and high-value chemicals from cellulosic wastes. *Theses and Dissertations - Department of Civil and Environmental Engineering* (2019).

156. Caporaso, J. G. *et al.* QIIME allows analysis of high-throughput community sequencing data. *Nat Methods* **7**, 335–336 (2010).
157. Mallick, H. *et al.* Multivariable association discovery in population-scale meta-omics studies. *PLoS Comput Biol* **17**, e1009442 (2021).
158. Lozupone, C., Lladser, M. E., Knights, D., Stombaugh, J. & Knight, R. UniFrac: an effective distance metric for microbial community comparison. *ISME J* **5**, 169–172 (2011).
159. Hirano, S., Matsumoto, N., Morita, M., Sasaki, K. & Ohmura, N. Electrochemical control of redox potential affects methanogenesis of the hydrogenotrophic methanogen Methanothermobacter thermautotrophicus. *Lett Appl Microbiol* **56**, 315–321 (2013).
160. Lyu, Z., Shao, N., Akinyemi, T. & Whitman, W. B. Methanogenesis. *Current Biology* **28**, R727–R732 (2018).
161. Li, Y., Li, X., Sun, Y., Zhao, X. & Li, Y. Cathodic microbial community adaptation to the removal of chlorinated herbicide in soil microbial fuel cells. *Environmental Science and Pollution Research* **25**, 16900–16912 (2018).
162. Berg, C., Beckmann, S., Unter Jost, G., Labrenz, M. & Urgens, K. J. Acetate-utilizing bacteria at an oxic-anoxic interface in the Baltic Sea. doi:10.1111/1574-6941.12114.
163. Guarino, F., Motta, O., Turano, M., Proto, A. & Vigliotta, G. Preferential Use of the Perchlorate over the Nitrate in the Respiratory Processes Mediated by the Bacterium Azospira sp. OGA 24. *Water (Basel)* **12**, 2220 (2020).
164. Straub, K. L. & Schink, B. Ferrihydrite-Dependent Growth of *Sulfurospirillum deleyianum* through Electron Transfer via Sulfur Cycling. *Appl Environ Microbiol* **70**, 5744–5749 (2004).
165. Morita, M. *et al.* Potential for Direct Interspecies Electron Transfer in Methanogenic Wastewater Digester Aggregates. *mBio* **2**, (2011).
166. Summers, Z. M., Gralnick, J. A. & Bond, D. R. Cultivation of an Obligate Fe(II)-Oxidizing Lithoautotrophic Bacterium Using Electrodes. *mBio* **4**, (2013).
167. Emerson, D., Fleming, E. J. & Mcbeth, J. M. Iron-Oxidizing Bacteria: An Environmental and Genomic Perspective. (2010) doi:10.1146/annurev.micro.112408.134208.
168. Pisciotta, J. M., Zaybak, Z., Call, D. F., Nam, J.-Y. & Logan, B. E. Enrichment of Microbial Electrolysis Cell Biocathodes from Sediment Microbial Fuel Cell Bioanodes. *Appl Environ Microbiol* **78**, 5212–5219 (2012).

APPENDIX I: CHAPTER 2 SUPPLEMENTARY MATERIALS

Table S1: Comparison of POME structures with the same Alkyl and Oxymethylene Indices. LHV is not included in this comparison since models used for LHV predictions do not account for this structural difference

Species	AI	OI	O/A Ratio	YSI	YSI/LHV (kg/MJ)	T_{boil} (°C)	T_{melt} (°C)	T_{flash} (°C)	DCN	Bio-degradable	Water Solubility (mg/L)
PB-POME$_2$	7	3	0.43	34.9	1.2	208.0	-3.8	70.3	104.7	YES	1127
1P-PM-POME$_2$	7	3	0.43	31.4	1.0	196.0	-14.7	62.1	87.3	NO	1303
PP-POME$_1$	6	2	0.33	27.3	0.9	144.4	-44.7	26.9	87.2	YES	2777
iPiP-POME$_1$	6	2	0.33	18.7	0.6	116.9	-67.7	8.1	74.6	NO	3708
BB-POME$_1$	8	2	0.25	40.2	1.2	187.2	-20.9	56.1	99.0	YES	304
iBiB-POME$_1$	8	2	0.25	51.6	1.5	161.9	-43.3	38.8	79.0	NO	2016

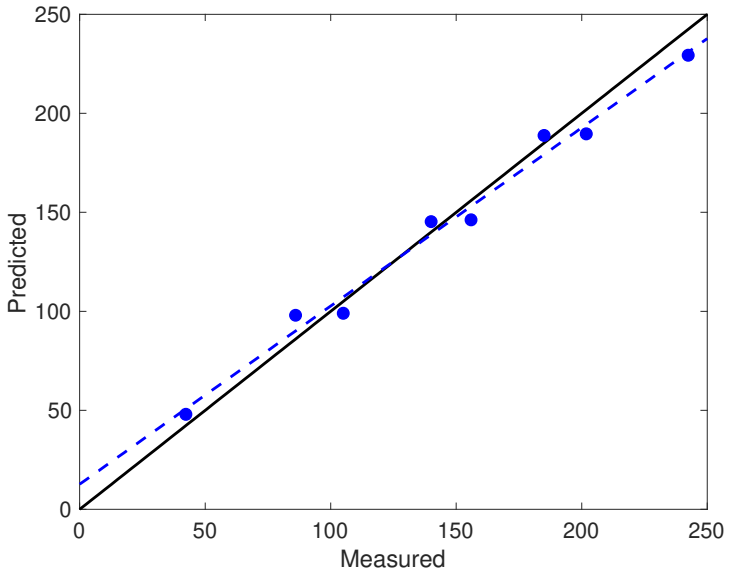

Figure S1: Predicted vs. measured values for T_{boil}. Solid black line: predicted = measured. Blue circles: T_{boil} predictions vs. measured data. Dotted blue line: linear regression of predicted vs. measured values.

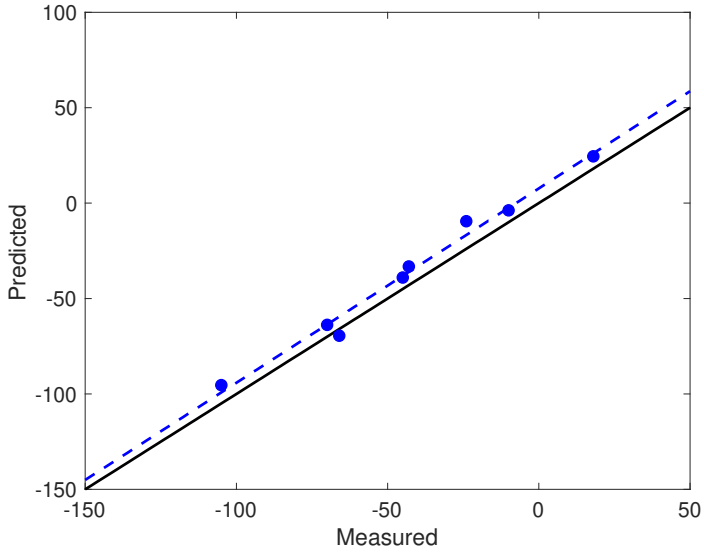

Figure S2: Predicted vs. measured values for T_{melt}. Solid black line: predicted = measured. Blue circles: T_{melt} predictions vs. measured data. Dotted blue line: linear regression of predicted vs. measured values.

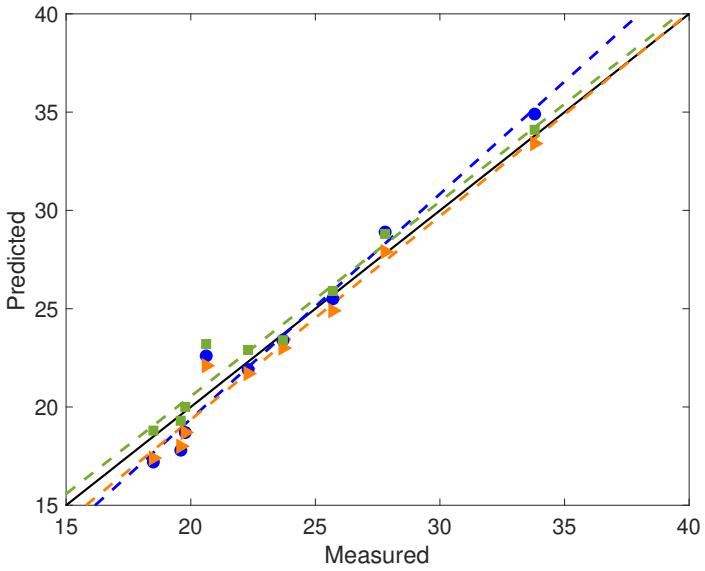

Figure S3: Predicted vs. measured values for LHV. Solid black line: predicted = measured. Blue circles: Dulong mode (Eq. 4) predictions vs. measured data. Orange triangles: Boie model (Eq. 5) predictions vs. measured data. Green squares: Lloyd and Davenport model (Eq. 6) vs. measured data. Dotted blue line: linear regression of predicted vs. measured values for the Dulong model. Dotted orange line: linear regression of predicted vs. measured values for the Boie model. Dotted green line: linear regression of predicted vs. measured values for the Lloyd and Davenport model.

151

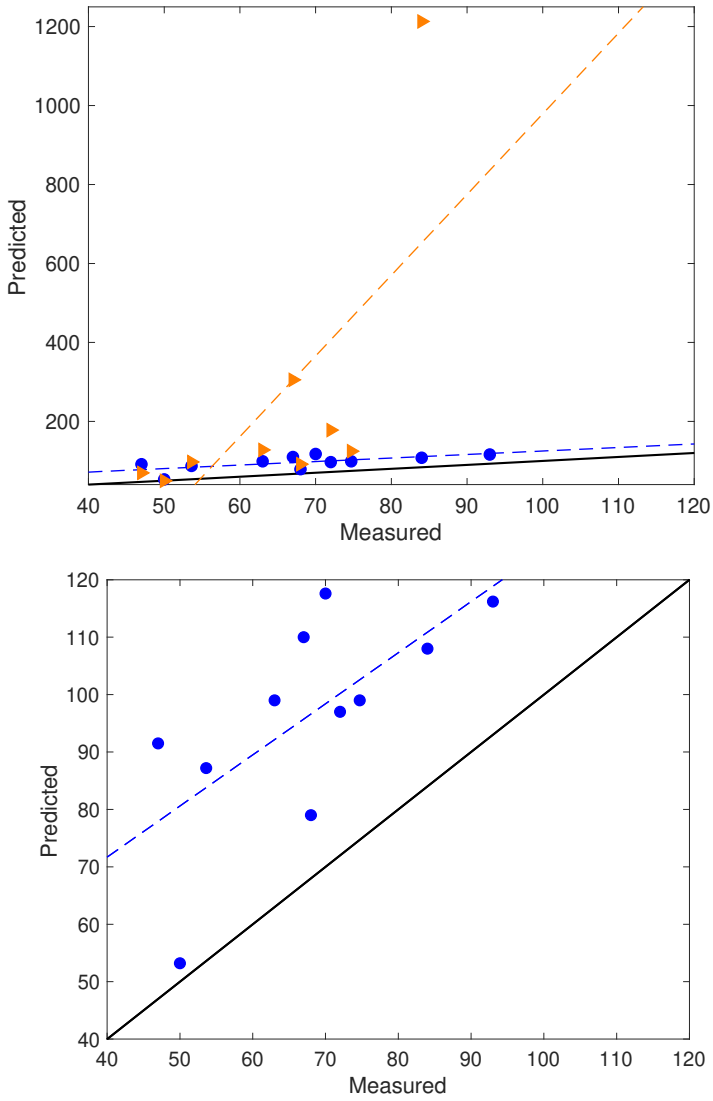

Figure S4: Predicted vs. measured values for DCN. A) Solid black line: predicted = measured. Blue circles: Machine learning model predictions vs. measured data. Orange triangles: Group contribution model predictions vs. measured data. Dotted blue line: linear regression of predicted vs. measured values for the machine learning model. B) Machine learning model only.

152

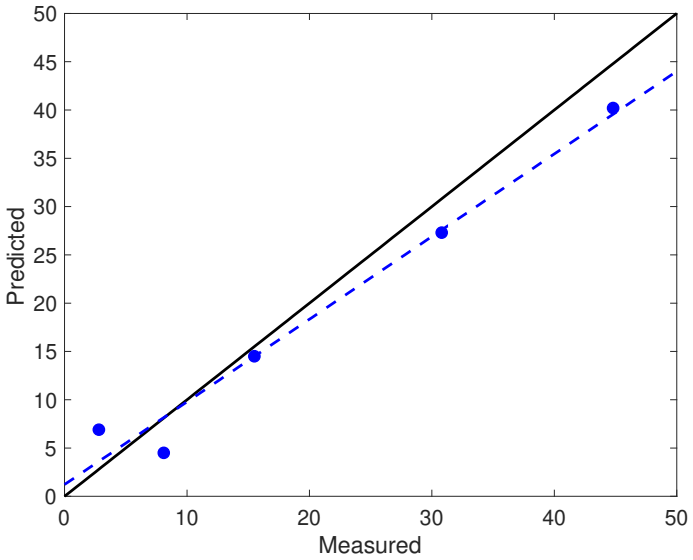

Figure S5: Predicted vs. measured values for YSI. Solid black line: predicted = measured. Blue circles: YSI predictions vs. measured data. Dotted blue line: linear regression of predicted vs. measured values.

153

Table S2: Significant associations identified by MaAsLin analysis for -300 mV vs. Ag/AgCl relative to respective controls

feature	metadata	value	coef	stderr	N	N.not.0	pval	qval
d__Bacteria..p__Firmicutes..c__Clostridia..o__Peptostreptococcales.Tissierellales..f__Peptostreptococcaceae..g__Terrisporobacter..s__uncultured_bacterium	Trt	Control	-2.034205533	0.236808981	19	9	1.37E-07	4.25E-05
d__Bacteria..p__Firmicutes..c__Clostridia..o__Peptostreptococcales.Tissierellales..f__Anaerovoracaceae..g__.Eubacterium._nodatum_group	Trt	Control	-2.372705363	0.426784171	19	12	3.46E-05	0.005379368
d__Bacteria..p__Campilobacterota..c__Campylobacteria..o__Campylobacterales..f__Arcobacteraceae	Trt	Control	-3.695806668	0.726290764	19	14	9.11E-05	0.009441305
d__Bacteria..p__Proteobacteria..c__Gammaproteobacteria..o__Burkholderiales..f__Rhodocyclaceae..g__Azospira	Trt	Control	-2.284889274	0.544276736	19	17	0.000604188	0.042901982
d__Bacteria..p__Firmicutes..c__Clostridia..o__Oscillospirales..f__Ruminococcaceae..g__uncultured..s__uncultured_compost	Trt	Control	-1.593790387	0.385279675	19	13	0.000689742	0.042901982
d__Bacteria..p__Bacteroidota..c__Bacteroidia..o__Bacteroidales..f__Bacteroidaceae..g__Bacteroides..s__iron.reducing_bacterium	Trt	Control	-1.505660646	0.39166838	19	18	0.001299876	0.067376892
d__Bacteria..p__Bacteroidota..c__Bacteroidia..o__Sphingobacteriales..f__ST.12K33..g__ST.12K33..s__uncultured_bacterium	Trt	Control	2.732826996	0.77392691	19	17	0.002564988	0.099713906
d__Bacteria..p__Campilobacterota..c__Campylobacteria..o__Campylobacterales..f__Sulfurospirillaceae..g__Sulfurospirillum..s__Sulfurospirillum_deleyianum	Trt	Control	-2.158284265	0.604030768	19	6	0.00234151	0.099713906
d__Bacteria..p__Firmicutes..c__Syntrophomonadia..o__Syntrophomonadales..f__Syntrophomonadaceae	Trt	Control	1.780351419	0.517011672	19	7	0.003101185	0.107163182
d__Bacteria..p__Bacteroidota..c__Bacteroidia..o__Bacteroidales..f__Rikenellaceae..g__Alistipes..s__uncultured_bacterium	Trt	Control	2.614880402	0.81262299	19	16	0.005050017	0.157055534
d__Bacteria..p__Firmicutes..c__Clostridia..o__Clostridiales..f__Clostridiaceae..g__Clostridium_sensu_stricto_7..s__Clostridium_sp.	Trt	Control	-1.38401718	0.445075694	19	15	0.006371774	0.18014743
d__Bacteria..p__Firmicutes..c__Clostridia..o__Clostridiales..f__Clostridiaceae..g__Clostridium_sensu_stricto_1	Trt	Control	1.245910381	0.447529383	19	19	0.012727211	0.182390009
d__Bacteria..p__Bacteroidota..c__Bacteroidia..o__Bacteroidales..f__Rikenellaceae..g__dgA.11_gut_group..s__uncultured_bacterium	Trt	Control	1.478729802	0.496819539	19	19	0.0084702	0.182390009
d__Bacteria..p__Firmicutes..c__Clostridia..o__Peptostreptococcales.Tissierellales..f__Peptostreptococcaceae..g__Terrisporobacter..s__Terrisporobacter_glycolicus	Trt	Control	1.312829945	0.441564372	19	17	0.008529163	0.182390009
d__Bacteria..p__Bacteroidota..c__Bacteroidia..o__Bacteroidales..f__Dysgonomonadaceae..g__Dysgonomonas	Trt	Control	-1.938579585	0.678260357	19	15	0.01088486	0.182390009
d__Bacteria..p__Bacteroidota..c__Bacteroidia..o__Bacteroidales..f__Bacteroidaceae..g__Bacteroides	Trt	Control	-1.722697342	0.636798664	19	17	0.015009716	0.182390009
d__Bacteria..p__Bacteroidota..c__Bacteroidia..o__Bacteroidales..f__Bacteroidaceae..g__Bacteroides..s__Bacteroides_paurosaccharolyticus	Trt	Control	-1.745346353	0.65298034	19	12	0.016057412	0.182390009
d__Bacteria..p__Proteobacteria..c__Gammaproteobacteria..o__Aeromonadales..f__Aeromonadaceae	Trt	Control	-1.560442977	0.567202351	19	13	0.013635882	0.182390009
d__Bacteria..p__Proteobacteria..c__Gammaproteobacteria..o__Burkholderiales..f__Comamonadaceae	Trt	Control	-1.433443495	0.536745139	19	9	0.016133506	0.182390009
d__Bacteria..p__Firmicutes..c__Clostridia..o__Peptostreptococcales.Tissierellales..f__Peptostreptococcaceae..g__Acetoanaerobium..s__uncultured_bacterium	Trt	Control	1.68857154	0.642305345	19	12	0.017593892	0.182390009

d__Bacteria..p__Bacteroidota..c__Bacteroidia..o__Bacteroidales..f__Williamwhitmaniaceae..g__Acetobacteroides..s__uncultured_bacterium	Trt	Control	-1.854215136	0.698655413	19	10	0.016702011	0.182390009
d__Bacteria..p__Firmicutes..c__Clostridia..o__Lachnospirales..f__Lachnospiraceae..g__XBB1006..s__uncultured_bacterium	Trt	Control	-2.14449374	0.799595481	19	16	0.015756494	0.182390009
d__Bacteria..p__Firmicutes..c__Clostridia..o__Oscillospirales..f__Ruminococcaceae	Trt	Control	-2.186865887	0.814144554	19	10	0.015621845	0.182390009
d__Bacteria..p__Firmicutes..c__Clostridia..o__Oscillospirales..f__Oscillospirales..g__Hydrogenoanaerobacterium..s__uncultured_bacterium	Trt	Control	-1.12875984	0.419890556	19	6	0.015552503	0.182390009
d__Bacteria..p__Firmicutes..c__Clostridia..o__Oscillospirales..f__Butyricicoccaceae..g__UCG.009..s__uncultured_bacterium	Trt	Control	-1.880195234	0.713080788	19	11	0.017311531	0.182390009
d__Bacteria..p__Firmicutes..c__Clostridia..o__Clostridiales..f__Clostridiaceae..g__Clostridium_sensu_stricto_12..s__Clostridium_magnum	Trt	Control	-1.35576489	0.492720167	19	11	0.013622457	0.182390009
d__Bacteria..p__Synergistota..c__Synergistia..o__Synergistales..f__Synergistaceae	Trt	Control	-1.312059899	0.462869771	19	15	0.011439686	0.182390009
d__Bacteria..p__Desulfobacterota..c__Desulfuromonadia..o__Geobacterales..f__Geobacteraceae..g__Geobacter	Trt	Control	-2.462296001	0.924196978	19	6	0.016348763	0.182390009
d__Bacteria..p__Firmicutes..c__Clostridia..o__Oscillospirales..f__Ruminococcaceae..g__uncultured..s__uncultured_Clostridium	Trt	Control	-1.395001882	0.463767518	19	5	0.007918845	0.182390009
d__Bacteria..p__Bacteroidota..c__Bacteroidia..o__Bacteroidales..f__Rikenellaceae..g__Rikenellaceae..s__uncultured_bacterium	Trt	Control	-1.772304362	0.616744138	19	6	0.010534312	0.182390009
d__Bacteria..p__Bacteroidota..c__Bacteroidia..o__Bacteroidales..f__Tannerellaceae..g__Macellibacteroides	Trt	Control	-0.792024468	0.307100338	19	19	0.01950672	0.188629328
d__Bacteria..p__Proteobacteria..c__Gammaproteobacteria..o__Burkholderiales..f__Rhodocyclaceae..g__uncultured..s__uncultured_Azospira	Trt	Control	-2.167233372	0.849206486	19	8	0.020621856	0.188629328
d__Bacteria..p__Bacteroidota..c__Bacteroidia..o__Bacteroidales..f__p.251.o5..g__p.251.o5..s__metagenome	Trt	Control	1.611915403	0.62434254	19	6	0.019396737	0.188629328
d__Bacteria..p__Firmicutes..c__Clostridia..o__Oscillospirales..f__Oscillospiraceae	Trt	Control	-1.258207618	0.490296851	19	11	0.020029622	0.188629328
d__Bacteria..p__Firmicutes..c__Clostridia..o__Peptostreptococcales.Tissierellales..f__Anaerovoracaceae..g__uncultured	Trt	Control	1.019135825	0.419859605	19	6	0.026611612	0.236463177

155

Table S3: Significant associations identified by MaAsLin analysis for -600 mV vs. Ag/AgCl relative to respective controls

feature	metadata	value	coef	stderr	N	N.not.0	pval	qval
d__Bacteria..p__Desulfobacterota..c__Desulfovibrionia..o__Desulfovibrionales..f__Desulfovibrionaceae..g__Desulfovibrio	Trt	Control	1.555259186	0.193582646	12	6	1.13E-05	0.002744952
d__Bacteria..p__Firmicutes..c__Clostridia..o__Lachnospirales..f__Lachnospiraceae..g__Lachnospiraceae_NK4A136_group..s__uncultured_bacterium	Trt	Control	-2.372792734	0.317089539	12	7	2.10E-05	0.002744952
d__Bacteria..p__Firmicutes..c__Clostridia..o__Peptostreptococcales.Tissierellales..f__Peptostreptococcaceae..g__Acetoanaerobium..s__uncultured_bacterium	Trt	Control	2.211635301	0.33629743	12	6	6.26E-05	0.005447021
d__Bacteria..p__Bacteroidota..c__Bacteroidia..o__Bacteroidales..f__Rikenellaceae..g__Anaerocella..s__uncultured_Bacteroidales	Trt	Control	-5.042299129	0.848357033	12	9	0.000142458	0.008801726
d__Bacteria..p__Firmicutes..c__Clostridia..o__Oscillospirales..f__Oscillospiraceae..g__Colidextribacter	Trt	Control	-1.48727853	0.255603037	12	12	0.000168615	0.008801726
d__Bacteria..p__Firmicutes..c__Clostridia..o__Clostridiales..f__Clostridiaceae..g__Clostridium_sensu_stricto_1..s__Clostridium_butyricum	Trt	Control	-1.899399724	0.386494792	12	9	0.00060989	0.026530204
d__Bacteria..p__Campilobacterota..c__Campylobacteria..o__Campylobacterales..f__Arcobacteraceae	Trt	Control	-3.633209877	0.813831013	12	6	0.001207993	0.035437606
d__Archaea..p__Euryarchaeota..c__Methanobacteria..o__Methanobacteriales..f__Methanobacteriaceae..g__Methanosphaera	Trt	Control	-2.202441502	0.494164063	12	8	0.001221986	0.035437606
d__Bacteria..p__Firmicutes..c__Clostridia..o__Eubacteriales..f__Eubacteriaceae	Trt	Control	-2.256290105	0.503045043	12	12	0.001169452	0.035437606
d__Bacteria..p__Proteobacteria..c__Gammaproteobacteria..o__Enterobacterales..f__Enterobacteriaceae	Trt	Control	-2.633088016	0.740752181	12	12	0.005227919	0.069297918
d__Bacteria..p__Firmicutes..c__Clostridia..o__Peptostreptococcales.Tissierellales..f__Peptostreptococcaceae..g__Terrisporobacter..s__uncultured_bacterium	Trt	Control	-2.411738261	0.618409009	12	11	0.002961451	0.069297918
d__Bacteria..p__Proteobacteria..c__Gammaproteobacteria..o__Burkholderiales..f__Rhodocyclaceae..g__uncultured..s__uncultured_Azospira	Trt	Control	-1.954480074	0.518417685	12	8	0.003661016	0.069297918
d__Bacteria..p__Firmicutes..c__Clostridia..o__Lachnospirales..f__Lachnospiraceae..g__Butyrivibrio..s__uncultured_bacterium	Trt	Control	-2.322683274	0.640043512	12	10	0.004620633	0.069297918
d__Bacteria..p__Proteobacteria..c__Gammaproteobacteria..o__Pseudomonadales..f__Moraxellaceae..g__Acinetobacter	Trt	Control	-2.095776769	0.594910625	12	11	0.005512223	0.069297918
d__Bacteria..p__Firmicutes..c__Clostridia..o__Clostridiales..f__Clostridiaceae..g__Clostridium_sensu_stricto_7..s__Clostridium_sp.	Trt	Control	-1.978948985	0.539548077	12	10	0.004332917	0.069297918
d__Bacteria..p__Desulfobacterota..c__Syntrophorhabdia..o__Syntrophorhabdales..f__Syntrophorhabdaceae..g__Syntrophorhabdus..s__uncultured_bacterium	Trt	Control	1.598219929	0.422243491	12	5	0.003572154	0.069297918
d__Bacteria..p__Chloroflexi..c__Anaerolineae..o__Anaerolineales..f__Anaerolineaceae..g__Anaerolinea..s__uncultured_bacterium	Trt	Control	1.21342465	0.344229783	12	11	0.005492033	0.069297918
d__Bacteria..p__Synergistota..c__Synergistia..o__Synergistales..f__Synergistaceae..g__Lactivibrio..s__uncultured_bacterium	Trt	Control	1.882712639	0.531592669	12	6	0.005342088	0.069297918
d__Bacteria..p__Firmicutes..c__Clostridia..o__Lachnospirales..f__Lachnospiraceae	Trt	Control	-1.66557485	0.473715376	12	5	0.005575695	0.069297918
d__Bacteria..p__Firmicutes..c__Clostridia..o__Clostridiales..f__Clostridiaceae..g__Clostridium_sensu_stricto_16..s__uncultured_bacterium	Trt	Control	-1.773168413	0.48051897	12	9	0.004176079	0.069297918

156

d__Bacteria..p__Actinobacteriota..c__Acidimicrobiia..o__Microtrichales..f__Microtrichaceae..g__IMCC26207	Trt	Control	1.533623569	0.410347272	12	5	0.003863158	0.069297918
d__Bacteria..p__Cloacimonadota..c__Cloacimonadia..o__Cloacimonadales..f__W27..g__W27..s__uncultured_bacterium	Trt	Control	1.960620666	0.575593994	12	6	0.006700279	0.079489669
d__Bacteria..p__Firmicutes..c__Clostridia..o__Peptostreptococcales.Tissierellales..f__Peptostreptococcaceae..g__Terrisporobacter..s__Terrisporobacter_glycolicus	Trt	Control	1.463656903	0.445215251	12	9	0.008184164	0.082453985
d__Bacteria..p__Firmicutes..c__Bacilli..o__Bacillales..f__Bacillaceae..g__Bacillus	Trt	Control	-4.584279047	1.39535429	12	5	0.008213807	0.082453985
d__Bacteria..p__Actinobacteriota..c__Actinobacteria..o__Corynebacteriales..f__Corynebacteriaceae..g__Corynebacterium	Trt	Control	-1.625078485	0.486690444	12	5	0.007502646	0.082453985
d__Bacteria..p__Caldatribacteriota..c__Caldatribacteriia..o__Caldatribacteriales..f__Caldatribacteriaceae..g__Candidatus_Caldatribacterium	Trt	Control	1.20937443	0.366871717	12	11	0.008061688	0.082453985
d__Bacteria..p__Patescibacteria..c__ABY1..o__Candidatus_Falkowbacteria..f__Candidatus_Falkowbacteria..g__Candidatus_Falkowbacteria..s__metagenome	Trt	Control	1.655245723	0.513743558	12	7	0.009145179	0.0884034
d__Bacteria..p__Actinobacteriota..c__Thermoleophilia..o__Gaiellales..f__uncultured..g__uncultured..s__uncultured_prokaryote	Trt	Control	0.907058168	0.310972463	12	4	0.015383377	0.14339505
d__Bacteria..p__Firmicutes..c__Clostridia..o__Oscillospirales..f__Ruminococcaceae	Trt	Control	-2.51548909	0.882621634	12	8	0.017249506	0.155245551
d__Bacteria..p__Cloacimonadota..c__Cloacimonadia..o__Cloacimonadales	Trt	Control	1.385162934	0.501548188	12	12	0.020068593	0.174596758
d__Bacteria..p__Proteobacteria..c__Gammaproteobacteria..o__Xanthomonadales..f__Xanthomonadaceae..g__Stenotrophomonas	Trt	Control	-1.153283704	0.422857382	12	6	0.021289716	0.17924567
d__Bacteria..p__Firmicutes..c__Clostridia..o__Clostridiales..f__Clostridiaceae..g__Clostridium_sensu_stricto_13	Trt	Control	0.842072388	0.319947072	12	12	0.025079737	0.203583423
d__Bacteria..p__Firmicutes..c__Clostridia..o__Oscillospirales..f__Oscillospiraceae..g__Oscillibacter..s__uncultured_Oscillibacter	Trt	Control	-1.270018137	0.48533988	12	7	0.025740433	0.203583423
d__Archaea..p__Halobacterota..c__Methanosarcinia..o__Methanosarciniales..f__Methanosaetaceae..g__Methanosaeta	Trt	Control	1.750614057	0.68977936	12	11	0.02946738	0.226205477
d__Bacteria..p__Campilobacterota..c__Campylobacteria..o__Campylobacterales..f__Arcobacteraceae..g__Arcobacter	Trt	Control	1.343652641	0.541847633	12	6	0.032556146	0.242775829

157

1. *Terrisporobacter* uncultured bacterium

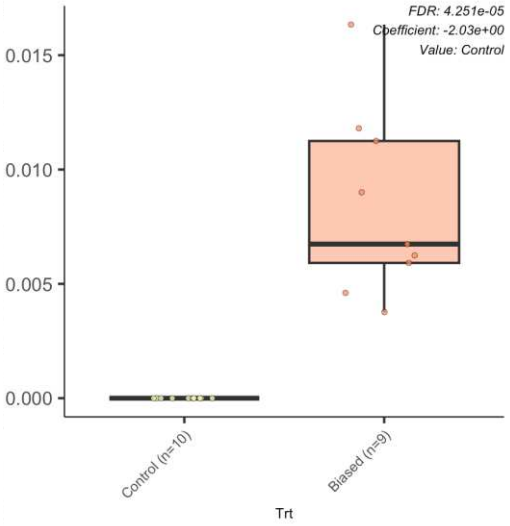

2. *Eubacterium nodatum*

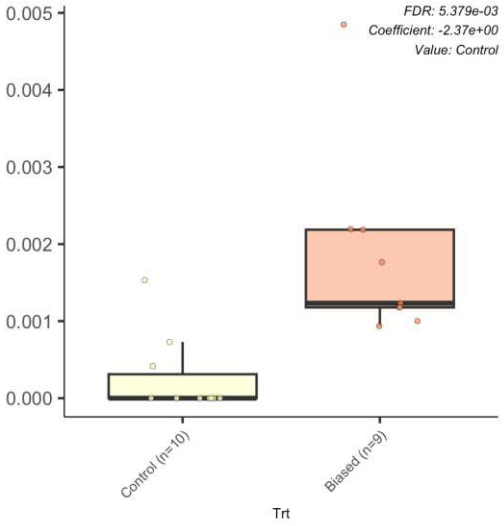

3. *Arcobacteraceae*

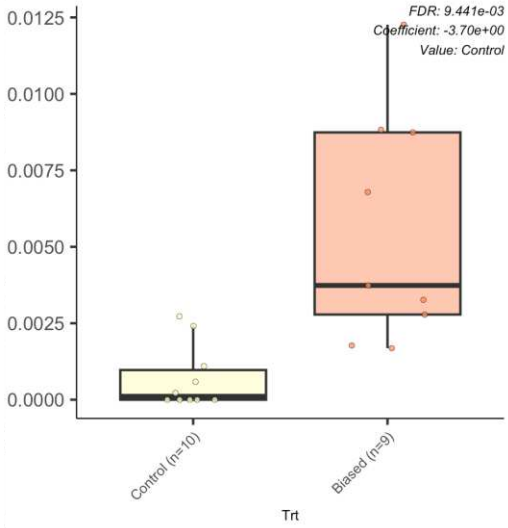

4. *Azospira*

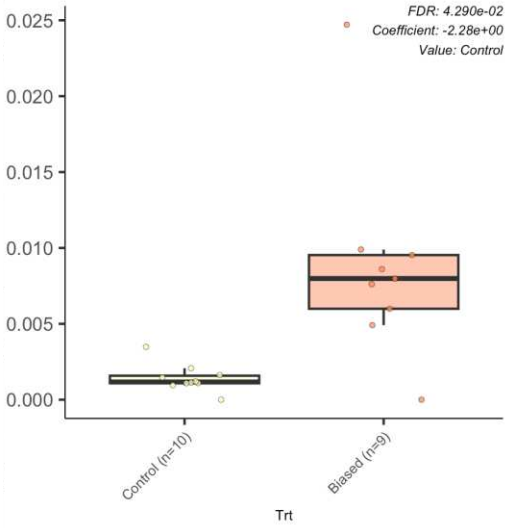

5. *Ruminococcaceae*

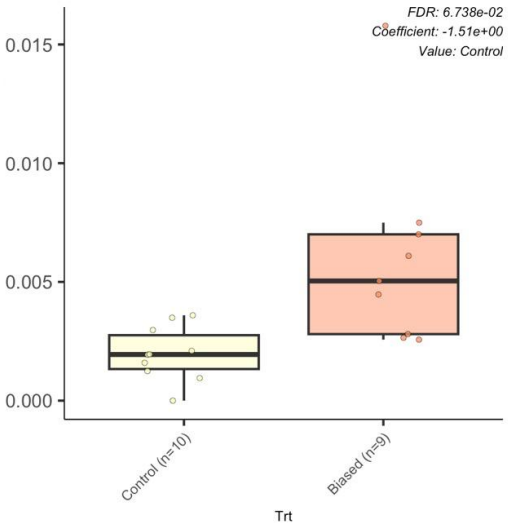

6. *Bacteroides iron reducing bacterium*

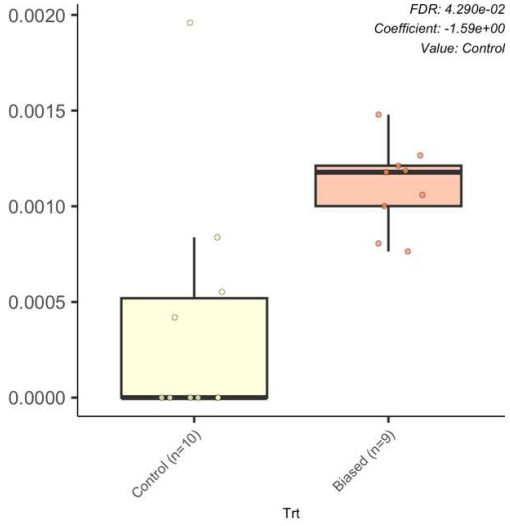

7. *ST.12K33*

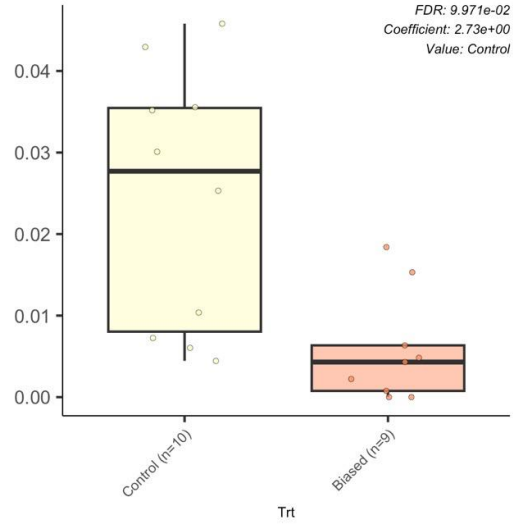

8. *Sulfurospirillum deleyianum*

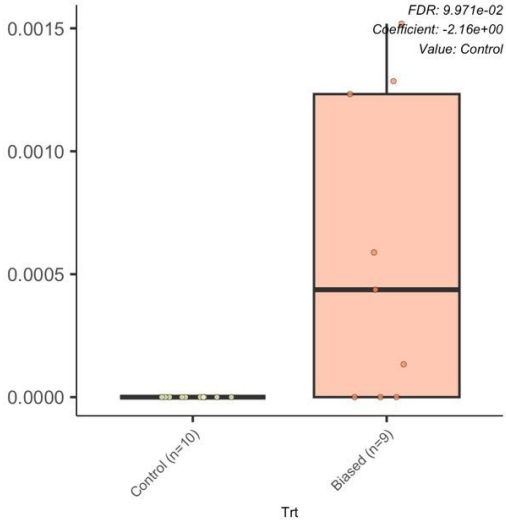

159

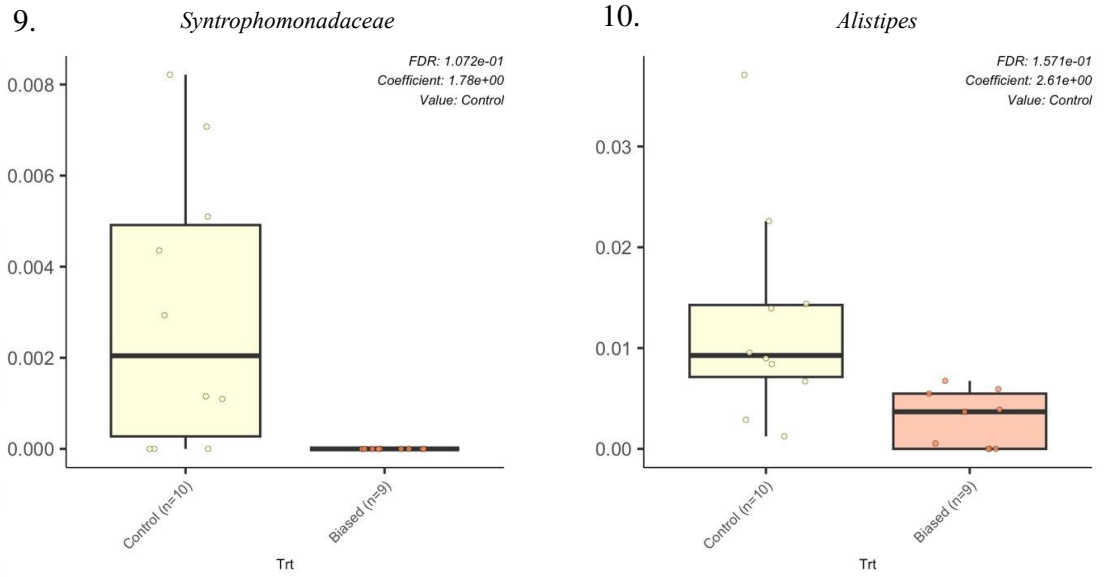

Figure S6.1-10: Differential abundances of top ten most significant associations for -300 mV vs. Ag/AgCl vs. respective controls

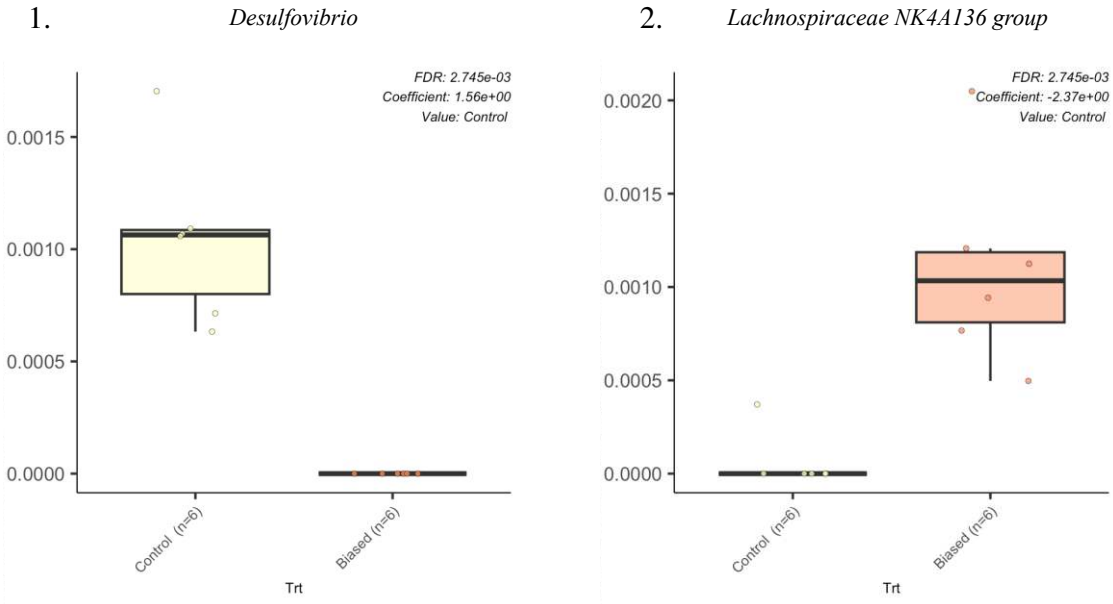

160

3. *Acetoanaerobium*

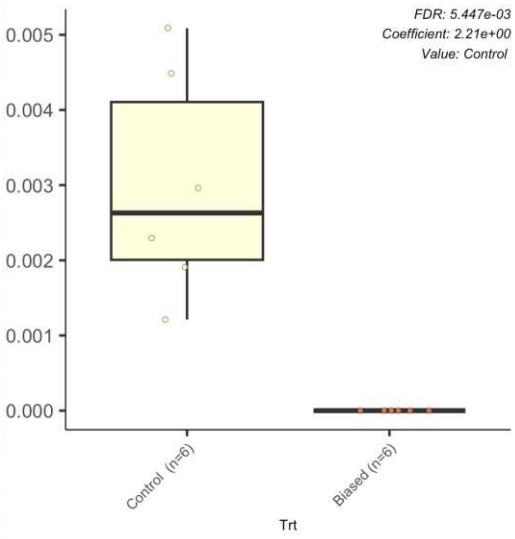

4. *Anaerocella*

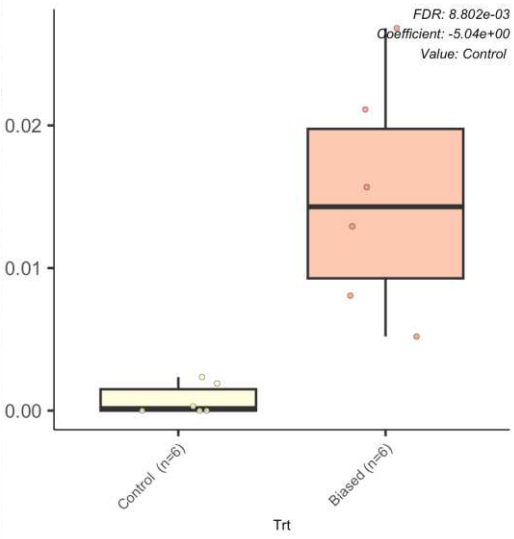

5. *Colidextribacter*

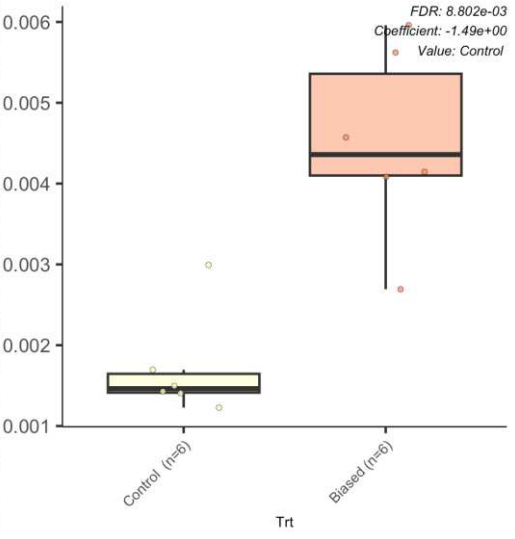

6. *Clostridium butyricum*

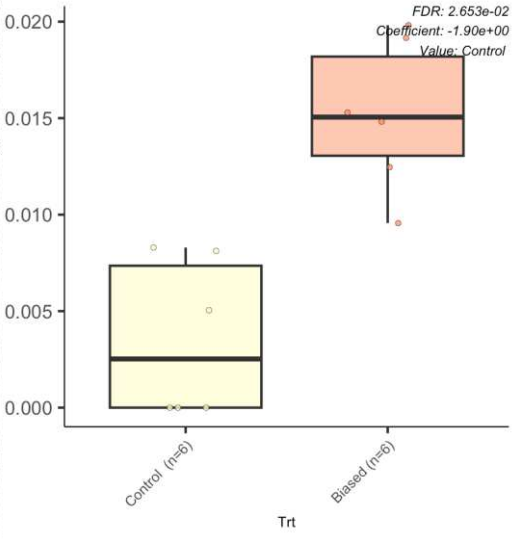

161

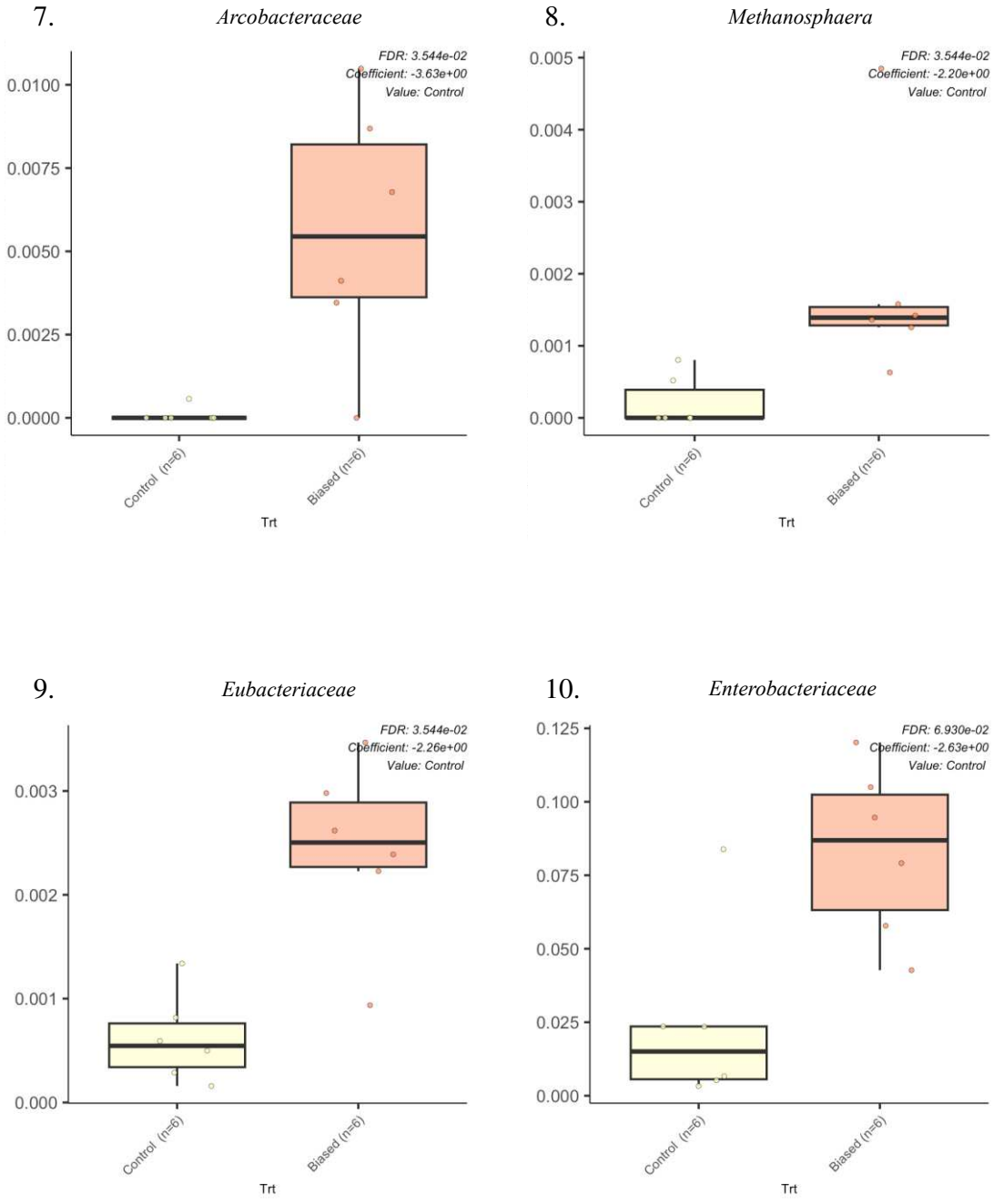

Figure S7.1-10: Differential abundances of top ten most significant associations for -600 mV vs. Ag/AgCl vs. respective controls

162